THE ATOMIC STRUCTURE OF SOME METALLIC GLASSES

AND

THE INFLUENCE OF THE PREPARATION TECHNIQUE ON THE AMORPHOUS STATE

Thesis by

Madhav Mehra

In Partial Fulfillment of the Requirements

for the Degree of

Doctor of Philosophy

California Institute of Technology

Pasadena, California

1985

(Submitted August 2, 1984)

for

Boshida and Boudi

Ah, but a man's reach
Should exceed his grasp,
Or what's heaven for.

- Robert Browning

ACKNOWLEDGEMENTS

It would be futile to try to record the help given at every stage of this work by Dr. William L. Johnson. His advice was always coherent and his guidance keen. I was often amazed at his trenchant approach to research problems and have sometimes suspected his scientific foresight to be laced with a hint of clairvoyance ! Working with Dr. Johnson has been very rewarding, and I have learnt a lot. I thank him for that.

My experiences at Caltech would not be as memorable were it not for the opportunity to get to know Professor Pol Duwez. A man who deserves the highest accolade for his scientific achievements, Professor Duwez has the graciousness to treat young and aspiring students as friends. In my opinion, that is indeed the greatest gift a student can receive. I found him to be an extremely perceptive and kind person. His inimitable sense of humour and good-natured encouragement was a constant source of inspiration.

Dr. Art Williams was the first to befriend me when I joined Caltech. He not only helped me get started on my research, but equally important, he filled me in on all the stories around the lab and introduced me to all the "cheap" restaurants in town ! Thank you, Art.

The studies on the thin films were done in collaboration with Anil Thakoor and Bruce Clemens. I am grateful for their help.

Dave Baxter, Bob Schulz, Michael Atzmon, Vladimir Matijasevic and Karl Unruh were more than colleagues. They were friends. I must especially thank Dave for his patience in answering the barrage of questions that I hurled at him over these past four years. Karl's intimate knowledge of Webster's Dictionary was a great help. I would like to thank him for critically proof-reading this manuscript.

Angela Bressan and Concetto Geremia were invaluable for their technical support. Both perfectionists, it was a pleasure to work with them. It would be remiss of me to not thank Concetto for the things he did aside from his work in the lab. Of special mention are his attributes as a "hair-stylist" and a chef. Angela, a true mother at heart, "adopted" me into her favourite coterie. For that I am especially grateful.

It is difficult to thank one's parents for anything specific, for it seems so minute in the realm of all that they have done. Nonetheless I must, for I have been singularly fortunate to enjoy their love and support.

I thank my wife Deepa for being there. Her friendship was my greatest asset and her vivacity brought cheer on many a rainy day.

Finally, I would like to thank two special people. Emotions surge, but words fail me. I cannot eulogize them enough for what they were and all they have done. In practically every facet of life they have been my inspiration. To them I dedicate this thesis.

ABSTRACT

In this work the structure of some new transition metal-metalloid glasses is discussed. Based on the Ru-Zr-B and the Rh-Si-B alloy series, these glasses are unique in that they contain up to 52 atomic percent metalloids. Available dense random packing models are not successful in explaining the structure of these glasses. The presence of a peak in the reduced radial distribution functions, G(r), at a distance of $\sqrt{2}$ times the nearest-neighbour distance suggests the presence of octahedral coordination. This coordination, absent in the dense random packed models is explained by invoking a packing of trigonal prisms. With this proposed short range order the main features in the experimentally obtained G(r) have been reproduced.

Also presented is a study that compares the amorphous state obtained in the same alloy by two different techniques. Films of $(Mo_{0.6}Ru_{0.4})_{82}B_{18}$ obtained by sputtering are found to be more disordered than their liquid quenched counterparts. This increased disorder is evidenced through measurements of the G(r) and superconducting properties. The films have a lower atomic density than liquid quenched films of the same composition. This lower density reflects the presence of more entrapped free volume.

Finally, the results of a study on wear resistant amorphous coatings is reported. It is found that, by coating a surface of 52100 bearing steel with a thin film of $(W_{0.6}Re_{0.4})_{76}B_{24}$, the wear resistance of the steel is increased by three orders of magnitude. This encouraging result suggests that the technological hopes for amorphous materials may indeed be realised.

TABLE OF CONTENTS

TABLE OF CONTENTS (cont.)

LIST OF ILLUSTRATIONS

LIST OF ILLUSTRATIONS (cont.)

LIST OF ILLUSTRATIONS (cont.)

LIST OF ILLUSTRATIONS (cont.)

LIST OF ILLUSTRATIONS (cont.)

LIST OF ILLUSTRATIONS (cont.)

LIST OF ILLUSTRATIONS (cont.)

LIST OF ILLUSTRATIONS (cont.)

LIST OF TABLES

LIST OF TABLES (cont.)

CHAPTER 1

INTRODUCTION

§ 1.1 HISTORICAL OVERVIEW

The first report in the modern scientific literature on the production of amorphous metallic alloys was published in 1934 by Kramer[1,2]. The technique used was vapour-deposition. In 1950, Brenner et al.[3] reported electro-depositing amorphous Ni-P alloys. A few years later, Buckel and Hilsch vapour deposited tin, gallium and bismuth in the amorphous form[4,5]. Even though the amorphous structure in many of these cases could be retained only at low (below 100 K) temperatures, the scientific community was beginning to raise an eyebrow. It was not, however, until September 1959, when Duwez and his co-workers[6] cooled a molten alloy of Au-Si rapidly enough to obtain an amorphous phase, that interest was really stirred.

Soon afterwords, Cohen and Turnbull[7] pointed out that the composition of the Au-Si alloy was very close to a deep eutectic in the corresponding equilibrium phase diagram. This condition was known to be favourable for glass formation in covalent as well as ionic systems. This empirical observation proved to be a powerful guide in the search for other systems that might form glasses when cooled rapidly from the melt. In the next couple of years Duwez and his co-workers published work on the Ag-Ge and Pd-Si alloys[8]. The reaction was mixed. While the group at Harvard proceeded to measure the glass transition temperature in these alloys[9,10], an important piece of work, some scientists elsewhere dismissed them as "Duwez's stupid alloys"!

Empirically, researchers have found that metallic glasses can be divided into categories based on the elements in the alloys. Two of the most studied categories are the Transition Metal-Metalloid (TM-M) alloys and the Early Transition Metal-Late Transition Metal (ETM-LTM) alloys. Examples of the former are Fe-B, Pd-Si and (Mo,Ru)-B while in the ETM-LTM class belong alloys such as Zr-Cu and Zr-Ni. In all these alloys the presence of a deep eutectic near the glass forming region has been noted. These eutectics are often 200 to 300 C lower than those predicted by regular solution theory. This is indicative of a large negative heat of mixing between the two elements, over and above the entropic effects. Gilman[11] has studied the structure of TM-M eutectic liquids and found that they possess strong short range order. He also noted that of all the eutectics formed by transition metals with boron, carbon and phosphorous, a large percentage have between 13 and 18 atomic percent metalloids. Gilman proposed that it is the presence of this short range order in the eutectic liquid that permits glass formation at rates considerably slower than those expected for pure metals.

Thermodynamic arguments have also been presented[12] to explain why it is easier to quench alloys rather than pure metals. From a very simplistic point of view, the bottom line in terms of glass formation is a sufficiently rapid cooling rate. This effect is illustrated in figure 1.1, which shows a schematic time-temperature-transformation (t-t-t) curve. AB denotes the contour of the smallest detectable transformed fraction in the time-temperature space of a given material. XY denotes the slowest cooling rate necessary to avoid this detectable transformation. The form of the t-t-t curve and the magnitude of the

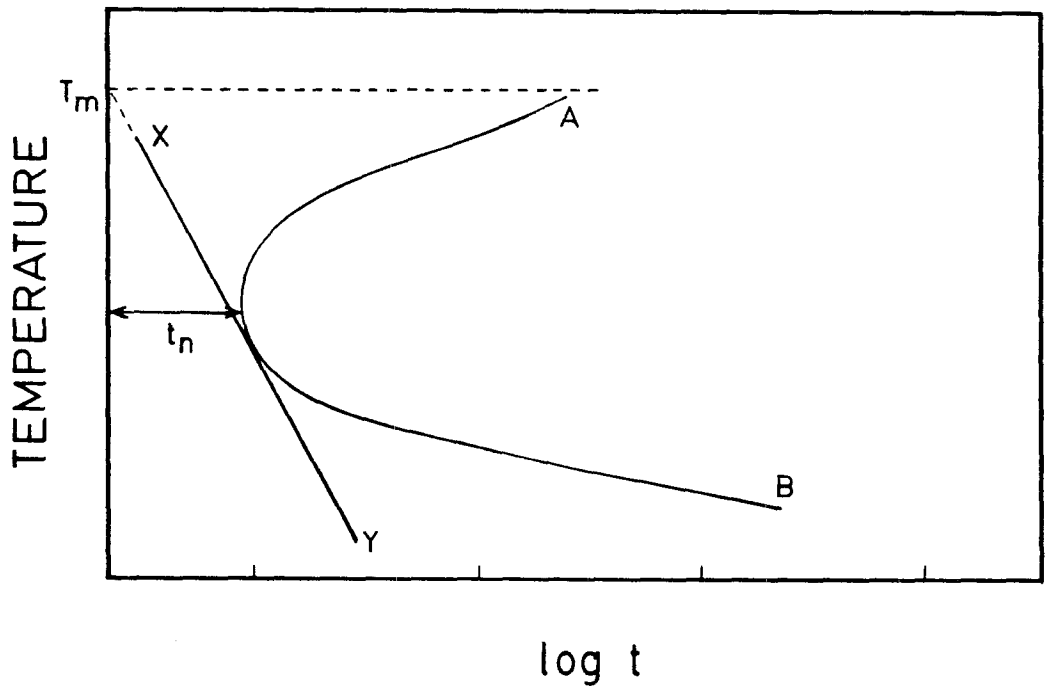

Figure 1.1 A schematic "time-temperature-transformation" diagram. AB represents the time required for the onset of a minimum detectable transformation at a given temperature. XY represents the slowest cooling rate that will suppress the transformation on quenching from the melting temperature, T_m.

time at the nose, t_n, under ideal conditions is largely a reflection of the competition between the increasing driving force for nucleation and the decreasing atomic mobility with decreasing temperature.

The glass forming ability (GFA) of a metallic system is often correlated to its reduced glass transition temperature, $T_{rg} = T_g/T_l$, where T_g is the glass transition temperature and T_l the liquidus temperature for the system. It is at once evident that alloying a pure element would, at least initially, increase the T_{rg} for the system, and hence assist glass formation. A larger t_n would also be favourable towards this same end.

In the twenty five years that have passed since their discovery, metallic glasses have enjoyed centre stage attention in the field of new materials. Physicists, chemists and material scientists have collaborated fruitfully in order to learn about and understand these materials. In the process a plethora of interesting information and data has been accumulated.

Since the very start, the technological possibilities of amorphous metallic alloys have been inspiring, and while they have taken over two decades to come to fruition, metallic glasses are finally finding increasing use in industrial applications. From materials for sophisticated electronic and low frequency magnetic devices[13] to uses such as corrosion and wear resistant coatings[14], these materials have a wide gamut of possible applications.

§ 1.2 THIS WORK

The work presented in this thesis deals primarily with the study of the atomic structure of metallic glasses. Two aspects are considered. First, an attempt is made to analyse the structural

information obtained on some new metallic glasses. While these glasses belong to the TM-M category, they are unique in that they contain as much as 52 atomic percent metalloids. This is an extremely high proportion of metalloids, considerably higher than the 15 to 25 atomic percent found in "traditional" TM-M glasses. The presence of such a large number of metalloid atoms necessitates the invocation of some new ideas on the packing of atoms in these glasses.

Second, in view of the increasingly important applications of these materials, an attempt is made to correlate the structure of a given TM-M glass to the technique of preparation. The techniques compared are splat quenching and sputtering. The alloy selected for this study was $(Mo_{0.6}Ru_{0.4})_{82}B_{18}$. This particular alloy is a good glass former and has a very high crystallisation temperature, a property essential to any uses that may be envisaged. Splat quenched alloys of the same composition have already been studied in great detail[15] and this provided a good starting point for the comparative study.

Chapter 2 of this thesis is aimed at solid state physicists with little or no knowledge of the atomic structure of metallic glasses. While it has no pretentions of being an exhaustive review, it begins with brief descriptions of the techniques used to prepare amorphous materials, goes on to develop the theory of diffraction from an amorphous solid[16], and finally discusses the evolution of contemporary ideas on the structure of metallic glasses.

Chapter 3 describes the various experimental procedures used in the course of this work.

In the first section of Chapter 4 a detailed description of the

X-ray data analysis is provided. This is followed by a discussion of the results that constitute the body of this thesis. Also proposed are some other experiments that could be carried out to further help elucidate the structure of metallic glasses.

Finally, Chapter 5 contains the description of some work that substantiates the claim that these materials may have significant technical importance. The mechanical wear resistance of sputtered, amorphous $(W_{0.6}Re_{0.4})_{76}B_{24}$ thin films is reported and shown to be considerably better than that of heat treated 52100 bearing steels. For the sake of completeness and ease of discussion, Chapter 5 not only contains the results of the study, but also includes a description of the experiment and the optimum conditions required during the sputtering process. To avoid duplication, the experimental aspects of this study are not included in Chapter 3.

There is only one general comment that need be made at the outset. All occurrences of the term "atomic structure" are intended to imply "the arrangements of atoms in the condensed matter phase" rather than the structure of the atoms themselves. This is a colloquial usage of the term and certainly does not mean the structure within an atom.

CHAPTER 2

METALLIC GLASSES

§ 2.1 TECHNIQUES FOR THE PREPARATION OF AMORPHOUS ALLOYS

In the previous chapter both the terms "metallic glasses" and "amorphous alloys" have been used, but not entirely interchangeably. A fine, though pertinent, distinction exists. "Metallic glasses" necessarily entail quenching from the liquid phase. It is only under such circumstances that the analogy with oxide glasses is appropriate. "Amorphous materials" or "amorphous alloys" are a broader category of materials of which "metallic glasses" are a subset. Although this distinction is often ignored, it shall be maintained throughout this work. In this section some of the techniques used to make amorphous alloys are discussed. This is by no means a complete enunciation of all possible methods, but rather a brief presentation merely to provide a flavour for the more common laboratory techniques and their respective advantages.

§ 2.1.1 Liquid Quenching

As the name implies, this technique deals with the rapid quenching of the melt and "metallic glasses" has come to be the generic name for all amorphous alloys produced in this way . A necessary implication of all techniques in this category is the rapid removal of heat. This restricts one physical dimension of all metallic glasses to be less than about 50 μm so as to permit efficient heat transfer. There is no fundamental limit on the other two dimensions. The cooling rates obtainable by these techniques range from 10^5 to 10^6 K/sec. Whether these rates are sufficient for glass formation is determined by

thermodynamic and kinetic considerations for the particular alloy system.

The technique originally used by Duwez et al.[17] was the "gun technique." This entailed using a shock wave to propel a molten droplet of the alloy onto a rotating copper cup. The rotation of the cup was thought necessary for good thermal contact, but it turned out that in most cases the molten alloy would wet the copper well enough without this additional centrifugal force. Figure 2.1 shows a schematic diagram of the present version of the gun. This technique is not used much today primarily because the resulting material has a nonuniform thickness (from less than a micron to about 20 μm) and a random shape. This prevents the use of this morphology for either X-ray diffraction studies or for the measurement of physical properties. It is useful, however, if electron diffraction is to be carried out without any artifacts due to chemical thinning.

The next generation technique was the "piston and anvil" technique[18]. Here a molten droplet, typically 100 mg, falling under gravity is caught between a rapidly moving piston and a stationary anvil. The synchronization is done by means of a light sensor which releases a pressurised piston the instant the molten droplet breaks the light beam. Figure 2.2 shows the essentials of this technique. The foils produced are circular, typically 1 to 2 cm in diameter and 20 to 50 μm thick. These foils are readily usable for diffraction experiments and can be cut into strips for the measurement of physical properties. The major advantage of this technique lies in the compromise between the uniformity obtained and a high turnover rate that is so essential in the laboratory when searching for new glass

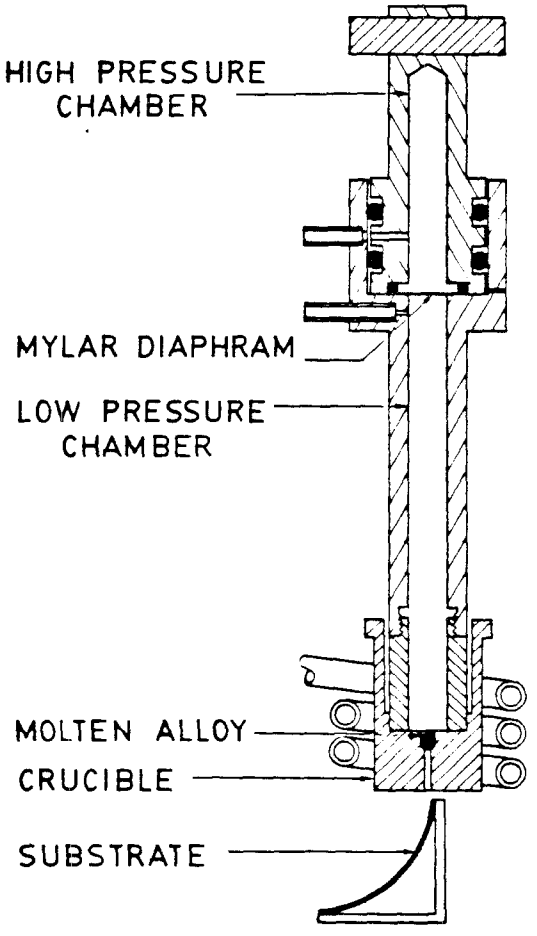

Figure 2.1 The "gun-quenching" apparatus. The molten alloy is propelled by the shock wave created when the mylar diaphram bursts, and is quenched on the substrate.

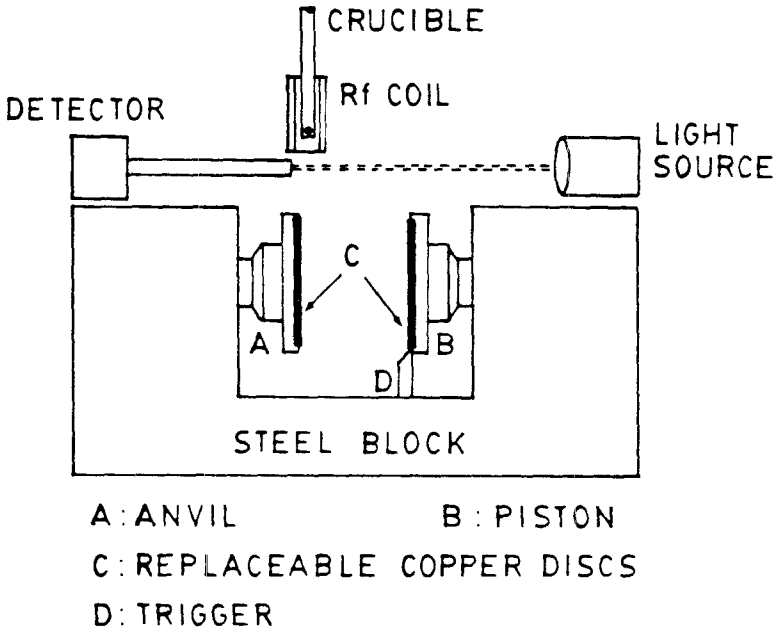

Figure 2.2 The "piston and anvil" apparatus. The falling droplet is caught between the rapidly moving piston and the anvil and quenched on the copper discs.

forming compositions.

The industrially important technique is "melt spinning"[19]. Here a stream of molten alloy impinges on a rotating copper wheel and long ribbons of the amorphous alloy are formed. The width of these ribbons varies between 1 mm and 150 mm. This superficially simple device hides very considerable complexities: for instance, the wheel rotation speed, melt jet diameter and velocity, the angle of attack of the jet, melt superheat, coating and finishing of the wheel and the pressure and nature of the gas in which the operation takes place are some of the variables that influence the cooling rate, geometry, uniformity and in particular the surface finish of the ribbons produced. Details of the methods used to produce wide sheets, of crucial technological importance, have not been revealed by those who have shown the ability to make them. This technique is obviously the most important if technological uses for these materials are envisaged. In the laboratories it is particularly useful if large quantities of samples are required, as in neutron diffraction studies.

§ 2.1.2 Vapour Deposition

Techniques in this category include evaporation, sputtering and chemical vapour deposition (CVD). They are based on the atom-by-atom constitution of the amorphous alloy. If the arriving atoms have a low mobility on the substrate surface, then subsequently arriving atoms will promote amorphous structure formation. All three techniques are very sensitive to the deposition parameters.

In sputtering, a premixed target with the desired composition is bombarded by inert gas ions and these ions transfer sufficient energy to the target so as to propel the constituent atoms towards the

substrates. Each collision between an inert gas ion and the target results in a cascade of collisions between the target atoms themselves, and this further improves the efficiency of the sputtering process. The purity of the argon gas is important. The presence of oxygen in the chamber has been found to facilitate the formation of an amorphous atomic structure[20], while nitrogen has reduced the ability to form an amorphous phase in some cases[a]. Estimated "quench rates" in these processes are $> 10^9$ K/sec and this allows the formation of many amorphous alloys that cannot be obtained by a rapid quenching of the melt. Herein lies one important advantage of these techniques.

While evaporation is generally a much cleaner process than sputtering, the latter is preferred because it retains the composition of the target onto the films. This is generally not the case during evaporation because of differing vapour pressures of the constituent elements. This is an important drawback because, except in the case of intrinsic semiconductor materials, amorphous materials are always alloys. Sputtering is also an important technique if amorphous alloys are to be used as protective coatings from wear and corrosion, since it can be easily scaled up to accommodate industrial applications.

CVD and electrodeposition are very sensitive to the bath composition. This additional parameter restricts the use of the technique. Of singular disadvantage is also the frequent incorporation of hydrogen in the amorphous structure which often has an adverse effect on the properties of the alloys so produced.

---

[a] The introduction of nitrogen gas during the sputtering of Mo-Ru-B alloys resulted in the formation of crystalline phases.

§ 2.1.3 Other Methods

Besides the two categories mentioned above, other techniques exist to produce amorphous alloys. Of these the following deserve mention: laser quenching, ion implantation and solid state reactions.

In laser quenching, an alloy which is to be quenched is heated locally using a laser pulse. When the power is turned off, the rapid thermal conduction causes the molten pool to solidify at extremely fast rates. The same has also been done on alternate layers of elements deposited by sputtering. This enables a close check on the composition and is more tractable in the laboratory. In some cases it also permits the extension of the glass forming range of the alloy due to quenching rates that may exceed 10^{10} K/sec[21].

Ion bombardment has been used for a long time to study radiation damage in metals. Recently, by bombarding multi-layers of certain elements by high energy xenon ions, it was shown that enough damage could be created in the films to produce a structure virtually indistinguishable from vapour deposited amorphous films[22].

Solid-state reactions involve the reaction of multi-layer thin films at elevated temperatures[23]. The process takes advantage of the anomalous fast diffusion of certain elements in a host matrix. Examples are gold in lanthanum and nickel in hafnium or zirconium. Due to the fast diffusion it is possible that the resulting mixture becomes trapped in a metastable (often amorphous) state. In other words, the time scale for the diffusion is faster than the time scale required for the growth of any intermetallic crystalline nuclei that may result from the atomic diffusion. While this technique appears to restrict the glass forming alloys to those consisting of elements that demonstrate

such fast diffusion, this technique could be an important one, were it translated to industrial scales.

§ 2.2 DIFFRACTION FROM AMORPHOUS MATERIALS

X-rays are the most easily available among the various probes of atomic structure. The common laboratory technique for producing metallic glasses, viz. the "piston and anvil" technique and melt spinning, result in morphologies ideally suited for X-ray diffraction. As a result, the bulk of the experimental structural studies on metallic glases have been done using X-rays. For MoKα radiation, typical X-ray penetration depths in metallic glasses vary from 10 to 20 μm. An infinite thickness approximation for a reflection experiment can easily be attained by stacking two or three foils together. At the same time, a single foil is appropriate for transmission experiments. The range of scattering vectors that can conveniently be scanned is 1.5 to 17.5 $\mathring{A}^{-1}$. This is just sufficient to enable meaningful data reduction. This point is discussed in § 4.1 in greater detail.

Electron diffraction, though commonly used to study the crystallisation behaviour of metallic glasses, has not been used to study their atomic structure. The primary reasons for this are the experimental difficulties involved. A large reduction in thickness would be required, and due to possible oxidation and enhanced surface roughness, in comparison to the penetration depth of electrons (a few hundred angstroms in metals) the regions studied may not be representative of the bulk glasses. Furthermore, because we attempt to record a spherical surface (the Ewald's sphere) onto a flat surface (the film), there is a significant distortion for higher values of the scattering vector, $\vec{K}$. This restricts the range of $\vec{K}$ to a smaller

interval than that available in X-ray diffraction and results in less information about the structure.

Neutron diffraction has problems at the other end of the spectrum. Penetration depths of thermal neutrons in metals are so large (tens of millimetres) that the amount of material required often strains the manufacturing process. While typical ingots used in laboratory melt spinning weigh 2 to 3 gm, a total of 20 to 25 gm of materials is often required for neutron diffraction. Also, since the energies of the neutrons are so much lower than that of X-rays, the diffraction process with neutrons is not a "snap shot" of the structure as is the case with X-rays. There is a considerable amount of thermal averaging that occurs during the experiment. This introduces further corrections that complicate the data analysis. The big advantage of using neutrons, particularly from a spallation source, are the very high values of $\vec{K}$ vectors accessible (as high as 30 $\mathring{A}^{-1}$). The other advantage is the possibility of isotope substitution to change the scattering cross-sections without changing, to any appreciable extent, the chemistry of the species in the alloy. This is particularly useful if correlations between given species of atoms are required.

For a crystalline solid, diffraction, be it X-ray, neutron or electron, is the primary tool for structure elucidation. However, it loses much of its power as the translation symmetry in the crystal is lost; it is the constructive interference from these repeat patterns that produces the precise finger-print of the crystalline solid. Nonetheless, it remains the best tool available. If we imagine a collimated beam of X-rays impinging upon a sample and then forming a diffraction image on a film (as in, for example, a transmission Laue

experiment) the pattern produced would vary from a symmetric arrangement of spots for a single crystal to a set of diffuse concentric rings for an amorphous material. The intensity of these rings would decrease from the centre outwards.

Figure 2.3 is a schematic representation of the elastic scattering of X-rays by a solid. It is equally appropriate for any other kind of elastic diffraction. $\vec{K}$ is a measure of the momentum transfer in the process, and is called the "scattering vector." In a transmission experiment $\vec{K}$ lies parallel to the surface of the sample while in a reflection experiment $\vec{K}$ is perpendicular to the sample. This distinction is meaningless for a randomly oriented polycrystalline material, but becomes important for either a single crystal or an oriented microcrystalline solid. The primary scatterers of X-rays in a solid are the electrons. The scattering power of a free electron is hence the standard unit. The ratio of the diffracted intensity (I) to the incident intensity (I_o), for a free electron at a unit distance in the direction of the transmitted beam is 7.94×10^{-26}, and is called an electron unit (e.u.). I/I_o for all experiments is measured in terms of these electron units. For an atom, with the effects of polarisation ignored, I/I_o is isotropic and is the square modulus of the atomic form factor f(K). At K=0, the square modulus of f(K) equals the square of the atomic number Z of the atom, and decreases monotonically for larger K. This decrease is due to the destructive interference from the individual electrons themselves, a result of the fact that the electrons have a spatial extent rather than being point charges, and this spatial extent is comparable to the wave length of X-rays ($\sim$1 Å). In thermal neutron scattering, on the other hand, the nucleus is

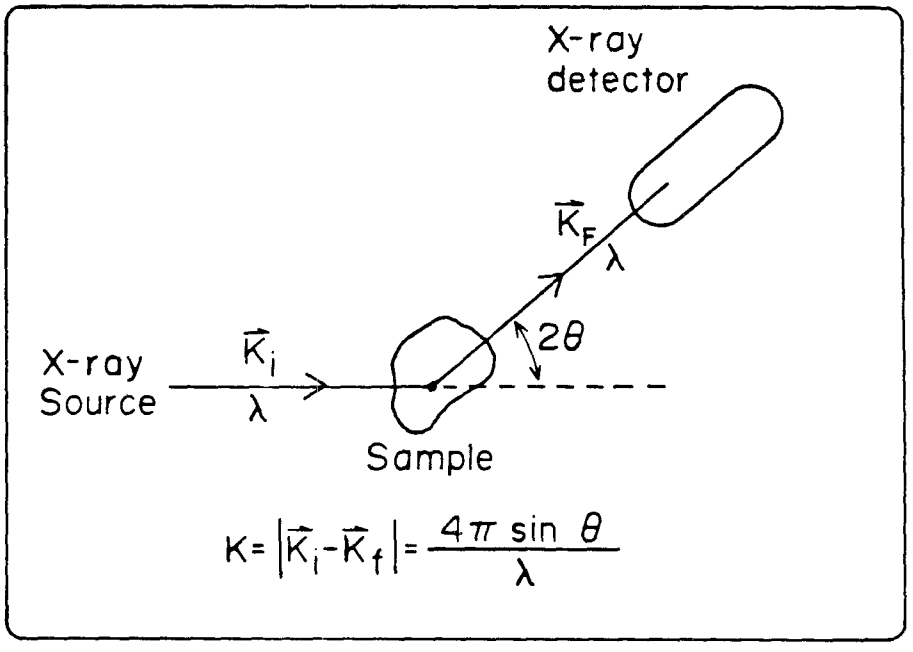

Figure 2.3 A schematic representation of the elastic scattering of X-rays by a solid.

essentially a point scatterer in comparison to the wave length of the neutrons and the analogous nuclear scattering lengths, b, are independent of K.

Let us consider a collection of N atoms of one kind located at $\vec{r}_L$. We may define the number density as[16]

$$\frac{1}{V}\sum_{L}\delta(\vec{r}-\vec{r}_L) ,$$

where V is the total volume containing the N atoms. We can also write the average density as $\rho_o = N/V$. However, when we talk of a distribution of N atoms, rather than try to define the position of each atom (which is quite intractable for a glass) we define the correlations between the various atoms. In this regard we may define $\rho_L(r)$ as the number density of atoms at a point $\vec{r}$ relative to the position of an atom at $\vec{r}_L$. For a glass, since it is not an ordered structure, $\rho_L(r)$ will vary from one site L to another. However, the angular dependence of ρ_L will be completely random as L is varied. We may then define

$$\rho_L(r) = <\rho_L(|\vec{r}|)> ,$$

with the average taken over a thin spherical shell of radius r about the atom at site L. We may note here that for a model of a finite number of atoms care must be taken when treating the atoms near the surface, since those atoms have neighbours on only one side.

There will still be variations in $\rho_L(r)$ from one site to another, especially for small values of r. For example, an eight or nine fold

coordination will result in quite different densities when r is on the order of the nearest neighbour separations. However, for a general amorphous solid we have no way of determining such local structure, and we must sacrifice the detail and average over L :

$$\rho(r) = \langle \rho_L(r) \rangle_L \ .$$

This quantity measures the average number density of atoms at a distance r from an average site.

If we extend these arguments to an n component system of N atoms, then the following expressions result :

The number density of the i^{th} component is

$$\frac{1}{V} \sum_L \delta(\vec{r} - \vec{r}^{\,i}_L) \ ,$$

and the total number density is

$$\frac{1}{V} \sum_L \sum_i \delta(\vec{r} - \vec{r}^{\,i}_L) \ .$$

In addition we define the average density of type i sites as

$$\rho_{oi} = N_i/V \ .$$

With $c_i = N_i/N$ as the concentration of i type atoms, this becomes

$$\rho_{oi} = c_i \rho_o \ . \qquad (2.1)$$

We may now also generalise $\rho(r)$ to $\rho_{ij}(r)$ which now becomes the number density of j atoms, a distance r from an average i type atom.

For a one-component system we may define the radial distribution function (RDF) as

$$RDF(r) = 4\pi r^2 \rho(r) \ . \tag{2.2}$$

Here the oscillations occur about a parabolic base line and it is often more convenient to define the reduced radial distribution function as

$$G(r) = 4\pi r \left[\rho(r) - \rho_o \right] \ . \tag{2.3}$$

For a multicomponent system we have

$$RDF(r) = 4\pi r^2 \ \rho(r) = 4\pi r^2 \sum_{i,j} A_{ij} \ \rho_{ij}(r) \ . \tag{2.4}$$

Here we sum the contributions from various pairs to obtain the total RDF. A_{ij} are weighting factors and in some manner relate to the fact that the correlations between some pairs are more detectable than others.

The total average coordination number for a multicomponent system may be obtained by integrating the first peak in the RDF. That is,

$$CN = \int_o^{r_{min}} 4\pi r^2 \rho(r) \, dr \ , \tag{2.5}$$

where r_{min} is the position of the minimum of the RDF(r) following the primary maximum and $\rho(r)$ has contributions from the various pair

correlation functions as defined by equation (2.4).

All the above information is in principle available from diffraction experiments, and a relationship between it and the raw data can be easily drawn. If atoms of type i are the primary scatterers, then the total distribution of i sites is given by

$$\rho_{ij}(\vec{r}) + \delta(\vec{r} - \vec{r}^{i}) \qquad \left\{ i = 1,2,....N_i \right\} .$$

This describes the distribution of the neighbours plus the distribution of all the central sites of type i. No averaging has yet been performed. This quantity is often discussed as the generalised Patterson function[24]. If an incident wave of X-rays is first scattered off the central atom of type i, and then off a secondary atom of type j, then this scattering will be cooperative if the two atoms are separated by some integral multiple of the X-ray wavelength. In general, the fraction of the incident radiation of wavelength λ, that is scattered through a wave vector $\vec{K}$, is given by the Fourier transform of the distribution of scattering sites. The transform calculates the number of pairs whose interatomic separation has a component along $\vec{K}$ which is $n\lambda$ in length. The relative scattering strength of the atoms are taken into account via their scattering amplitudes (atomic form factors), f_i, which, in general depend on K. The resulting expression for the fraction of radiation scattered is

$$f_i(K)f_j(K) \int \left\{ \rho_{ij}(\vec{r}) + \delta(\vec{r} - \vec{r}^{i}) \right\} e^{-i\vec{K}.\vec{r}} \, d\vec{r} .$$

A sum may be performed over all types j, multiplied by the number of

atoms of type i, N_i, and then summed over i to obtain

$$\sum_{i,j} N_i f_i(K) f_j(K) \int \left\{ \rho_{ij}(\vec{r}) + \delta_{ij}\, \delta(\vec{r} - \vec{r}^{\,i}) \right\} e^{-i\vec{K}.\vec{r}}\, d\vec{r} \,.$$

Here we have included the Kronecker symbol, δ_{ij}, to avoid summing the primary sites again when we sum on j the different types of secondary sites.

This equation includes the volume scattering term, that is, scattering arising from the simultaneous, in phase, scattering from all atoms in the solid. It is conventional to subtract out this volume term which results essentially in a δ-function at K=0 and which can be thought of as the scattering from all i type atoms from an average background of j type atoms and is written as

$$\sum_{j} N_i f_i(K) f_j(K) \int \rho_{oj}\, e^{-i\vec{K}.\vec{r}}\, d\vec{r} \,.$$

Combining the two equations above, the observable intensity may then be written as

$$I_o(K) = \sum_{i,j} N_i f_i(K) f_j(K) \int \left\{ \rho_{ij}(r) - \rho_{oj} + \delta_{ij}\, \delta(\vec{r} - \vec{r}^{\,i}) \right\} e^{-i\vec{K}.\vec{r}}\, d\vec{r} \,.$$

Assuming isotropic scattering, integrating out the term including the delta function, writing the volume integral explicitly and suppressing the K dependence of f(K) for notational simplicity, we have

$$I_o(K) = \sum_i N_i f_i^{\,2} + \sum_{i,j} N_i f_i f_j \int_o^{\infty} r\,dr \left\{ \rho_{ij}(r) - \rho_{oj} \right\} \int_o^{\pi} \mathrm{Sin}\theta\, d\theta\, e^{-iKr\mathrm{Cos}\theta} \int_o^{2\pi} d\phi \,.$$

Solving this integral we have the result

$$I_o(K) = \sum_i N_i f_i^2 + \sum_{i,j} \frac{1}{K}(N_i f_i f_j) \int 4\pi r \left\{ \rho_{ij}(r) - \rho_{oj} \right\} \mathrm{Sin}(Kr)\, dr.$$

We may now define weighting functions $W_{ij}(K)$ as

$$W_{ij}(K) = \frac{c_i c_j f_i(K) f_j(K)}{\langle f(K) \rangle^2} \quad . \tag{2.6}$$

Here $\langle f(K) \rangle = \sum_i c_i f_i(K) = \frac{1}{N} \sum_i N_i f_i(K)$ is the scattering amplitude of the average atom in the alloy. Again, suppressing the K dependence of $f(K)$ and $W_{ij}(K)$ we may write

$$I_o(K) = N \left[\langle f^2 \rangle + \langle f \rangle^2 \sum_{i,j} \frac{1}{K} W_{ij} \int_o^\infty 4\pi r \left\{ \rho_{ij}(r)/c_j - \rho_o \right\} \mathrm{Sin}(Kr)\, dr \right]. \tag{2.7}$$

Since the absolute numbers of atoms are not known, it is desirable to transform the above equation to eliminate explicit reference to them. This can be done by expressing the scattered intensity on a per ideal atom basis, where the ideal atom has unit scattering amplitude. To do this we divide $I_o(K)$ by $N\langle f \rangle^2$ to obtain the scattered intensity per atom, and then normalise this scattered intensity so that in the absence of any pair correlation it is unity. Incorporating these simplifications we may write the interference function, $I_n(K)$, as

$$I_n(K) = 1 + \frac{I_o(K) - N\langle f^2(K) \rangle}{N\langle f(K) \rangle^2}$$

$$= 1 + \frac{1}{K} \sum W_{ij} \int 4\pi r \left\{ \rho_{ij}(r)/c_j - \rho_o \right\} \mathrm{Sin}(Kr)\, dr \; . \tag{2.8}$$

This is the final expression and can be fitted to experimental data. It allows for the fact that f_i, and hence W_{ij}, are K dependent. In most cases these quantities are complex and this can easily be incorporated in equation (2.8)[25].

To relate the interference function $I_n(K)$ to G(r) we first define the reduced interference function as

$$I(K) = K\left[I_n(K) - 1\right] \quad . \tag{2.9}$$

This enables us to write equation (2.8) as

$$I(K) = \sum_{i,j} W_{ij}(K) \int_0^\infty 4\pi r \left\{\rho_{ij}(r)/c_j - \rho_o\right\} \mathrm{Sin}(Kr)\, dr \quad . \tag{2.10}$$

We may define

$$I_{ij}(K) = \int_0^\infty 4\pi r \left\{\rho_{ij}/c_j - \rho_o\right\} \mathrm{Sin}(Kr)\, dr \quad , \tag{2.11}$$

enabling us to write equation (2.9) as

$$I(K) = \sum_{i,j} W_{ij}(K)\, I_{ij}(K) \quad . \tag{2.11a}$$

$I_{ij}(K)$ are the partial interference functions arising from the distribution of the two particular species. Now $W_{ij}(K)$ also take on a physical meaning, namely, the weighting factors that determine the contributions of the various partial interference functions to the total reduced interference function, I(K). The $W_{ij}(K)$ are very slowly varying functions of K and are usually taken to be constant, and equal

to the value at K=0. This is called the Warren, Krutter, Morningstar (WKM) approximation[26], and $W_{ij}(0)$ is given by equation (2.6) with the atomic scattering factors, f_i, substituted by the atomic numbers, Z_i.

Equation (2.10) may also be written as

$$I_{ij}(K) = \int_0^\infty G_{ij}(r)\ \mathrm{Sin}(Kr)\ dr\ , \tag{2.12}$$

where

$$G_{ij}(r) = 4\pi r \left\{ \rho_{ij}(r)/c_i - \rho_o \right\} . \tag{2.13}$$

This expresses the relation between the interference function arising from one pair of species to the reduced radial distribution of one of those species about the other.

Incorporating the WKM approximation and using the fact that by definition $\sum_{i,j} W_{ij}=1$, we can write equation (2.9) as

$$I(K) = \sum_{i,j} \int_0^\infty W_{ij}(0)\ G_{ij}(r)\ \mathrm{Sin}(Kr)\ dr$$

$$= \int_0^\infty G(r)\ \mathrm{Sin}(Kr)\ dr \tag{2.14}$$

where

$$G(r) = 4\pi r \left\{ \sum_{i,j} W_{ij}\ \rho_{ij}/c_j - \rho_o \right\} .$$

This Fourier relationship between I(K) and G(r) permits the transformation of data from reciprocal space to real space coordinates. This is

the route taken when an experiment is carried out. In modelling, on the other hand, a model is either simulated on a computer or made from a collection of balls intended to simulate atoms. The density distribution of this collection of "atoms" is calculated in terms of various $\rho_{ij}(r)$ for a multicomponent system and then equation (2.10) is used to calculate I(K). This I(K) is compared to experimental results and used to judge the particular model.

From equation (2.10) it is evident that a single X-ray experiment cannot yield all the individual ρ_{ij}, because only their weighted sum contributes to I(K). However, since the complex scattering amplitudes, f_i, depend on the wavelength of the probing radiation, it is possible to combine experiments using radiations of different wavelengths to deconvolute the contributions of the various $\rho_{ij}(r)$. For an n component system, n(n+1)/2 experiments are required. Waseda et al.[27] have used this anomalous scattering technique to study the pair correlation functions in Fe-P alloys. Sadoc et al.[28] combined neutron and X-ray scattering experiments to deconvolute the pair correlations in Ni-P and Co-P alloys.

Two other techniques have been used to deconvolute the pair correlation functions $\rho_{ij}(r)$. These are both techniques in which the atomic scattering factors, $f_i(K)$ (or b_i in the case of neutron diffraction) are changed by substituting for certain elements. In X-ray diffraction, two chemically similar atoms, such as zirconium and hafnium are substituted for each other. This is called isomorphous substitution. The assumption is that the two elements are chemically so similar that they do not alter the chemistry of the alloy. This technique has been used by Lee et al.[29] to solve for the pair

correlations in Zr-Ni alloys. The assumption that there is no difference between the atomic arrangements in Zr-Ni and Hf-Ni alloys is made implicitly. Recently, consistency checks have been carried out by Krebs[30] by doing more than three experiments on the pseudo-binary Fe-(Hf,Zr) alloy. He concluded that the above assumption was a reasonable one. There has, however, been no independent confirmation that the Zr-Zr pair correlations in a Zr-LTM glass are the same as the Hf-Hf correlations in a Hf-LTM glass.

The other technique is one of isotopic substitution. Here the neutron scattering length, b_i, of a certain element is changed by using weighted averages of various isotopes. The chemical difference between the different isotopes of a metal is insignificant and not expected to change the structural arrangements in the alloy. This technique appears to work extremely well. Recently, Cowlam et al.[31] have used it to solve for the pair correlations in a $Ni_{64}B_{36}$ glass.

§ 2.3 DEVELOPMENT OF IDEAS ON THE ATOMIC STRUCTURE OF METALLIC GLASSES

Traditionally, two different approaches have been adopted when modelling the structure of metallic glasses. The first approach was to think of metallic glasses as microcrystalline rather than truly amorphous. Models based on this assumption were lent support by the observation that many metallic glasses exhibited broad maxima near the Bragg peaks obtained from corresponding crystalline compounds. It was suggested that the broad maxima were a result of small crystal size and an inhomogeneous distribution of strains and stacking faults[32]. The second approach, perhaps resulting from a more positive outlook, was to think of metallic glasses as frozen liquids. A short range order (SRO) similar to that in the liquid was expected to be retained in

the glass[11]. This approach was certainly reminiscent of that used for silicate glasses.

In the paragraphs that follow, the two approaches are outlined along with their results.

§ 2.3.1 Microcrystalline Models

Probably the first detailed analysis of the radial distribution function as applied to amorphous metals was carried out by Dixmier, Doi and Guinier[33]. They studied a chemically deposited $Ni_{83}P_{17}$ alloy by X-ray diffraction, and concluded that its structure had a greater degree of SRO than observed in liquids. They interpreted the observed diffraction pattern in terms of regions of close packed nickel planes ranging between 5.5 and 11 Å in spatial extension and piled upon each other in bundles that measured up to 20 Å perpendicular to the surface of the planes. Dixmier at al.[33] further mentioned that there was a certain randomness between the bundles and that the phosphorous atom occupied interstitial sites as in Ni_2P or Ni_3P.

The common approach in studies such as the above was to consider line broadening from a small crystallite size and a high density of defects and strains. The former is the easiest to incorporate through the Scherrer formula[34]

$$K^{size} = C\ (2\pi/D)\ .$$

Here K^{size} is the size contribution to the width at half-maximum of a resolved Bragg peak. C is a geometric constant depending on the shape of the crystallites (C = 0.9 for spherical crystallites) and D is the dimension of the crystallite normal to the diffracting planes

(that is along $\vec{K}$). It must be noted, however, that reducing the crystallite size broadens all peaks equally, even though closely spaced peaks may overlap and become unresolved. Broadening due to small crystallite size alone is hence inconsistent with the observed interference functions, in which the first peak is much sharper than the subsequent peaks. The problem with trying to satisfactorily incorporate the effect of defects and strains is to determine what are the relative contributions of the three sources of line broadening.

Cargill[35] studied the Ni-P system extensively and tried to include the effects of all the parameters listed above in his microcrystalline models. In addition to the effect of small crystallite sizes, the effect of strains was incorporated using a Gaussian strain distribution and an expression of the type

$$K^{strain} \simeq 2.4\ K < \varepsilon^2 >^{1/2} ,$$

where K^{strain} is the strain contribution to the width at half maximum of a resolved Bragg peak. K is the position of the peak and $< \varepsilon^2 >^{1/2}$ is the rms strain in the model. He found that he could not reproduce the experimentally obtained interference functions. The problem was invariably in the second peak of the interference functions. While the experimental results showed the second peak to have a high K, low intensity shoulder, the models always had a low K, low intensity shoulder. The results are summarised in figure 2.4.

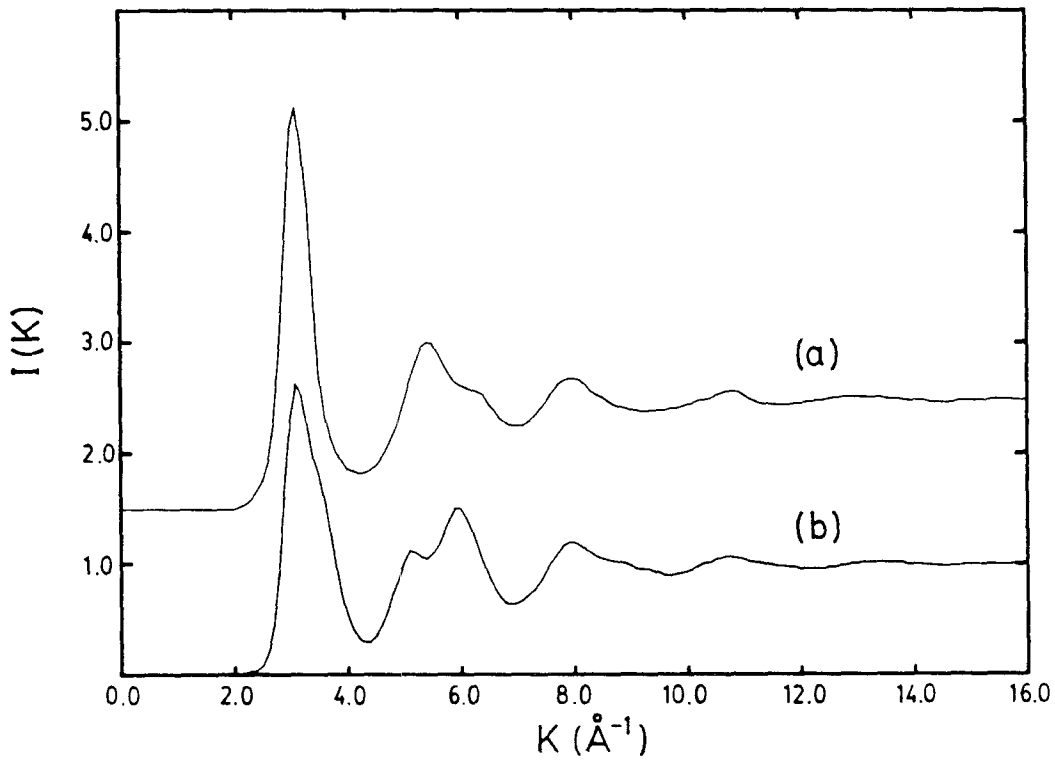

Figure 2.4 A comparison of (a) the experimental data for $Ni_{78.9}P_{21.1}$ and (b) the I(K) from a model of strained fcc microcrystals. The model consists of 512 atoms and has an rms strain of 0.06. [Taken from reference (35).]

§ 2.3.2 Hard Sphere Models

It is natural to compare the structure of a glass to that of a liquid alloy of the same composition. Figure 2.5 shows the radial distribution functions for liquid and glassy $Pd_{80}Si_{20}$[36]. It is evident that there is a better definition of structure in the glass than in the liquid. The low K shoulder in the first peak of the RDF for the glass is attributed to Si-Pd correlations while the main peak represents the Pd-Pd correlations. The average coordination number, as defined by equation (2.5) in § 2.3, is higher for the glassy alloy than for the liquid. This is also borne out by the density increase in going from the liquid to the glass.

Turnbull and Cohen[37] were the first to suggest the use of hard sphere models for metallic glasses. The concept of the dense random packing (DRP) of hard spheres, had been invoked earlier by Bernal[38,39] in an attempt to understand the structure of monoatomic liquid metals. His models consisted of ball bearings that were kneaded in a bladder to obtain maximum density and then frozen in space by pouring in paint, which was then allowed to solidify. The individual coordinates of each ball were then measured using a three-dimensional translation stage. Bernal analysed these models in terms of the polyhedral holes formed between the "atoms." Within the constraint that all polyhedral holes be bounded by edges of equal lengths, Bernal found that there were five such canonical holes. Due to the dense packing of the spheres these holes were necessarily too small to contain another sphere. Figure 2.6 shows these polyhedra. The most ambitious effort was carried out on a collection of 7994 spheres[40] and has been analysed in considerable detail by Finney[41]. Figure 2.7

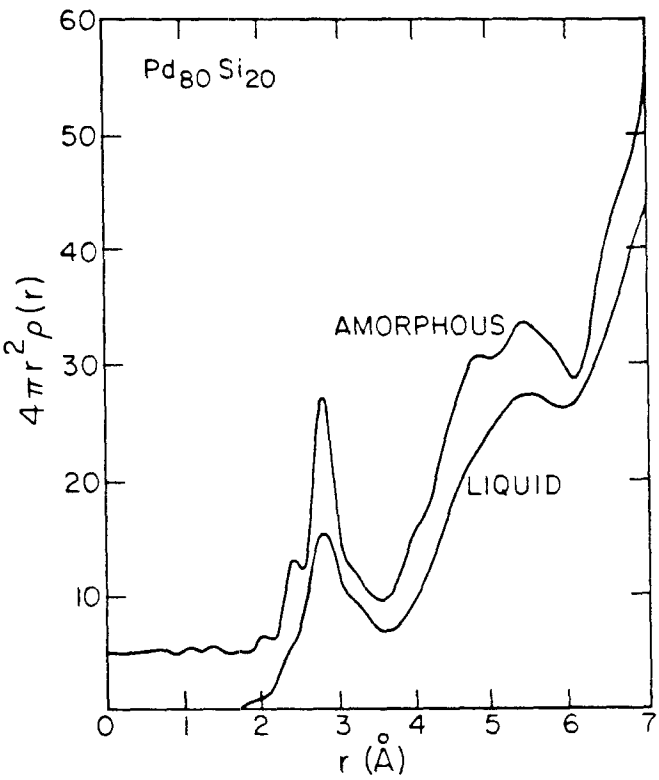

Figure 2.5 The radial distribution function for liquid and glassy $Pd_{80}Si_{20}$ alloy. [Taken from reference (36).]

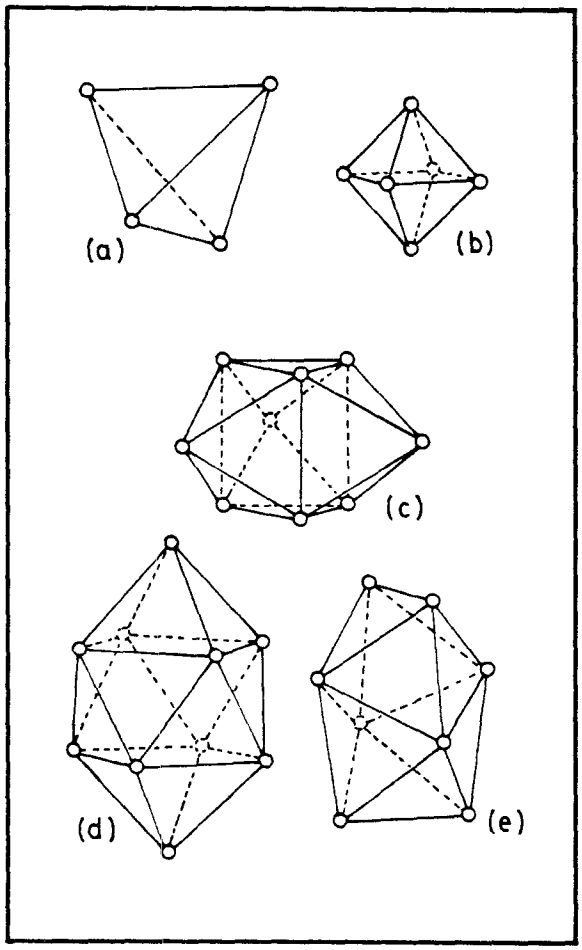

Figure 2.6 The Bernal polyhedra found in a DRP structure of one size spheres; (a) tetrahedron, (b) octahedron, (c) trigonal prism capped with three half-octahedra, (d) Achimedian antiprism capped with three half-octahedra and (e) tetragonal dodecahedra. [Taken from reference (38).]

shows the reduced radial distribution calculated by Finney for the hard sphere assembly, superimposed on the experimental data for Ni-P from Cargill[35]. The agreement appears to be striking. However, the model does not contain spheres of appropriate sizes to represent the smaller phosphorous atoms. Polk[42] suggested that the phosphorous atoms would occupy the larger polyhedral holes (figure 2.6(c)-(e)) in the DRP structure. Based on the number and size distribution of these Bernal holes calculated by Finney[41], Polk determined that with a little distortion, about 20 % of the cages formed in the DRP structure were large enough to accommodate the phosphorous atoms. This number, 20 %, appeared to be significant, because of the empirical findings that most TM-M glasses form near this composition[25]. In addition, this idea satisfied the expectation that metalloid-metalloid nearest neighbours would not occur, just as it was observed for corresponding intermetallic compounds.

Motivated by the similarity between the model and the data in figure 2.7, there have been attempts to simulate DRP models on a computer. Bennet[43] calculated the RDF for a 3999 "atom" model. Figure 2.8 compares his results to those of Finney's. It is evident that the shape of the second peaks in the two models do not compare very well. However, the use of computers made it possible to "relax" these simulated models. von Heimendahl[44] worked on the inner 888 "atom" core of Bennet's model and relaxed it using a Lennard-Jones potential, followed by a softer Morse potential. Figure 2.9 shows the result along with the experimental data for Ni-P alloys[35]. A comparison of figures 2.9 and 2.7 shows that the intensity of the split second peak is modified upon relaxation and better resembles the

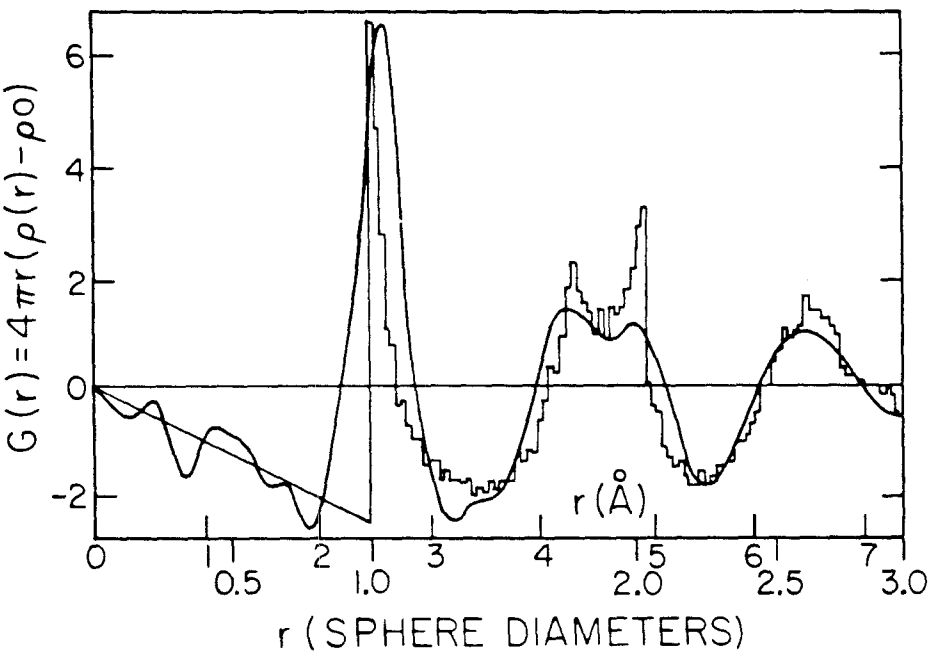

Figure 2.7 The histogram for the radial distribution function obtained by Finney for an assembly of 7994 hard spheres, superimposed on the experimental data for $Ni_{76}P_{24}$. [Taken from reference (25).]

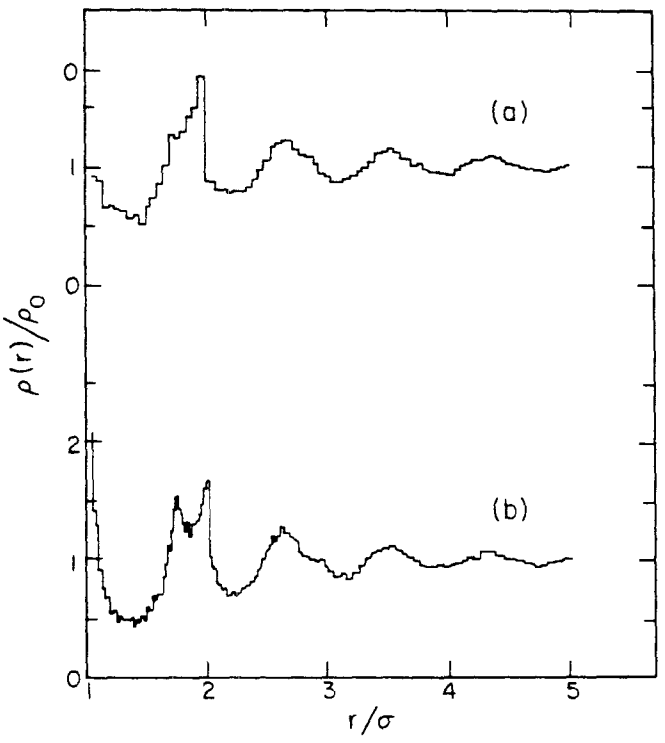

Figure 2.8 A comparison of (a) the normalised density distribution for Bennet's computer model of 3999 spheres and (b) the same result for Finney's DRP model of 7994 spheres. σ is the sphere diameter. [Taken from reference (43).]

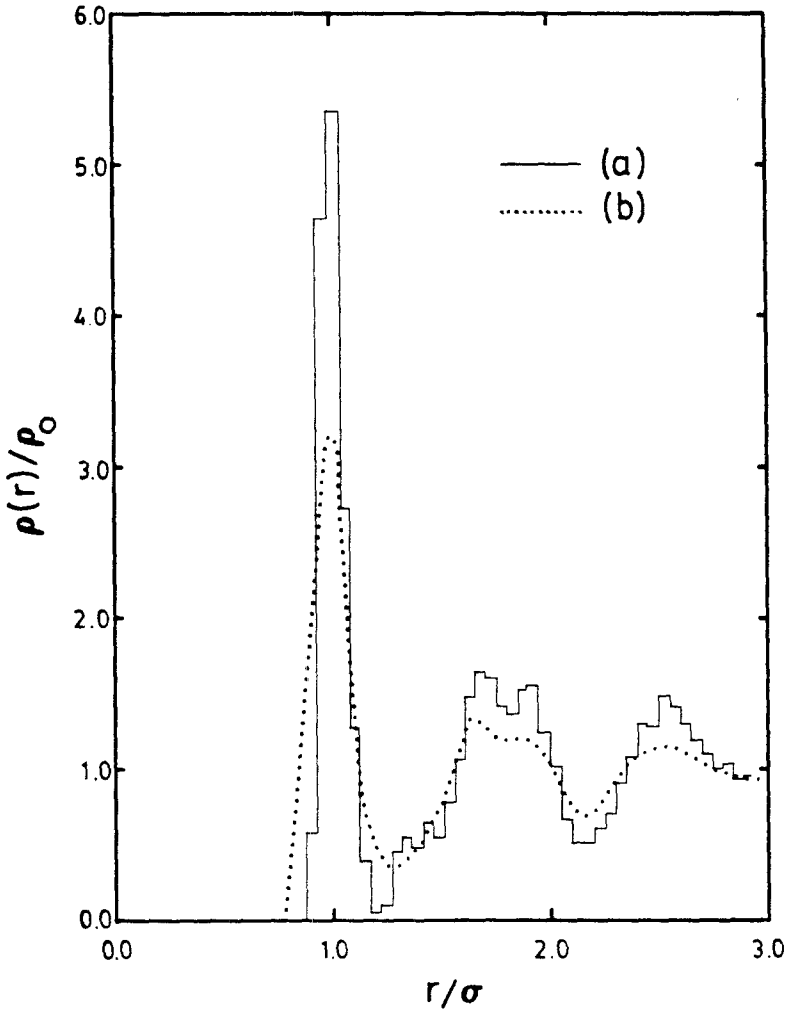

Figure 2.9 A comparison of (a) von Heimendahl's result for the relaxed computer model of Bennet and (b) the experimental data for $Ni_{76}P_{24}$. σ is the hard sphere diameter. [Taken from reference (44).]

experimental data. The agreement of the second and third peak positions between the DRP model and the data is also improved with the use of softer potentials.

There have also been attempts to simulate the DRP of spheres of two sizes, the smaller sphere being intended to simulate the smaller metalloid atom. Sadoc et al.[45] have reported results on aggregates of up to 1000 "atoms." Apart from constraints typical of one size sphere models, they further constrained the smaller spheres to be completely surrounded by large spheres; that is, there were to be no metalloid-metalloid nearest neighbours in their "computer glass." These results are in fair agreement with the data for $Ni_{84}P_{16}$[35]. They have succeeded in reproducing the split second peak with the correct intensity ratios, and have even seen this shoulder vanish for high concentrations of small spheres, as was seen by Dixmier and Duwez[46] for $(Pd_{50}Ni_{50})_{100-x}P_x$ alloys.

Recently, Lewis and Harris[47] have simulated the $Fe_{80}B_{20}$ glass. In addition to the constraint that there be no B-B nearest neighbours, they also monitored the average composition of the cluster at every step of the simulation. The addition of each atom was constrained to bring the average composition closer to the desired value. This avoided the compositional segregation problems that are often associated with two size DRP models[48]. They then used a truncated pairwise Lennard-Jones potential to relax the model.

These additional details, while indicative of the sincere efforts to simulate the structure of metallic glasses, have not really resulted in any significant improvement in the results over those obtained from the relaxation of the one size DRP of hard spheres[44]. The one big

advantage of two size models over one size models however, is the ability of the latter to provide information about the pair correlations that might exist in the glass. This is very important in the simulation of ETM-LTM glasses, where the two atoms cannot be distinguished on the basis of their sizes alone.

§ 2.3.3 Compositional Short Range Order

The structure of Zr-Cu alloys, probably the most studied alloy in the ETM-LTM category, has been modelled by several workers[49,50]. The approach has been to pack spheres representing the two atoms randomly, without any specific constraints on the kinds of nearest neighbours. One manifestation of this scheme is very little SRO. These models are certainly more random than those made for TM-M glasses[44-48]. In this aspect the agreement with experimental results on Zr-Cu is quite good. It is indeed found[49] that not much structure exists in the experimental RDFs for Zr-Cu past the second peak, while in Ni-P alloys even the fifth peak is resolved. The models, however, fail to reproduce the pair correlations observed experimentally in Zr-Cu alloys. While the Cu-Cu and the Zr-Zr distances observed experimentally are fairly well duplicated by the Goldschmidt diameters for copper and zirconium, respectively, the Zr-Cu distance in the alloy is less than the sum of their Goldschmidt radii. This is indicative of a preferred Zr-Cu interaction, an observation supported by the negative heat of mixing between zirconium and copper[51]. Also the Zr-Cu correlation has a much sharper contribution to the first peak of the RDF than any of the other two correlations. In order to reproduce these results Harris et al.[50] arbitrarily introduced a Zr-Cu interaction that was twice as strong as the other two interactions. Upon relaxing the DRP

model with this revised choice for interatomic interactions in a pairwise Lennard-Jones potential, they were able to reproduce the pair correlation functions in a Zr-Cu alloy reasonably well.

This scheme of modelling emphasises the importance of SRO arising from chemistry rather than topology. Such SRO is often called compositional (or chemical) short range order (CSRO).

In the case of a crystalline solid solution, departures from randomness may be characterised in the following manner. The disordered binary alloy is compared to an ideal crystal consisting of "average" atoms at lattice sites. Superimposed on this is an "inhomogeneity" represented by variations in the atomic scattering amplitudes and the static displacements due to the differences in the sizes of the real atoms in the alloy and the "average" atom at the ideal lattice sites. The scattering is then considered as as a superposition of the Bragg peaks from the "average" lattice and a diffuse scattering produced from the fluctuations in the composition and distortions, called Laue diffuse scattering[24]. The chemical fluctuations are described by a short range order parameter, $\alpha(r)$, defined as[24,52]

$$\rho(r) = 1 - \frac{\rho_{12}(r)}{c_2\rho_1(r)} \qquad (2.15)$$

where c_2 is the composition of species 2, ρ_{12} is the density of 2-type atoms around an average 1-type atom and ρ_1 is the total number density

of all atoms around an average 1-type atom. ρ_1 is defined by

$$\rho_1(r) = \sum_{j=1}^{2} \rho_{1j}(r) \quad .$$

For a binary amorphous alloy, a generalised parameter, $\alpha(r)$, may be defined as[53]

$$\alpha(r) = \frac{\rho_{12}(r)}{c_2 \left[c_2\rho_1 + c_1\rho_2 \right]} \tag{2.16}$$

where c_i, ρ_{12} and ρ_i are defined as before.

If the coordination around both the species is the same, as it would be for a solid solution of equal sized atoms, $\rho_1(r) = \rho_2(r)$ and equation (2.16) would reduce to equation (2.15). For a completely random solution we expect $\rho_{12}(r) = c_2\ \rho_1(r)$ and this means that $\alpha = 0$. For chemical ordering, that is, when hetero-coordination is preferred, $\alpha < 0$ and when there is a tendency to cluster (like atom neighbours) $\alpha > 0$. Hence by measuring the pair correlations, ρ_{ij}, between atomic species as defined in § 2.2, it is possible to define the CSRO in terms of the order parameter.

The order parameter may also be defined by measuring what are known as the Bhatia-Thornton[54] partial interference functions, S_{N-C}, and pair correlation functions, ρ_{N-C}. These are applicable only to binary alloys and measure correlations between number and composition fluctuations. The $S_{N-C}(K)$ and the $\rho_{N-C}(r)$ are related through Fourier transforms very similar to equations (2.12) to (2.14)[53]. $\rho_{NN}(r)$, the number-number correlation, measures the density of all atoms a given distance r from an average reference atom. This is the analog of the

Bragg peaks from the "average" lattice. $\rho_{CC}(r)$, the concentration-concentration correlation function, describes the tendency to order. This is the analog of the Laue diffuse scattering. Negative peaks in $\rho_{CC}(r)$ correspond to distances between unlike atoms, while positive peaks indicate a preference of like neighbours. $4\pi r^2\rho_{CC}(r)$ is the mean value of the difference between the number of atoms and the number of j atoms in a spherical shell of radius r and unit thickness about an i atom (i,j = 1,2). The third, $\rho_{NC}(r)$, is a measure of the cross correlation, and contains the effect of the different sizes. $S_{NC}(K)$ relates the fluctuations of the number of atoms in a given volume and the fluctuations of the atomic concentrations in the same volume. $S_{NC}(K)$ and $\rho_{NC}(r)$ both oscillate around zero. If $\rho_1(r) = \rho_2(r)$, then $\rho_{NC}(r) = 0$.

The analysis of diffraction data based on the Bhatia-Thornton formalism is becoming increasingly popular, primarily because $\rho_{CC}(r)$ readily provides visual information regarding any possible CSRO in the alloy. In order to obtain $\rho(r)$, however, there is no direct advantage of one set of pair correlation functions over the other.

CHAPTER 3

EXPERIMENTAL PROCEDURES

§ 3.1 SAMPLE PREPARATION

All the pure elements needed for this study were procured from Alpha products, Massachusetts. The purities and the morphologies of the elements used are listed in table 3.1.

Table 3.1

A list of the purity and the morphology of the elements used.

ELEMENT	PURITY (%)	MORPHOLOGY
Molybdenum	99.995	Crystal bar, chips
Ruthenium	99.97	Powder (-80 mesh)
Tungsten	99.97	Powder (-80 mesh)
Rhodium	99.95	Powder (-80 mesh)
Zirconium	99.94	Crystal bar (Hf impurity)
Rhenium	99.97	Powder (-80 mesh)
Boron	99.8	Bulk, powder (-80 mesh)
Silicon	99.99	Bulk

To prepare alloys of the desired compositions, the constituent elements were weighed to within an accuracy of ± 1 mg. If the element was available only in powder form, it was first pressed into a small pellet and melted independently. This was done so as to eliminate any gaseous impurities that might have been incorporated in the powder. This ingot was then used to prepare the alloys rather than the

"raw" powder. The accurately weighed chunks of the various elements were then induction melted together on a water cooled silver boat. The melting was done in an over pressure of titanium gettered argon. The alloy ingots so produced were broken open and remelted until a visual inspection showed them to be homogeneous.

Small pieces of these ingots (50 to 100 mg) were then splat quenched using the "piston and anvil" technique (§2.1.1). The foils obtained were typically 30 to 50 μm thick.

For the comparative study, sputtered films were made from premixed targets. These targets contained accurately weighed fine powders of the constituent elements. After sufficient mixing, to ensure homogeneity, the powder was hot pressed at 1200 C and 3000 psi to form toroidal targets. The films were sputtered using a d.c. Research S-gun[(a)] magnetron system with argon as the carrier gas.

In planar diode sputtering, figure 3.1(a), as the applied voltage is increased and the pressure in the chamber lowered, the mean free path (mfp) of the electrons increases rapidly. At low pressures this means that the argon ions are created at large distances from the target and are often lost to the walls of the chamber. Furthermore, a large number of primary electrons hit the anode with high energies, a loss of electrons that is not offset by the production of secondary electrons from the cathode. These electrons hitting the anode, which also constitutes the substrate holder, also result in heating and hence damage the films produced.

In magnetron sputtering a magnetic field is used to localise the

---

[(a)] Research S-gun is a registered trademark of Sputtered Films Inc.

(a)

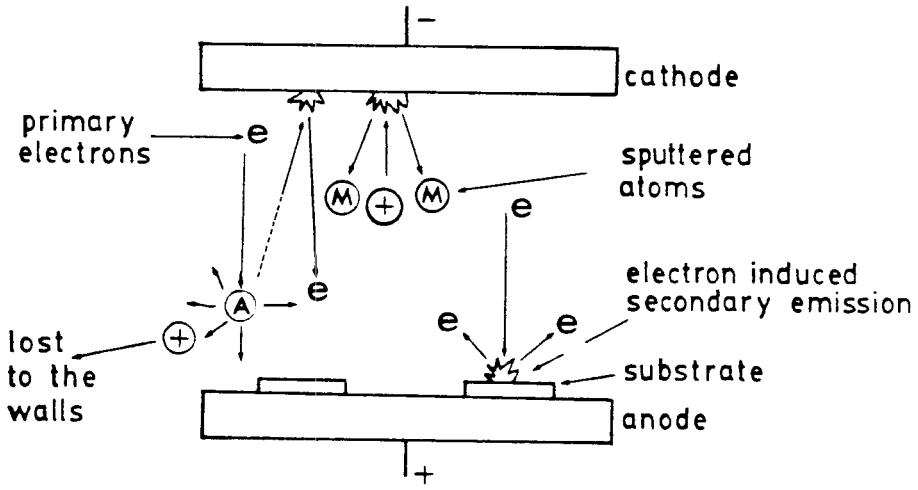

(b)

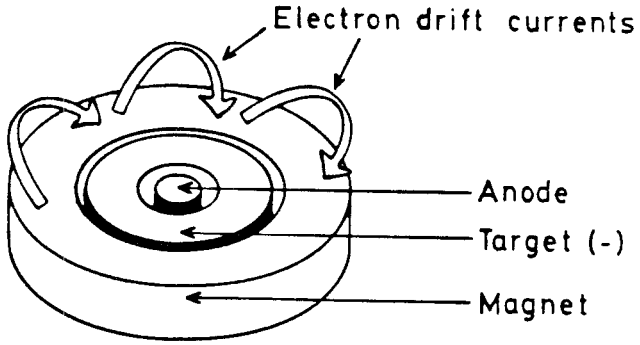

Figure 3.1 (a) A schematic representation of diode sputtering.

(b) The arrangement of the magnet and the target in a Research S-gun.

plasma in a physical proximity of the target. A magnetic field, suitably applied in conjunction with the already existing electric field, exerts a Lorentz force (often called the $\vec{E} \times \vec{B}$ force to denote its direction) on the electrons such that the electron drift currents close on themselves. This localises the electrons to a region of the plasma close to the target. Not only does this increase the ionisation efficiency and permit the use of lower argon pressures (an asset when the incorporation of the carrier gas into the films is undesirable), but it also greatly reduces any damage that might be caused to the films from electron bombardment.

Figure 3.1(b) shows the arrangement of the magnetic field used in S-gun magnetron sputtering. The electron drift paths are also indicated on the figure. Sm-Co magnets are used. They are magnetised along their thickness (generally 2 to 3 cm) and do not corrode easily. The latter property permits them to be placed within a water-cooled cathode assembly.

Figure 3.2 shows a schematic representation of the sputtering chamber used. Typical vacuums obtained prior to the sputtering process ranged from 10^{-7} to 10^{-6} torr. A Varian thermionic emission gauge was used to measure this pressure. To monitor the sputtering pressure (typically in the tens of microns of mercury) a capacitance manometer was used.

The pressure of the gas during sputtering was varied between 5 and 75 μm for the various films produced. The sputtering rate was maintained in the neighbourhood of 350 Å/min and the target to substrate distance was kept constant at about 10 cm. The substrate holder could be water-cooled when desired or simply allowed to float to an

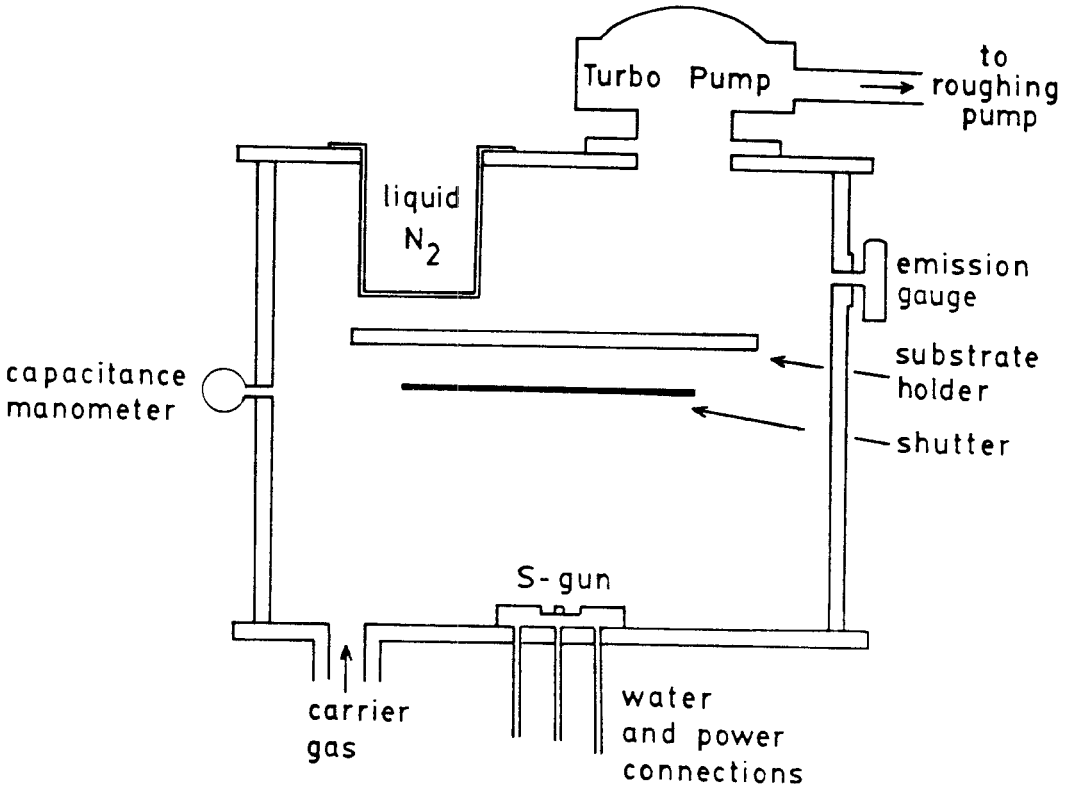

Figure 3.2 A schematic representation of the sputtering chamber used for sample preparation.

equilibrium temperature characteristic of the sputtering conditions. In some cases the radiation from a separate tungsten filament was used to reach a substrate temperature between 300 and 500 C.

The substrates used in the study were glass and quartz slides, mylar, kapton and mica. Often a thermal link was provided between the substrates and the substrate holder through a layer of a low melting Ga-In alloy.

§ 3.2 SAMPLE CHARACTERISATION

Prior to further study, all samples prepared were checked for the absence of any crystalline inclusions. This was done on a Norelco "theta-two theta" diffractometer using CuKα radiation. Only completely amorphous samples were studied further.

While the foils were assumed to be at nominal composition, the films were checked for the incorporation of argon using the energy dispersive analysis of X-rays (EDAX) method. For the films sputtered under low pressures (5 to 10 μm) there was no indication of any adsorbed argon. In the samples sputtered under higher argon pressures (75 μm) there was a noticeable incorporation of argon. The lack of an appropriate quantitative technique, however, prevented us from measuring this amount of argon.

The uniformity of the film, as a function of depth, was ascertained using secondary ion mass spectroscopy (SIMS). It was not possible to get quantitative results from the SIMS analysis because that requires, for purposes of scaling, comparison with a material of known composition and having a similar matrix. An unfortunate situation!

The crystallisation temperatures, T_x, were measured using a

Dupont 1090 thermal analyser in conjunction with a flowing argon atmosphere. In one case (see Chapter 5) the inability to peel the films off the substrates did not permit the use of this technique. A four-point resistivity measurement was used instead. Upon crystallisation, a large, irreversible change in the resistivity of amorphous materials occurs. The temperature at which this sharp drop in resistivity occurs is a good indication of the crystallisation temperature.

Superconducting properties were measured using a four-point probe with copper-beryllium spring contacts. The sample could either be immersed in liquid helium and maintained at 4.2 K or it could be sealed in a can and partially filled with helium gas which acted as a heat exchange medium. When enclosed in the can, a carbon resistance thermometer was used in conjunction with a constantin resistance heater to control the temperature of the sample. The mid-point of the transition was used to determine both, the transition temperature (T_c) and the critical field (H_{c2}) values. Critical current values were taken to be the current at which a 1 μV drop was measured across the sample.

Density measurements were done using the hydrostatic weighing technique[55] with toluene as the working fluid. An average of three or four results has been reported in each case. The error in the measurement, estimated from the least count of the balance and verified by the deviation in the results for the same material, was $\pm$ 0.5 %.

The Transmission Electron Microscopy (TEM) study was done on a Seimens ELMISCOP I electron microscope. The solution used to polish the Ru-Zr-B alloys was of the following composition :

Perchloric acid	6 %
Methanol	60 %
N-Butyl alcohol	34 % .

The polishing was done on an electrolytic jet thinning instrument.

§ 3.3 DETAILED X-RAY STUDY

Detailed and accurate X-ray measurements were performed on a GE XRD-5 scanning diffractometer. A stabilized Phillips XRG-3000 power supply was used in the constant potential mode to power the X-ray tube. To enable data acquisition to a sufficiently high value of K, either MoKα or AgKα radiation was used. The choice of radiation was determined by the elements in the alloy under study. The main consideration was to avoid sample fluorescence of any characteristic radiation close in energy to the incident radiation. The incident radiation was filtered to reduce the ratio of the Kβ to the Kα intensity to about 0.01. A 0.04 inch thick zirconium foil was used with the molybdenum tube while a similar rhodium foil was used to monochromate the silver radiation.

The X-ray tubes used had a 1.5 mm spot width. They were set at a take-off angle of 6° followed by a 1° divergent beam slit. Soller slits were placed immediately after the 1° beam slit to collimate the beam in the horizontal plane. A 0.2° receiving slit was placed in the diffracted beam on the circumference of a circle centred at the sample and defined by a radius equal to the distance between the tube and the sample. Figure 3.3 shows a schematic arrangement of the diffractometer. To eliminate air scattering at low angles, a 3° scatter-Soller slit was placed in the diffracted beam between the sample and the receiving slit. It was found that this eliminated nearly all the air scattering without significantly reducing the intensity of the beam scattered from the sample.

To reduce contributions to the scattered intensity from any

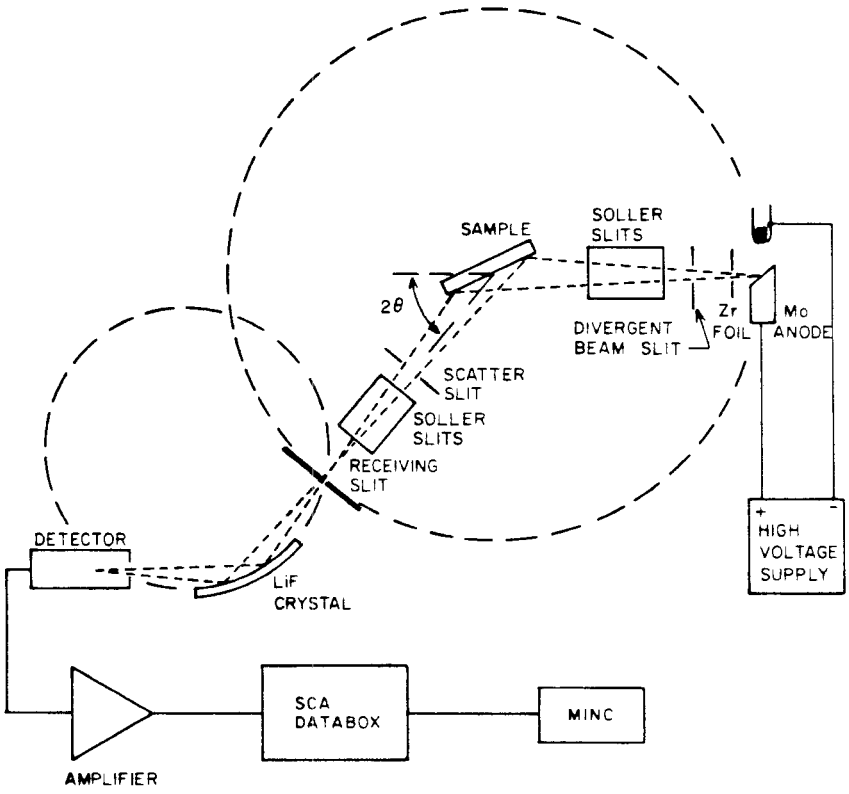

Figure 3.3 A schematic arrangement of the components of the diffractometer used for the X-ray study.

fluorescence or Compton scattering, a LiF focusing crystal monochromator was placed in the diffracted beam. The advantage of LiF over other commonly available monochromating crystals is primarily the large range of characteristic radiations that are usable with LiF. This is made possible by the availability of a small d-spacing coupled with the strong reflection from the (200) planes. The band pass of the monochromator was measured independently for MoKα and AgKα radiations. This was done by first tuning the monochromator for the desired radiation and then scanning in energy with the Bremsstrahlung white radiation diffracted from an oriented $(10\bar{1}1)$ single crystal of quartz (d = 6.6862 Å). For the two cases of MoKα and AgKα radiation the Bremsstrahlung white radiation was obtained from silver and tungsten tubes, respectively. It is important to note that the monochromator was tuned in both cases with a filter in place.

Figure 3.4 shows the experimentally measured band pass of the LiF crystal tuned for the MoKα radiation. For the geometry depicted in figure 3.3, the resolution, that is the full width at half maximum intensity (FWHM), of the crystal is 1.87 keV.

This experimentally obtained band pass was fitted to a Gaussian in $\Delta\lambda$, where $\Delta\lambda$ is the Compton shift given by[24]

$$\Delta\lambda = 0.0486 \, \mathrm{Sin}^2\theta \quad .$$

Since, however, the monochromator does not eliminate all the Compton scattering, this functional form was then used to attenuate the published Compton scattering profile[56,57].

For AgKα radiation the measured band pass had a FWHM of

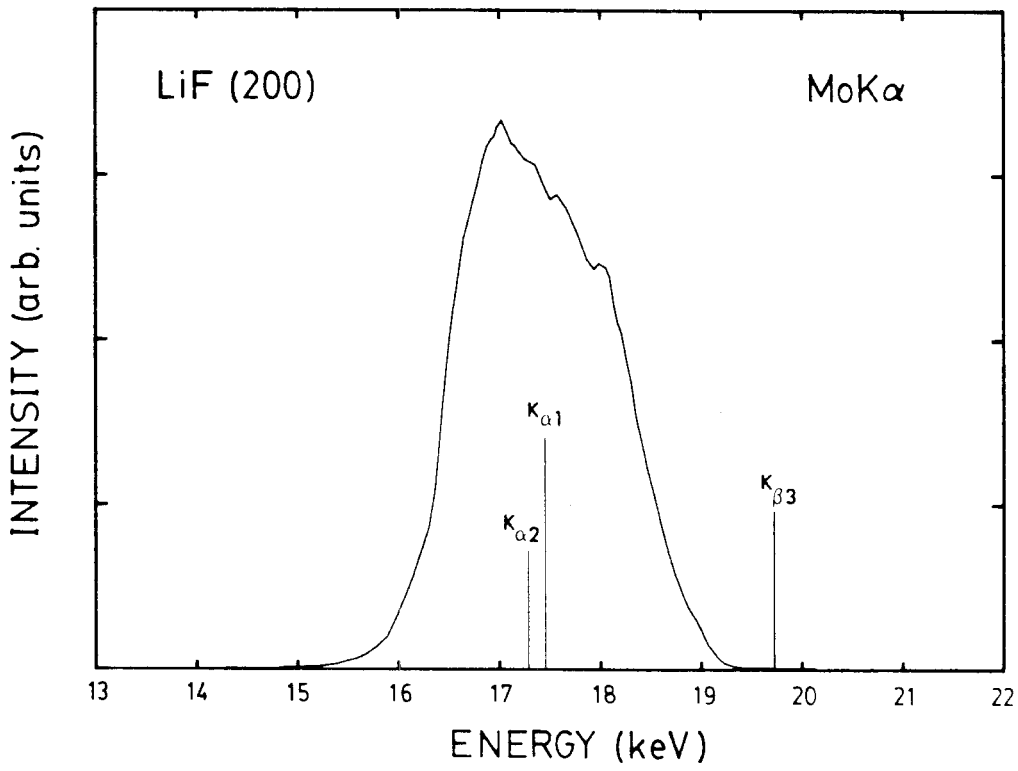

Figure 3.4 The experimentally obtained band pass for the LiF monochromator, tuned for MoKα radiation. FWHM = 1.87 keV.

2.1 keV centered at AgKα .

A Harshaw Scintillation Preamplifier was used as a detector. It consisted of a collimator, a thallium activated NaI scintillation crystal and a photomultiplier tube all in one housing. At its base was mounted a solid state preamplifier particularly suited for energies greater than 4 keV (TiKα = 4.51 keV). The preamplifier was used in conjunction with a pulse height analysing single channel analyser. This permitted not only discrimination against the low energy noise pulses, but also the higher energy radiation (corresponding to $\lambda/2$, $\lambda/3$, etc.) that was passed by the LiF monochromator.

For the experiments done in transmission a single foil was thick enough to provide a good signal to noise ratio. For the reflection geometry it was essential to stack three to four layers of foils using thinned Duco cement onto a glass slide. With this mosaic an infinitely thick sample was simulated and the appropriate absorption approximations could be made (§ 4.1). The films were treated similarly.

The data acquisition was carried out by a microprocessor controlled DATABOX[(a)]. For all the experiments reported here, the same number of counts (10^4) were collected at each data point, thereby restricting the statistical errors in the raw data to within $\pm$1 %. Errors introduced through any low frequency fluctuations in the power supply were reduced by adding the results of two or more independent runs. The data were transfered via an RS 232 line to a Minc PDP 11 computer for further analysis.

[(a)]DATABOX is made by Radix Instruments Inc.

CHAPTER 4

RESULTS AND DISCUSSION

§ 4.1 DATA ANALYSIS

All the alloys listed in table 4.1 were studied using X-ray diffraction. Detailed X-ray data were collected using the experimental arrangement described in § 3.3, for values of 2θ ranging from 10 to 150°.

Figure 4.1 shows the "raw" diffracted intensity from a sample of $Rh_{60}Si_8B_{32}$. This experiment was carried out in reflection. For a flat face reflection geometry it can be shown[24] that in the case of an infinitely thick sample the effect of absorption by the sample is to reduce the intensity by a factor independent of 2θ . With this in mind, the observed intensity may be written as

$$I_{raw}(2\theta) = \frac{1}{A}\left[I_o(2\theta) + I_c(2\theta).R(2\theta).M(2\theta)\right].P(2\theta) + I_{BG}(2\theta) \quad . \qquad (4.1)$$

Here $I_o(2\theta)$ is the intensity of the coherently scattered radiation which appeared in equation (2.7). $I_c(2\theta)$ is the intensity of the modified Compton scattering that is obtained from the literature[55,57]. $R(2\theta)$ is the Breit-Dirac recoil function[58,59] and modifies the intensity of the Compton scattering over that calculated by the classical theory. $R(2\theta)$ is often approximated as unity for heavy elements, although for lighter elements it becomes more important. $R(2\theta)$ may be written as

$$R(2\theta) = \left(\frac{E_{out}}{E_{in}}\right)^3 = \frac{1}{(1 + \frac{2h}{mc\lambda}\,Sin^2\theta)^3} \quad .$$

Table 4.1

A list of all the alloys that were studied using X-Ray diffraction. Also listed is the mode in which the diffraction was carried out.

ALLOY	DIFFRACTION ARRANGEMENT
$(Ru_{0.84}Zr_{0.16})_{54}B_{46}$	Transmission, reflection
$(Ru_{0.84}Zr_{0.16})_{52}B_{48}$	Transmission
$(Ru_{0.84}Zr_{0.16})_{48}B_{52}$	Transmission
$Rh_{70}Si_8B_{22}$	Reflection
$Rh_{65}Si_8B_{27}$	Reflection
$Rh_{65}Si_8B_{27}$	Reflection, transmission
$(Mo_{0.6}Ru_{0.4})_{82}B_{18}$	Reflection

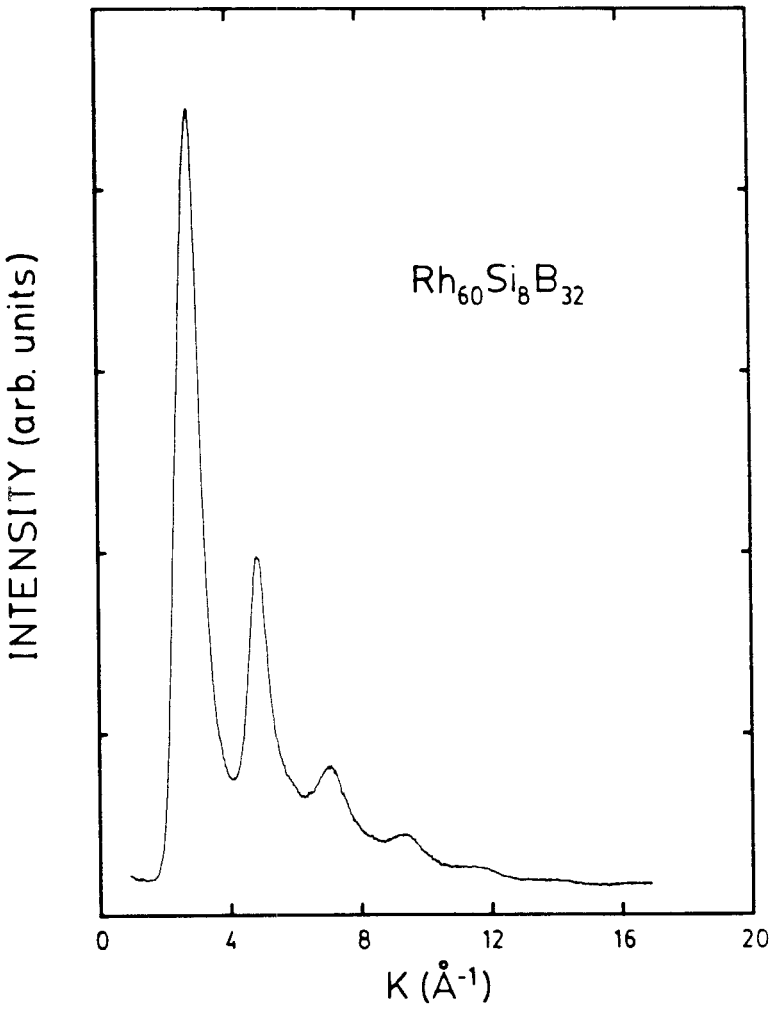

Figure 4.1 The uncorrected diffracted intensity, $I_{raw}(K)$, from a $Rh_{60}Si_8B_{32}$ alloy. This experiment was carried out in reflection.

$M(2\theta)$ in equation (4.1) is the monochromator band pass and has already been discussed in § 3.3. $P(2\theta)$ is the polarisation correction to the intensity. It includes the reduction in intensity due to both, the polarisation from the sample and the polarisation from the monochromator.

$$P(2\theta) = \frac{(1 + \mathrm{Cos}^2 2\beta \, \mathrm{Cos}^2 2\theta)}{2},$$

where 2β is the angle of diffraction through the monochromator. For the reflection of Mokα from the (200) planes of LiF, $2\beta = 20.3^{\circ}$. I_{BG} is the background contribution to the intensity. It arises from sources such as electronic noise, fluorescence, air scattering, multiple scattering and stray radiations. To a first approximation I_{BG} was assumed to be a constant. Finally, A is the normalisation constant, which includes the effects of absorption and also converts the data into electron units (e.u.).

For the transmission experiments the corrections due to absorption are not constant in 2θ, and as such were made explicitly. In this case the analog of equation (4.1) is

$$I_{raw}(2\theta) = \frac{\exp[-\mu\rho \, t/\mathrm{Cos}\,\theta]}{\mathrm{Cos}\,\theta} \left[\; . \; . \; . \; . \; . \; . \; . \; . \; . \; \right], \qquad (4.2)$$

where the term within the brackets is the right-hand side of equation (4.1), t is the thickness of the sample, ρ is the density of

the sample and μ is the average mass absorption coefficient given by

$$\mu = \sum_i w_i \left(\frac{\mu}{\rho} \right)_i \quad .$$

In the above expression w_i are the weight fractions and $(\mu/\rho)_i$ are the mass absorption coefficients of element i. The values of $(\mu/\rho)_i$ were obtained from the literature[60]. The Cosθ term in the denominator of equation (4.2) arises due to the increase in the diffracting volume for all angles other than zero.

The data were converted to e.u. by the "high angle method"[61]. An examination of equation (2.7) shows that in the absence of any correlations $I_o(K)$ goes as $N\langle|f(K)|^2\rangle$. This is also true at large values of K where these correlations are negligible. In the "high angle method" the $I_o(K)$ is fitted to $\langle|f(K)|^2\rangle$ for large values of K, and the factor N absorbed in the constant A. In other words, the fitting was done by minimising the square deviation of $I_o(K)$ from $\langle|f(K)|^2\rangle$ for values of K larger than 8 $\mathring{A}^{-1}$. That is, the expression

$$\sum_{K \geq 8} \left[A.\left(\frac{I_{raw}(K) - I_{BG}}{P(K)} \right) - I_c(K).R(K).M(K) - \langle|f(K)|^2\rangle \right]^2$$

was minimised with respect to A and I_{BG}. The cutoff at K = 8 $\mathring{A}^{-1}$ is arbitrary and was chosen because very little structure was observed beyond this value in the interference function. Figure 4.2 shows the fit to the data shown in figure 4.1.

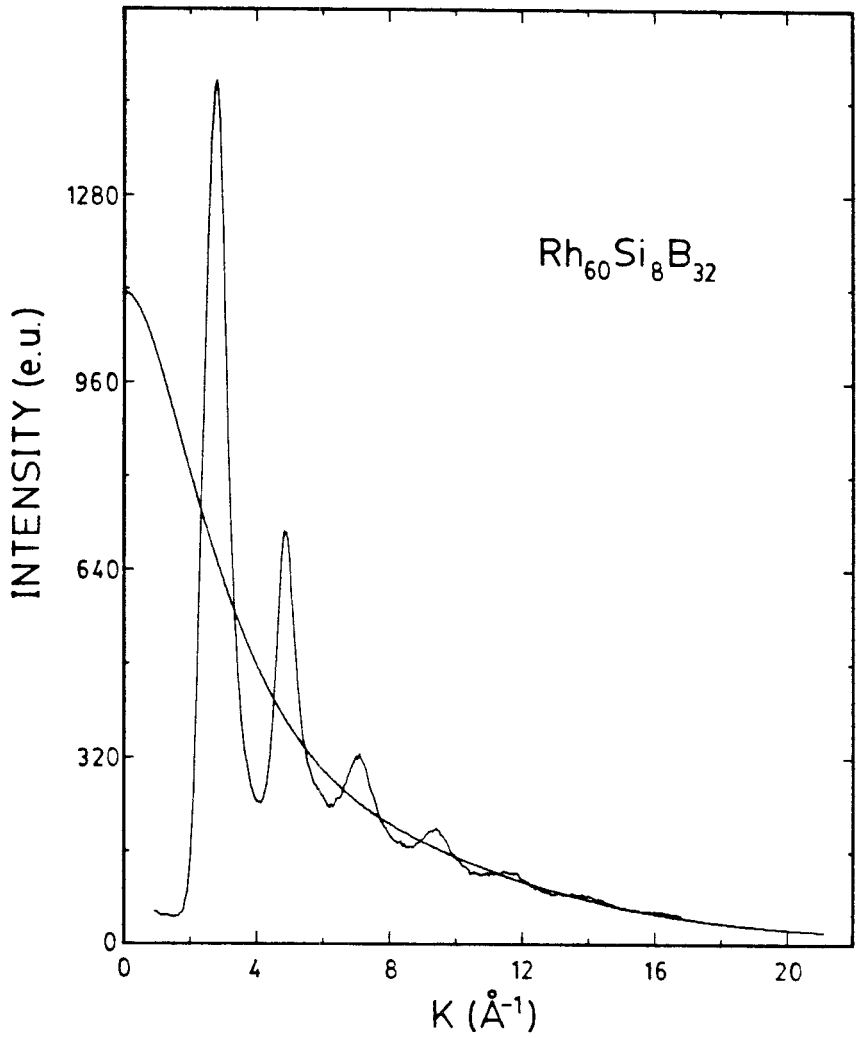

Figure 4.2 The diffracted intensity, $I_o(K)$, from a $Rh_{60}Si_8B_{32}$ alloy, after being corrected for polarisation, Compton scattering and background effects. It has also been converted to e.u. Also shown is the curve for $\langle|f(K)|^2\rangle$, which is a least-square fit to the $I_o(K)$ for $K > 8$ Å^{-1}.

Once A and I_{BG} were determined, $I_o'(K)$ was obtained from

$$I_o'(K) = A.\left(\frac{I_{raw}(K) - I_{BG}}{P(K)}\right) - I_c(K).R(K).M(K) \quad .$$

Since the normalisation constant A includes the number of atoms N, $I_o'(K)$ is simply $I_o(K)/N$. $I_n(K)$ and I(K) were then obtained from equations (2.8) and (2.9), respectively.

Equation (2.14) relates the reduced interference function I(K) to the reduced radial distribution function G(r). It is reproduced below for convenience

$$I(K) = \int_o^\infty G(r)\ \mathrm{Sin}(Kr)\ dr \quad . \tag{4.3}$$

In order to obtain G(r) from I(K) this equation is inverted and written as

$$G(r) = 4\pi r\left[\ \rho(r) - \rho_o\ \right] = \frac{2}{\pi}\int_o^\infty I(K)\ \mathrm{Sin}(Kr)\ dK \quad . \tag{4.4}$$

In an actual experiment, however, the data are accessible only to some finite upper limit, K_{max}. Under these circumstances the above equation must be written as

$$G(r) = \int_o^\infty I(K)\ L(K)\ \mathrm{Sin}(Kr)\ dK \quad , \tag{4.5}$$

where

$$L(K) = \begin{cases} 1 & \text{for } K < K_{max} \\ 0 & \text{for } K > K_{max} \quad . \end{cases} \tag{4.6}$$

Warren[24] and others[25,62] have shown that this abrupt termination of the data results in the broadening of the transform. This particular form of L(K) also results in strong satellite ripples on either side of a true peak. To assist convergence, another factor, U(K), is often introduced within the integral. Two common forms of U(K) are used. The first, an exponential convergence factor, is written as

$$U_1(K) = \exp[-bK^2] \quad , \tag{4.7}$$

where the magnitude of b determines the strength of the damping. The second is the Lorch filter[63],

$$U_2(K) = \frac{\mathrm{Sin}(\pi K/K_{max})}{(\pi K/K_{max})} \quad . \tag{4.8}$$

With the use of such convergence factors the measured G′(r) is really a convolution of the real distribution function G(r) and a modifying function P(r). This convolution may be written as

$$G'(r) = \int_0^\infty G(r') \, P(r-r') \, dr' \quad , \tag{4.9}$$

where P(r) is the Fourier transform of the convergence factor, and given by

$$P(r) = \int_0^\infty U(K) \, \mathrm{Cos}(Kr) \, dr \quad . \tag{4.10}$$

For $U_1(K)$, as defined in equation (4.7), P(r) is also a function of b

and is usually written as P(r,b). The form of P(r,b) has been discussed by Warren[24] in detail. For all the work reported here the Lorch filter was used. It was found to be easier to implement and had the advantage that it went to zero at K_{max}. With the exponential convergence factor, $U_1(K)$, if a small value of b was selected, then $U_1(K)$ was found to be non-zero at K_{max} and resulted in strong termination ripples.

All analysis of radial distribution functions in this thesis has been carried out within the WKM approximation (§ 2.2). For the purposes of calculating $\langle|f(K)|^2\rangle$ and $\langle|f(K)|\rangle^2$ the values reported in the literature for $f_i(K)$ by Cromer et al.[64,65] were used. Figure 4.3 shows the $W_{ij}(K)$ for an $(Ru_{0.84}Zr_{0.16})_{54}B_{46}$ alloy. The W_{ij} are indeed fairly constant over K. It is also evident that in this case the majority of the contributions to the scattered intensity arise from the Ru-Ru, Ru-Zr and the Ru-B correlations. While it is true that $W_{ij}(0)$ is not the best choice for the value of W_{ij} over all K space, it does not really matter since there have been no attempts in this work to deconvolute the pair correlation functions. Other workers[35] have often used the average value of $W_{ij}(K)$ over all K space rather than the value at K=0.

It is possible that due to approximations in the estimation of the background noise, the computed f(K) and errors in the fitting of the data to $\langle|f(K)|^2\rangle$, that a slowly varying function $\varepsilon(K)$ gets added to the true reduced interference function I(K). When the transform of this combined function is taken, the effect of $\varepsilon(K)$ is to introduce oscillations in the low r regions of G(r)[66]. This source of error may be combatted by noting that, physically, $\rho(r)=0$ for values of r

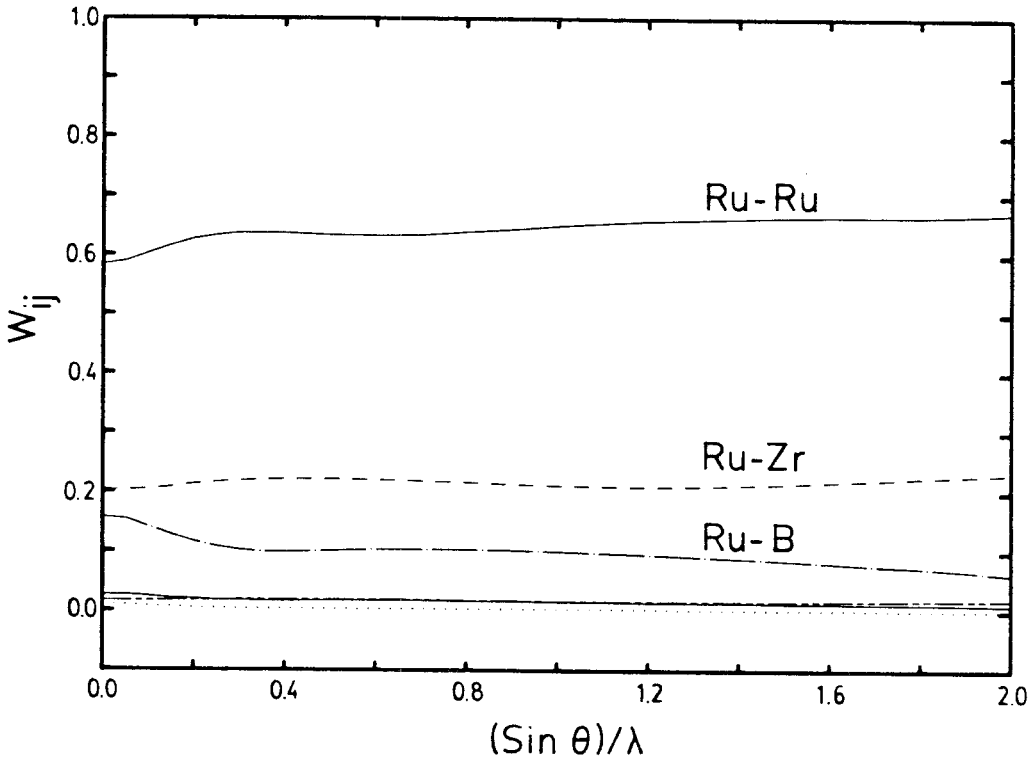

Figure 4.3 The weighting factors, $W_{ij}(K)$ for the alloy $(Ru_{0.84}Zr_{0.16})_{54}B_{46}$. The contributions from B-B, Zr-Zr and Zr-B correlations are all very small, and practically undistinguishable.

less than the nearest neighbour distance (NND), and hence for values of $r < r_{NND}$, $G(r) = -4\pi\rho_o r$. This is a condition placed by the physical constraints of the problem. As such, prior to introducing the Lorch filter, a Fourier transform of the data was taken and the low r data replaced by a straight line given by $G(r) = -4\pi\rho_o r$. After this was done the inverse transform was taken. The effect of this procedure was essentially to, in some manner, deconvolute the $\varepsilon(K)$ from the combined function, $I(K) + \varepsilon(K)$. The inverse transform was smoothened, if desired, multiplied by the Lorch filter and then transformed to obtain the reported values for G(r). On any given alloy series identical data reduction steps were carried out for all compositions. This was obviously done so as to permit meaningful comparisons.

The effect on the FWHM of the transform due to the use of $U_2(K)$ is shown in figure 4.4. The plot shows the Fourier transform of a data set that has been analysed to remove the effects of $\varepsilon(K)$, as discussed above, and the transform of the same data set filtered using $U_2(K)$. The solid line denotes the filtered transform, while the dotted line represents the results of transforming the unfiltered data. There is no significant increase in the FWHM of the transform upon filtering. This is an important observation since it permits one to correlate the FWHM of the first peak with the sharpness of the distribution without any need for correction. It is also worth noting that there is no shift in the peak positions (to within the error of the experiment). There is, however, a decrease in the coordination number (CN) as obtained from equation (2.5). For the case shown in figure 4.4, this decrease is on the order of the error in the estimation of the CN.

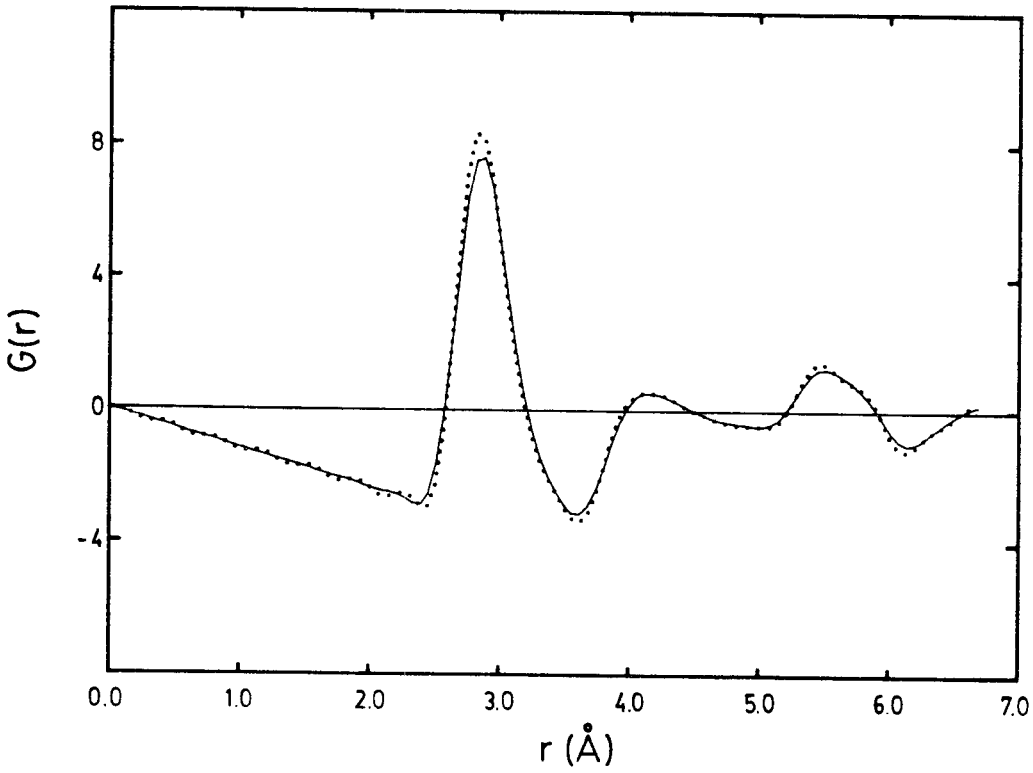

Figure 4.4 The Fourier transform of the real data for a Ru-Zr-B alloy, with (———) and without (•••••) the use of the Lorch filter as a window function.

§ 4.2 HIGH METALLOID CONTENT GLASSES

The metalloid content of most archetypal TM-M glasses ranges between 17 and 25 atomic percent[25]. This empirical observation is probably the single idea that has threaded together the many models proposed for the structure of metallic glasses. Recently, however, with the increasing use of sputtering as a technique to make amorphous alloys, this composition range has been extended. Some metallic glasses with higher metalloid contents have also been made[67-70]. In glasses belonging to the Ru-Zr-B alloy series, for example, the metalloid content is as high as 52 atomic percent. It is evident that the models proposed for lower metalloid concentration TM-M glasses would not be applicable here. For instance, the constraint imposed by Sadoc et al.[45], that there be no nearest metalloid neighbours in the computer simulation of TM-M glasses, would not be applicable to these high metalloid glasses. Also, models such as the one by Polk[42] would be inadequate because of the large fraction of metalloids present in these glasses. In view of these observations it is apparent that there is a need for a radically new approach to the problem. One such approach has been provided by Gaskell[71].

Gaskell noticed that in the compositionally related crystalline phases of most TM-M glasses there is an almost universal occurrence of trigonal prismatic (TP) coordination. The packing comprises six metal (M) atoms forming the vertices of a trigonal prism with a non-metal (N) atom at the centre. This packing of NM_6 trigonal prisms is found in crystalline compounds ranging over wide compositions: from MoP_2[72] to Pd_6P[73]. Based on this observation, Gaskell proposed that TP packing might be the "dominant motif" in TM-M metallic glasses. He

suggested that in the amorphous state it would be the packing of clusters of such trigonal prisms that would attempt to fill all space. As is the problem with all cluster models, there is no *a priori* knowledge about the manner in which these clusters might pack. Gaskell overcame this problem by actually constructing "ball and spoke" models to represent such packing. Starting with a perfect trigonal prism, he added an atom to a rectangular face to produce a prism capped by half an octahedron. One of the triangular faces on the octahedron then provided the base for a new trigonal prism. This process is illustrated in figure 4.5.

The advantage of actually making a physical model was that the builder could see several moves ahead, and to some extent was able to prevent voids. The edge sharing arrangement (for example the edge AB in figure 4.5(b) is common to the two trigonal prisms) adopted by Gaskell was based on the structure of cementite (Fe_3C), in which the new prism is related to the old prism by a clockwise rotation of 215° about the common axis. A random arrangement of prisms was obtained by choosing the common axis randomly, constrained only by the need to avoid overlap and to obtain dense structures. The "ball and spoke" model was transferred to a computer to obtain the exact position of the "atoms". The metalloid "atoms" were then "inserted" in the centre of the trigonal prisms.

Kobayashi et al.[74] have proposed a similar model. They too consider a TP packing, but do not place an edge sharing constraint as done by Gaskell. The manner in which the units are packed in their model is random.

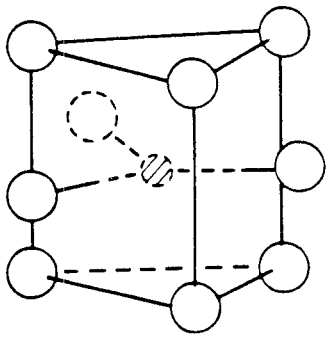

(a)

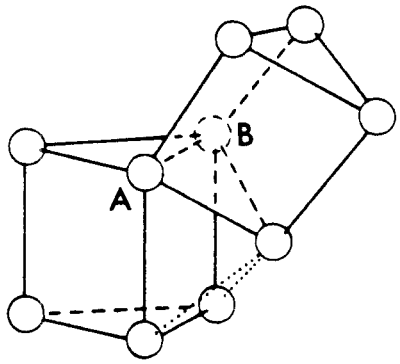

(b)

Figure 4.5(a) A trigonal prism, capped with three half-octahedra.

(b) A second trigonal prism, sharing an edge with the first, with one of the faces of the half-octahedron as its base. This represents the edge sharing scheme proposed by Gaskell[71].

The major implication of such models are the following. First, there is some connection between the structure of the glass and the corresponding crystalline phases. Secondly, since the packing of the trigonal prisms can be in many different ways, with a single or no metalloid atom within each prism, a wide range of compositions can be simulated. Gaskell has already shown[71] that the edge sharing scheme reproduces the experimentally observed distribution functions for $Pd_{80}Si_{20}$ very well. It therefore appears that the packing of trigonal prisms is a good candidate for explaining the structure of the high metalloid glasses.

§ 4.2.1 The Ru-Zr-B System

As mentioned in the previous section, alloys in the Ru-Zr-B system containing more than 50 atomic percent metalloid were quenched into the amorphous state. The high metalloid content left even the amorphous foils extremely brittle. Due to this brittleness some quenches resulted in fragments. Despite the high metalloid content these glasses were metallic in nature and had electrical resistivities that were within the realm expected for metallic glasses[a].

The ternary alloy $(Ru_{0.84}Zr_{0.16})_{100-x}B_x$ could be made amorphous when quenched from the melt, over the composition range $36 \leq x \leq 54$. The concentration of zirconium in these alloys was found to be extremely critical, and amorphous foils could be obtained only for zirconium concentrations ranging between 6 and 10 atomic percent.

---

[a]The electrical resistivity of amorphous alloys are known to range between about 100 and 220 μohm-cm[75], and the resistivity of the alloys in the Ru-Zr-B series lies near the upper limit of this range.

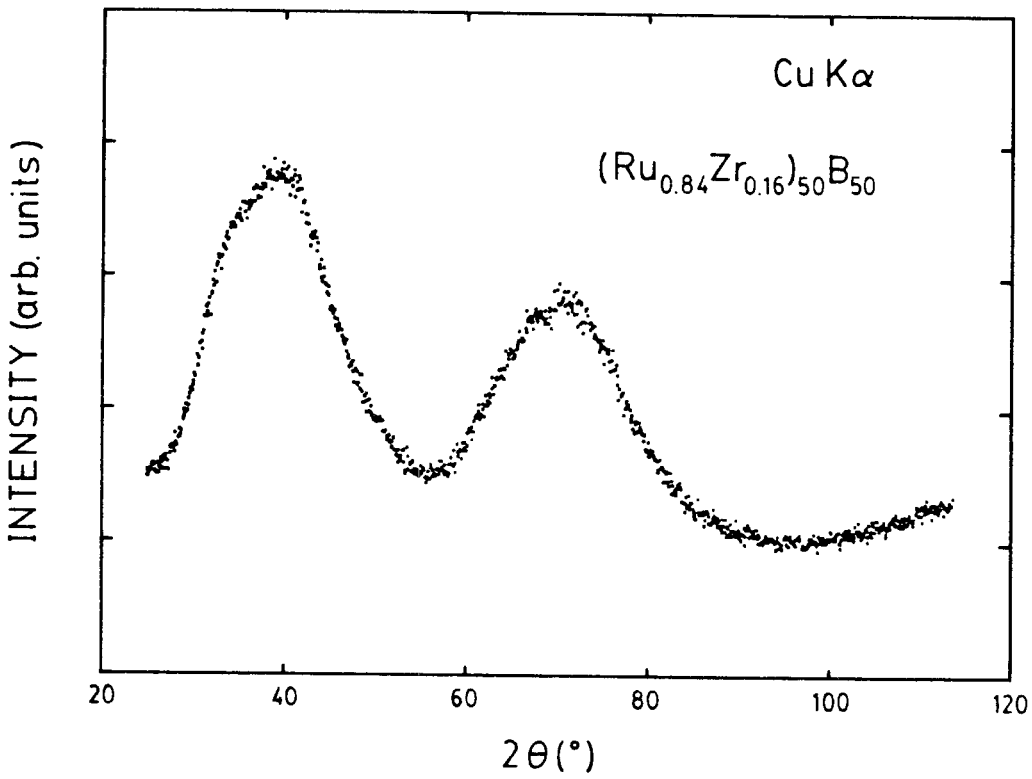

Figure 4.6 An X-ray diffraction pattern for a the Ru-Zr-B alloy with x = 50, obtained using CuKα.

Figure 4.6 shows the diffraction pattern obtained using CuKα radiation from an x = 50 alloy. The first maximum is seen to have a FWHM of 14°. This number is to be compared with the typical FWHM of 5 to 7° for most metallic glasses[76]. This unusually wide band is characteristic of all the high metalloid content glasses. Also interesting to note is the intensity of the second peak. A comparison with curve (a) in figure 2.4 shows the second peak in figure 4.6 to be much more intense than the second peak of archetypal TM-M glasses. The implications of these two observations are discussed in the following pages.

Figure 4.7 shows the reduced interference functions, I(K), for the alloys with x = 46, 48 and 52. Also shown in figure 4.6 are the I(K) for alloy x = 46 in both the transmission and the reflection geometries. One possible explanation for the very intense peaks in the diffracted intensity could be the presence of oriented microcrystals. The similarity between the results in the two diffraction geometries clearly precludes such a possibility.

Figure 4.8 shows the radial distribution functions obtained by Fourier transforming the transmission results in figure 4.7. To emphasize how different these G(r) are from those of archetypal TM-M glasses, figure 4.9 shows the G(r) for the x = 48 alloy and the G(r) for the alloy $(Mo_{0.6}R_{0.4})_{82}B_{18}$. The latter is a pseudo-binary TM-M alloy that has a reduced radial distribution function typical of most TM-M glasses. The G(r)s in figure 4.8 are seen to have a very sharp first peak, followed by very little structure for larger values of r. In fact, the ratio of the intensities of the first peak to the second

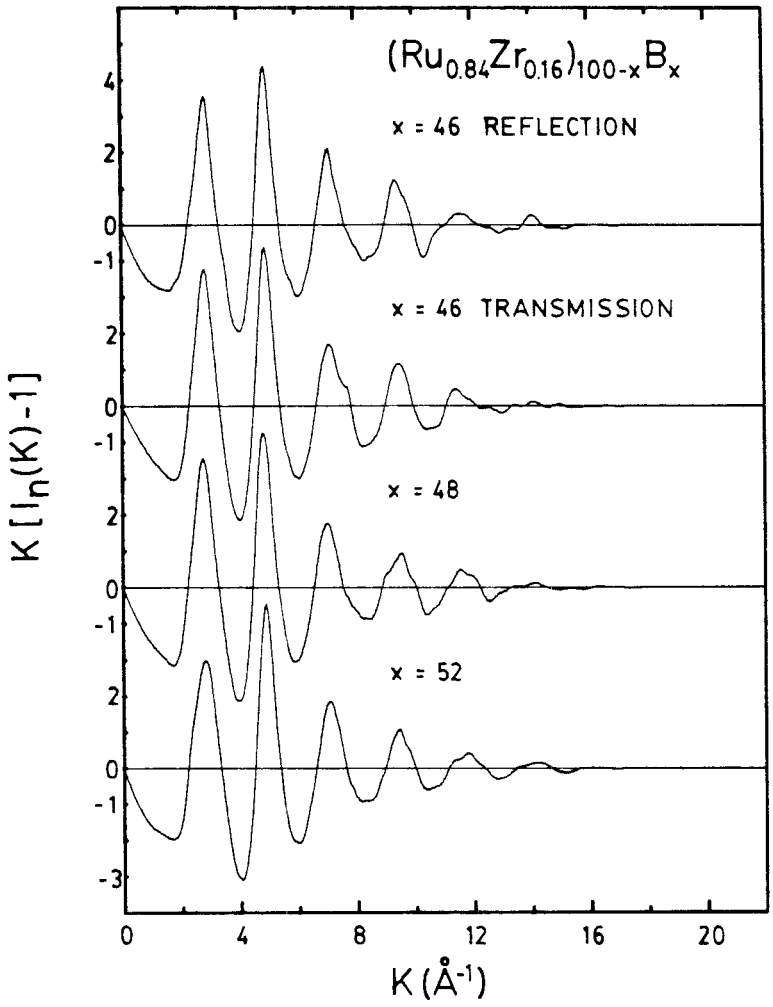

Figure 4.7 Reduced interference functions, $I(K) = K[I_n(K)-1]$, for the three alloys with x = 46, 48 and 52. For x = 46, the I(K) obtained for both the reflection and the transmitted geometries are shown.

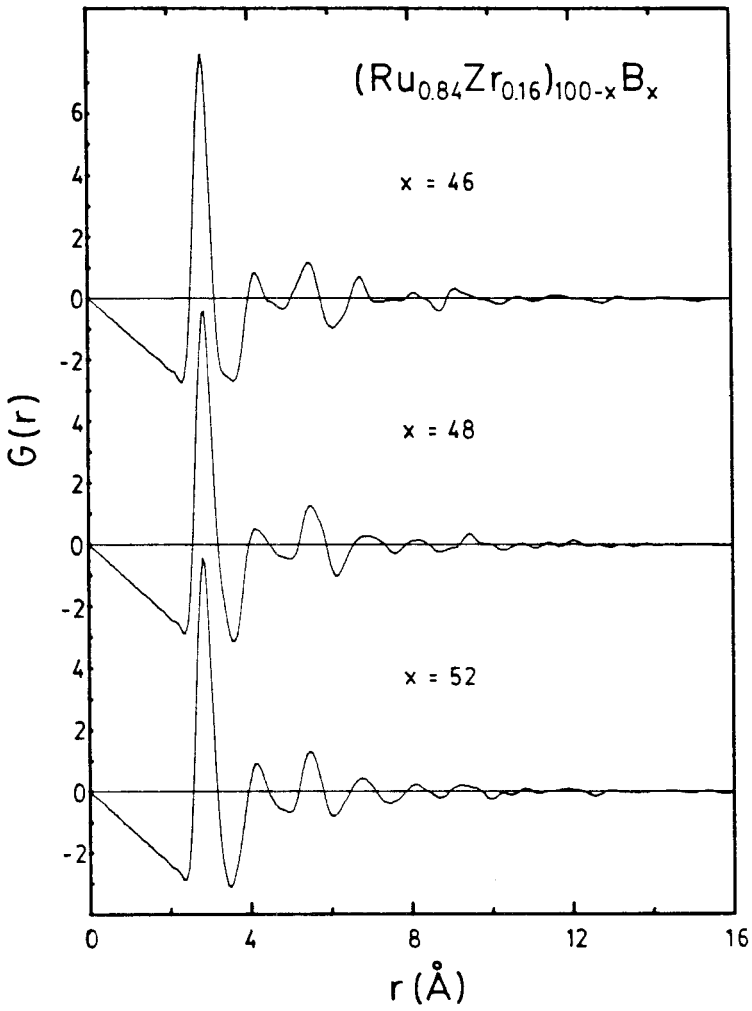

Figure 4.8 Reduced RDFs, G(r), for the three alloys studied in the Ru-Zr-B series.

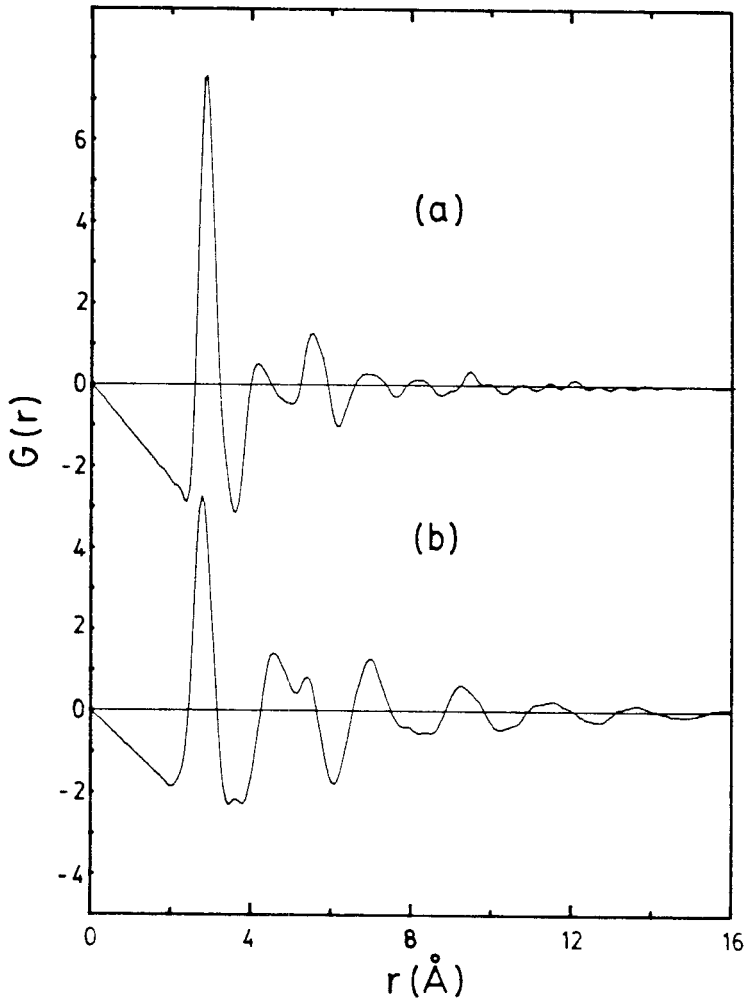

Figure 4.9 A comparison of (a) the G(r) for the Ru-Zr-B alloy with x = 48 and (b) the G(r) for an $(Mo_{0.6}Ru_{0.4})_{82}B_{18}$ alloy.

peak is twice as large as the same ratio for the Mo-Ru-B glass (figure 4.9). The sharpness of the peaks indicates an extremely well-defined nearest-neighbour distance.

Table 4.2 lists the G(r) peak positions, atomic densities and the composite coordination numbers for the alloys studied in the Ru-Zr-B series. Also shown for purposes of easy comparison are the same data for an $(Mo_{0.4}Ru_{0.4})_{82}B_{18}$ alloy. The FWHM, also listed, are for the first peaks in the corresponding $\rho(r)$.

It is at once evident that the two kinds of glasses differ dramatically in their structure. Normalised with respect to the position of the first peak (R_1), Finney's DRP model[41] predicts the position of the second peak (R_2/R_1) at 1.73. The position of the shoulder in the second peak (R_2^{sh}/R_1) was predicted to be at 1.99. In relaxed models[44], and in experimental results on archetypal TM-M glasses, these positions are slightly shifted. R_2/R_1 occurs at 1.63 while R_2^{sh}/R_1 moves down to as much as 1.92. Figure 4.10 shows the origin of these distances in the DRP models. R_2^{sh}/R_1 represents a collineation of three atoms. The maximum value of this distance is 2, as shown in figure 4.10(a). For any deviations from perfect collineation this value would decrease. The maximum at 1.73, shown in figure 4.10(b) represents the distance between the opposite apices of two tetrahedra that have coplanar bases (that is, the opposite vertices of two equilateral triangles with a common side). The third distance, 1.63, occurs when two tetrahedra share a common base. This is shown in figure 4.10(c). Indications are, that upon relaxation of DRP structures, tendencies to form arrangements as in figure 4.10(c) increase, while the probability of arrangements as in figure 4.10(b)

Table 4.2

The peak positions for the G(r) obtained experimentally, the width of the first peak, the composite coordination numbers and the measured atomic densities for the glasses in the Ru-Zr-B series. For purposes of comparison, the same data for the $(Mo_{0.6}Ru_{0.4})_{82}B_{18}$ glass are also listed.

Alloy	R_1(A) $\pm$ 0.01	ΔR_1(A) $\pm$ 0.01	R_2/R_1	R_3/R_1	CN $\pm$ 0.5	ρ(atoms/A^3) $\pm$ 0.1%
$(Ru_{0.84}Zr_{0.16})_{54}B_{46}$	2.83	0.37	1.47	1.94	16.6	0.0922
$(Ru_{0.84}Zr_{0.16})_{52}B_{48}$	2.86	0.38	1.45	1.92	16.2	0.0948
$(Ru_{0.84}Zr_{0.16})_{48}B_{52}$	2.84	0.38	1.46	1.92	15.9	0.0968
$(Mo_{0.6}Ru_{0.4})_{82}B_{18}$	2.77	0.52	1.66	1.93	13.30	0.0716

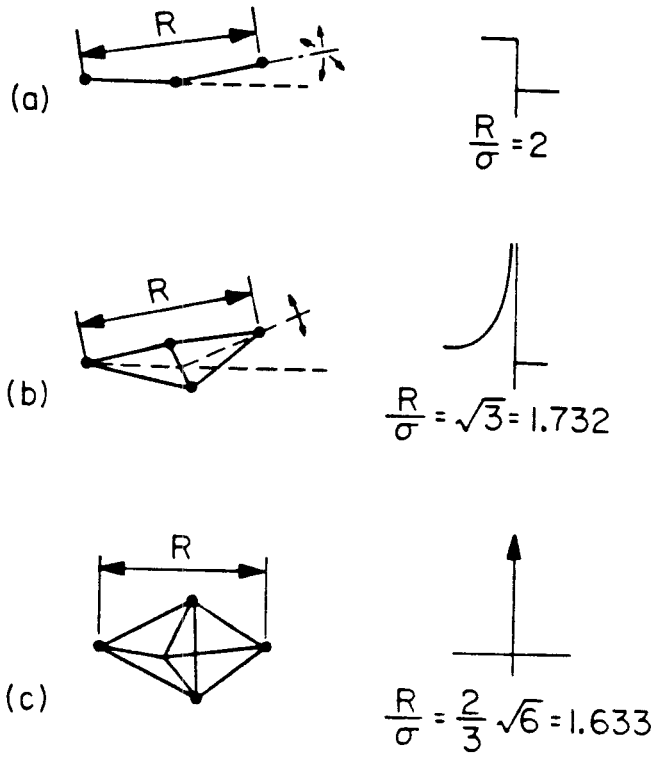

Figure 4.10 Simple connected groups of particles and their discontinuous contributions to the distribution functions in a DRP model. Two darkened circles connected by a solid line indicate two hard spheres in contact. σ is the hard sphere diameter. [Taken from reference (43).]

which lead to the long pseudo-nuclei chains discussed by Bernal[39], decrease.

What is interesting to note, however, is that in the G(r) obtained for glasses in the Ru-Zr-B series, there are no peaks corresponding to the R_2/R_1 distance of 1.63. In fact, the second peak and its shoulder are now two distinct peaks: the first, close to a value of $R_2/R_1 = 1.45$ and the second, close to a value of $R_3/R_1 = 1.92$. R_3/R_1 still denotes an imperfect collineation of three atoms, but R_2/R_1 occurs at a distance close to $\sqrt{2}$. In terms of the packing of Bernal holes (figure 2.6) a $\sqrt{2}$ distance corresponds to the distance between the diagonal atoms in an octahedron. The absence of a peak at this distance in the G(r) for DRP models has often been used to argue[45] that no octahedral coordination exists in archetypal TM-M metallic glasses. Based on the results of figure 4.7, it certainly appears that octahedral coordination is present in these high boron glasses.

Keeping the idea of Gaskell in mind, let us try to explain the observed reduced radial distribution functions. While the structure of intermetallic RuB has been proposed as cubic [77], it has yet to be studied in detail. Crystalline RuB_2, however, is known to have the AlB_2 structure[78]. The unit cell of AlB_2 is hexagonal, as shown in figure 4.11(a), and contains one formula weight. The metal atom is at the origin (0,0,0) and the boron atoms are positioned at (1/3,2/3,1/2) and (2/3,1/3,1/2). This results in alternate planar layers perpendicular to the c-axis, figure 4.11(b). Each metal atom has six equidistant metal neighbours in its own plane and twelve equidistant metalloid neighbours, six above and six below. In the particular case of RuB_2, the length of the a-axis is determined primarily by the B-B

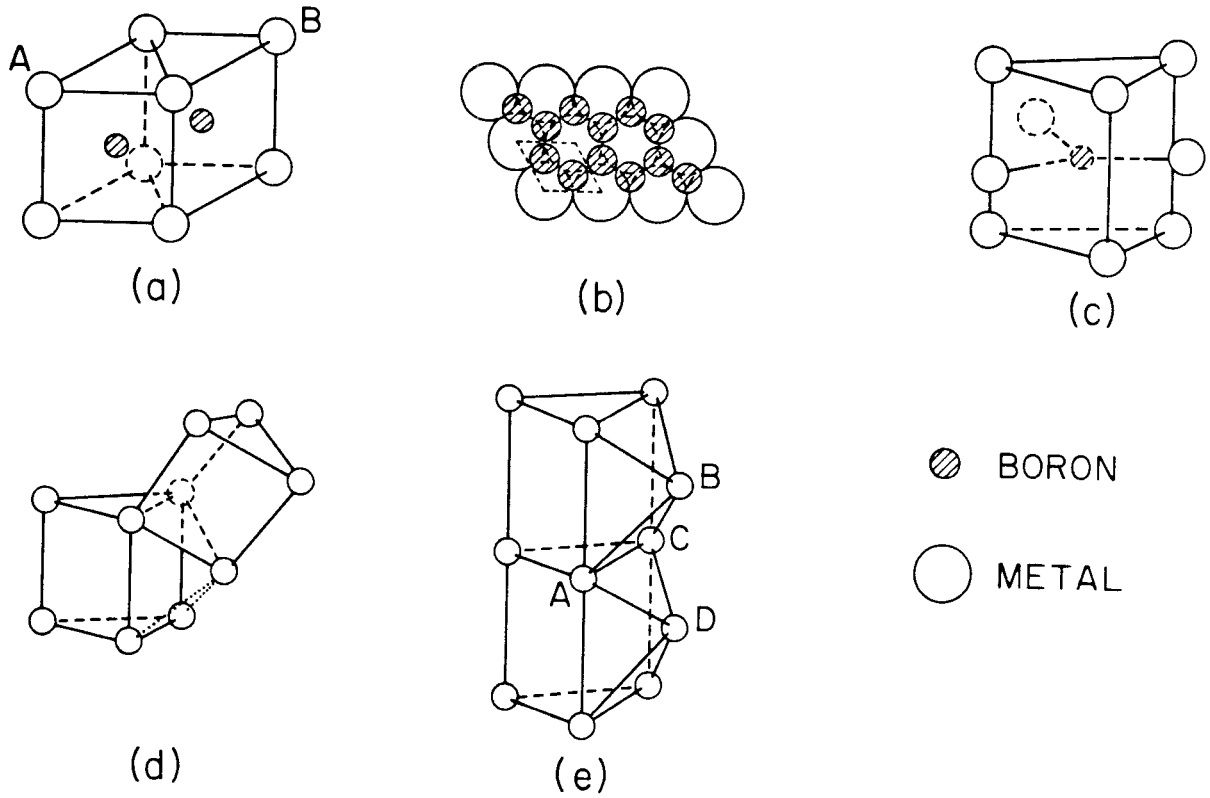

Figure 4.11 (a) Unit cell of AlB_2, (b) Planar layers formed in the AlB_2 structure, (c) a capped trigonal prism, (d) the Fe_3C edge sharing arrangement and (e) TP packing proposed for the Ru-Zr-B glasses. In (d) and (e) only one capping atom has been shown.

distance since the ruthenium atom is relatively small. That is to say, the interstices formed by a close packing of the ruthenium atoms are too small to accommodate the boron atoms without any expansion of the "lattice." It turns out that the Ru-Ru distance in one plane, that is the length of the a-axis, is 2.852 Å, while the length of the c-axis is 2.855 Å. This results in the packing of trigonal prisms with almost square faces (c/a = 1.001). This means that the nearest-neighbour Ru-Ru coordination is now eight, while the nearest-neighbour Ru-B coordination remains twelve.

A comparison with the second column of table 4.2 shows that this prismatic unit reproduces the nearest-neighbour distance of 2.86 Å obtained experimentally for alloy x = 48. Also, the second nearest-neighbour Ru-Ru distance in the crystalline structure is the distance between ruthenium atoms on the diagonal of the square faces, and equals 4.04 Å. The experimentally measured second nearest-neighbour distance varies between 4.14 and 4.16 Å for the three alloys, again in good agreement with the results from the crystalline unit. It thus appears that a packing of these crystalline RuB_2 units may explain the observed reduced distribution functions.

As it exists, there are two problems with the RuB_2 prismatic unit: it suggests a much higher boron content than is actually present in our alloys and it provides a third nearest-neighbour Ru-Ru distance of $\sqrt{3}R_1$. This is the distance between two ruthenium atoms in the same plane which form the vertices of two trigonal prisms sharing a square face. AB depicts this distance in figure 4.11(a). As is seen from table 4.2, no maxima occur at this distance in the G(r)s for the Ru-Zr-B alloys studied.

The first rule, then, for the packing of these trigonal prisms would be that they do not share square faces. Instead, the short range order could be in the form of corrugated chains as in the MoP_2 structure[72], or the square faces could be capped, as in figure 4.11(c), and two trigonal prisms would share only an edge common to their triangular faces as in Fe_3C[71]. Figure 4.11(d) shows this arrangement, and it was this kind of packing that was adopted by Gaskell. Yet another scheme for packing could be that capped trigonal prisms, like the canonical hole of a DRP structure shown in figure 2.6(c), are stacked around and on top of one another. The packing would then be in terms of such capped trigonal prisms with a boron atom within, and the tetrahedra formed between the capping atoms of two layers and the two atoms of the triangular edge in the plane between them. One such tetrahedron is shown by ABCD in figure 4.11(e). The packing in the plane of the capping atoms would be distorted since the undistorted vertex angle of the half-octahedron is about 75°; and this requires 4.8 half-octahedra to fill space. With some distortion, five half-octahedra could share the vertex atom, but this five-fold symmetry of the cluster would still prevent the complete filling of space. This is just what we require for the frustration of the alloy into the glassy state. The distortion would also result in an increase in the AB distance shown in figure 4.11(e) to 2.82 Å, which is almost equal to R_1. This further increases the first nearest-neighbour Ru-Ru coordination and may explain the unusually high composite coordination numbers listed in table 4.2. This structure would then have a significant number of well-defined third nearest neighbours at $2R_1$, and would result in a well-defined peak, rather than just a shoulder, in

the G(r) at that distance . This is indeed what we observe. If only half the prisms contain boron atoms, then the structure would collapse further, adding to the disorder. It would also result in the correct metal-to-metalloid ratio for our alloys.

The role of the zirconium atom is harder to quantify. It is expected that the zirconium atom enhances the disorder in the system. This would explain the lower limit of the zirconium concentration mentioned earlier. As the zirconium concentration is increased, it is possible that the zirconium atom's greater affinity for boron causes it to define its own environment, rather than merely play the role of increasing disorder. This would result in a loss of the glassy state. Attempts to substitute titanium for zirconium were unsuccessful. Ru-Hf-B alloys were , however, quenched into the glassy state.

It is possible to speculate on the possible sites available for the zirconium atom. One such site is that of the capping atom. Were the zirconium atom to be present at this site, its relatively larger size would result in a larger AD distance in figure 4.11(e). This would mean that the percentage distortion required to fit five half-octahedra would be less and easier to accomplish. This would not occur were a smaller atom to replace the zirconium. This may be why the titanium alloys were not good glass formers. This admittedly simplistic argument implies that each zirconium atom would be shared by five trigonal prisms. In an attempt to understand the coordination around the zirconium atoms better, transmission electron microscopy (TEM) was carried out on these alloys, both before and after annealing.

Figure 4.12 shows a bright field micrograph and a selected area diffraction (SAD) pattern for the as-quenched alloy with x = 52. While there does appear to be a mottled structure in the micrograph on a scale of 50 to 100 Å, it is not absolutely certain whether it means phase separation in the amorphous state or whether it is an artifact of the polishing. In any case, the SAD shows a set of diffuse rings, clearly indicative of an amorphous material.

Figure 4.13 shows the single crystal pattern obtained upon annealing the sample at 350 C for 12 hr. Also shown is the pattern calculated[79] for a fcc structure with a zone axis along [110]. The values for A/B and the angles between the [111] and [200] directions obtained from the SAD are within 0.5 % of those reported. This agreement is substantially conclusive and identifies the structure to be fcc. Based on a calibration at the operating conditions of the microscope, the lattice parameter, a, was obtained from

$$a^2 = (h^2 + k^2 + l^2).(\frac{L\lambda}{R})^2$$

where (hkl) are the Miller indices of the plane under consideration, R is the distance between the images of the transmitted beam and the diffracted beam on the film and $L\lambda$ is the calibration constant of the microscope for the particular conditions under which the picture was taken. The value obtained for the lattice constant, a, was 7.340 Å. ZrB_{12} forms a fcc lattice with four ZrB_{12} rhombohedrals per unit cell. The published value[80] of the lattice parameter is 7.408 Å. While the calculated value of the parameter is off by about 1 % (which is approximately the error in obtaining $L\lambda$), it does appear that upon

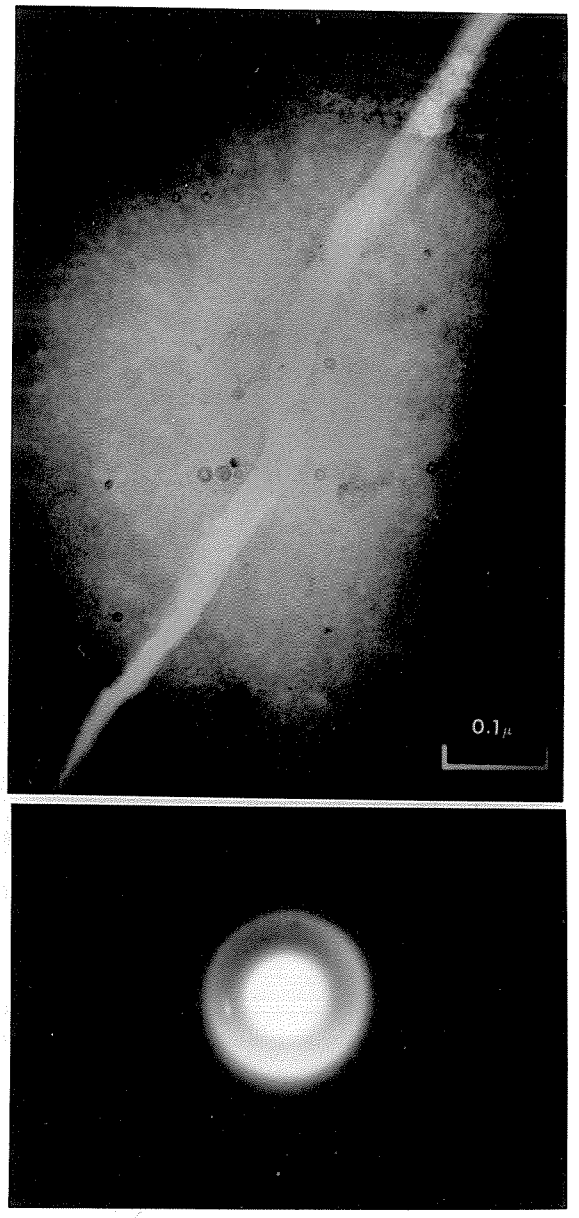

Figure 4.12 A bright field TEM micrograph and a SAD pattern for a Ru-Zr-B alloy with x = 52.

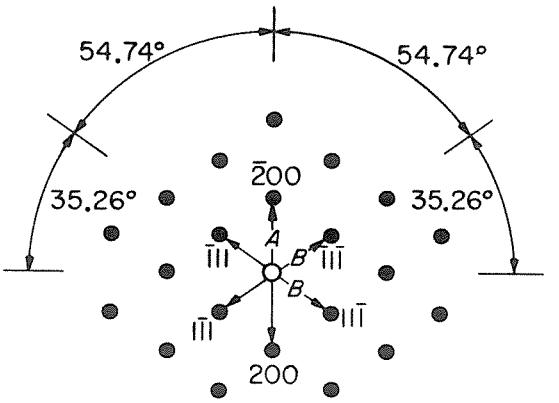

$$\frac{A}{B} = \frac{2}{\sqrt{3}} = 1.155 \quad B = z = [011]$$

Figure 4.13 The single crystal pattern from a region of the sample after annealing at 350 C for 12 hr. Also shown is the calculated pattern for a FCC crystal with a [110] zone axis(79).

annealing, fast diffusion of boron through the lattice permits the formation of the metastable ZrB_{12} phase. As can be seen in figure 4.13, the single crystal pattern is superimposed on diffuse bands, indicating that a significant portion of the amorphous phase remains. This would imply that the ZrB_{12} crystals are formed by the growth upon annealing of quenched-in nuclei. Unfortunately, the crystallisation temperature could not be measured calorimetrically due to the limits of the instruments available, or resistively due to the extremely brittle nature of these materials.

There is no systematic composition dependence of the structure of Ru-Zr-B glasses as understood from the G(r) in figure 4.8. The only observation is that the second and third peaks in the G(r) get better resolved with increasing boron content. This would mean that the third nearest neighbours are better defined as we increase the boron content. This is not unexpected in view of the findings of Boudreaux et al.[81], that the number of trigonal prisms observed in the simulations of Fe-B glasses increased with boron content. While their analysis was restricted to boron contents of up to 25 at.%, it is not entirely unreasonable to extrapolate to higher boron concentrations. With larger numbers of trigonal prisms we would expect more TP clusters, resulting in a better defined third-nearest-neighbour distance of $2R_1$.

The coordination number obtained in all three cases is approximately the same, and this is indeed what we expect since we have proposed that the local coordination in all three glasses is the same. To within the error of ± 0.5 in the composite coordination number, there is no compositional dependence of CN.

These metallic glasses have the highest atomic densities reported to date[15,82]. Further, the density is seen to increase with boron concentrations. This is reasonable since the boron atoms would fill available trigonal prisms without a significant increase in volume. Even though the atomic densities are high, the packing fraction defined in terms of the measured atomic volume, $\bar{V}$, as

$$P_F = \frac{4}{3}\pi \frac{\langle R_g \rangle}{\bar{V}}$$

where R_g are the Goldschmidt radii[83], and the angular brackets denote compositional averages, are typical of most metallic glasses. For instance, for alloy x = 52, $P_F = 0.625$. This is to be compared with a host of metallic glass packing fractions ranging between 0.529 and 0.686, as tabulated by Gaskell[82]. We have used the Goldschmidt radius for boron, rather than a smaller covalent radius, so as to obtain an upper limit on the packing fraction. This typical value of P_F, obtained despite the use of the large value for the boron radius, would lead us to believe that the reason for the high atomic density is the presence of a large fraction of small metalloid atoms rather than a denser packing of atoms.

§ 4.2.2 The Rh-Si-B System

Another ternary system that contains a large proportion of metalloids and can be quenched into the glassy state is Rh-Si-B. Alloys of the nominal composition $Rh_{92-x}Si_8B_x$ with x ranging between 20 and 34 atomic percent were made amorphous. This meant a total metalloid concentration between 28 and 42 atomic percent. It appears that silicon plays a stabilizing role, akin to that of the zirconium in

Ru-Zr-B alloys. Upon quenching alloys with $x < 20$, primary crystallisation of fcc rhodium was observed, while in $Rh_{66}Si_8B_{36}$ the amorphous phase was found to coexist with an unidentified crystalline phase.

The foils produced were very ductile and extremely resistant to chemical attack. In fact, all attempts to thin samples electrochemically for TEM studies were unsuccessful.

X-ray diffraction results on these materials exhibited an extremely broad primary maximum and a large secondary maximum, especially at higher metalloid concentrations.

Figure 4.14 shows the reduced interference functions for three $Rh_{92-x}Si_8B_x$ metallic glasses at $x = 22$, 27 and 32. The trends of increasingly broad primary maxima are clearly observable. In the $x = 32$ alloy we again observe the unusual fact that the secondary maximum is larger than the first. Also, the suggestion that these alloys may consist of oriented microcrystallites is again precluded by the similarity in the I(K) obtained for the two different diffraction geometries (figure 4.14). All indications are that, for the larger values of x, these glasses are quite similar to those in the Ru-Zr-B series.

Figure 4.15 shows the reduced radial distribution function, G(r), obtained for these glasses. The position of the first four maxima are listed in table 4.3 along with the coordination numbers and the atomic densities. The nomenclature for the peak positions is explained in figure 4.15.

The nearest-neighbour distance, R_1, is seen to increase rapidly with increasing boron concentration, and is in all cases

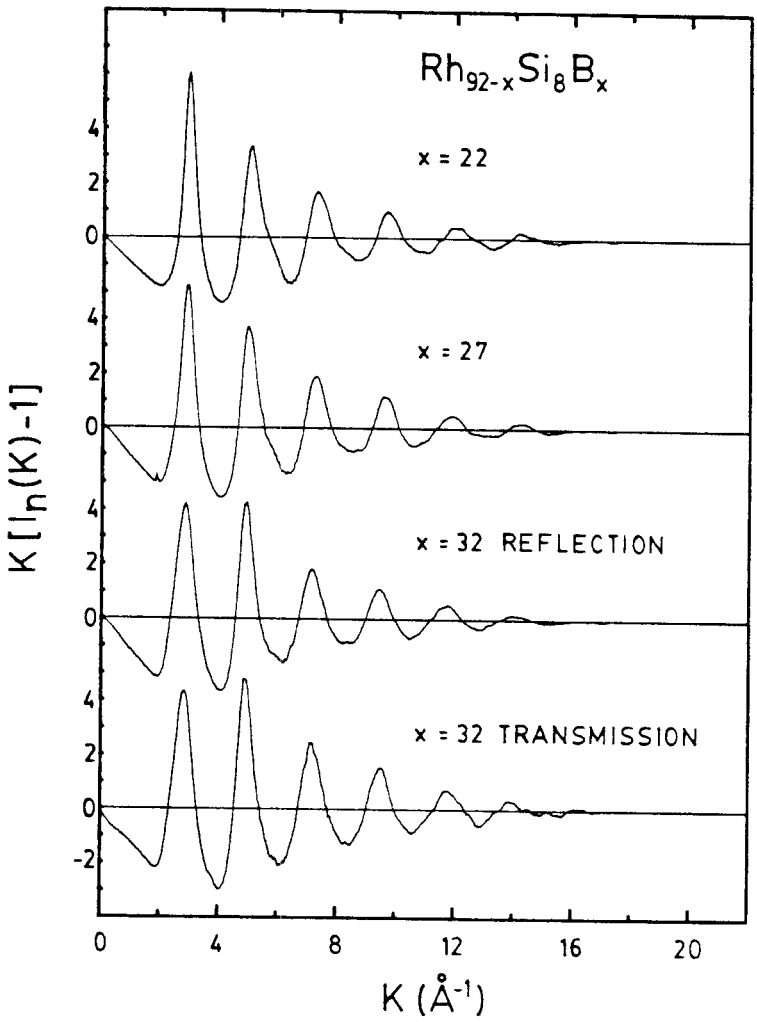

Figure 4.14 The reduced interference functions, $I(K) = K[I_n(K)-1]$, for the alloys in the Rh-Si-B series. Data for both geometries, transmission and reflection, are shown for $Rh_{60}Si_8B_{32}$.

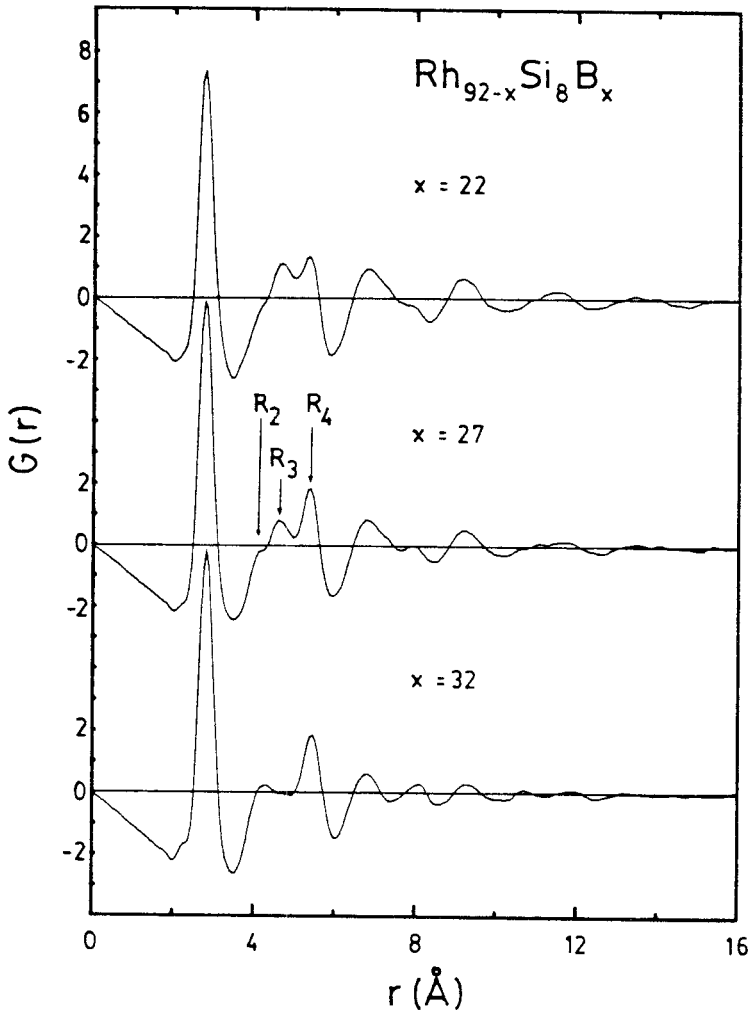

Figure 4.15 The radial distribution functions, G(r), for the three rhodium based metallic glasses.

Table 4.3

The peak positions of the G(r) obtained for the Rh-Si-B glasses. The nomenclature for the peak positions is listed in figure 4.14. Also listed below are the composite coordination numbers, first peak widths and the measured atomic densities of the glasses.

Alloy	R_1(Å) ± 0.01	ΔR_1(Å) ± 0.01	R_2/R_1	R_3/R_1	R_4/R_1	CN ± 0.5	ρ(atoms/Å^3) ± 0.1%
$Rh_{70}Si_8B_{22}$	2.75	0.35	—	1.69	1.94	14.3	0.0816
$Rh_{65}Si_8B_{27}$	2.78	0.37	1.51	1.67	1.93	15.4	0.0847
$Rh_{60}Si_8B_{32}$	2.82	0.38	1.52	—	1.93	16.0	0.0867

larger than the fcc metallic rhodium interatomic distance of 2.68 Å. Also interesting to note is that the peak near $1.67(R_3/R_1)$ disappears and there is a subsequent growth of a distinct maximum near $1.51(R_2/R_1)$ with increasing boron content. The peaks near 1.67 and 1.95 as displayed by the lowest metalloid content alloy, $Rh_{70}Si_8B_{22}$, are typical of the archetypal TM-M metallic glasses. However, the peak at $1.51(R_2/R_1)$ is of unexplained origin. It could be arising in a manner similar to the peak at $1.45(R_2/R_1)$ that occurs in Ru-Zr-B alloys (Table 4.2).

The coordination numbers listed were again obtained by using equation (2.5) and are composite coordination numbers. For these alloys we observe a systematic increase of this composite coordination number with boron content. Presumably this is because of the first coordination shell's being pushed further away, and therefore increasing the CN due to increasing numbers of closely coordinated boron atoms. This is also reflected by the increase in FWHM (ΔR_1) of the alloys with increasing boron content.

It appears that with increasing boron concentration there is a gradual change in the short range order of these alloys. Since the majority of the contributions to the X-ray scattering from all three alloys is due to Rh-Rh correlations and this fraction does not change drastically with the composition (87 % for $Rh_{60}Si_8B_{32}$ as compared to 83 % for $Rh_{70}Si_8B_{22}$), it is expected that the changes observed in the G(r) arise from actual topological changes in the short range order of these metallic glasses. That is to say, it is not likely that the changes are a result of the changes in the contributions of the various correlations.

Despite these peculiarities in their structure with increasing boron concentrations, the physical properties of these alloys do not exhibit any unexpected trends[69].

The density, hardness and electrical resistivity of these glasses behave much like typical TM-M glasses. From table 4.4, the mass density exhibits a predictable decrease with increasing boron concentrations, although the atomic density increases quite systematically. The increasing hardness may, in the simplest case, be due to the increasing rigidity of an ever denser atomic packing. The values for the Vicker's hardness are not particularly high for these alloys, but the trend with increasing boron concentration is typical[84] of archetypal TM-M glasses.

Table 4.4 also shows an increase in the electrical resistivity with increasing boron concentration. This is expected because of the increasing disorder of the glass[a]. All three glasses have a small but positive temperature coefficient of the resistivity, α. While this contradicts the Mooij correlation[85], which predicts that alloys with resistivities larger than $\sim$150 μohm-cm should have a negative temperature coefficient, there is enough scatter in the Mooij correlation to accept this discrepancy. Figure 4.16 shows the low temperature resistivity for the three alloys.

Figure 4.17 shows the high temperature resistivity for these alloys, depicting the crystallisation in $Rh_{60}Si_8B_{32}$ and $Rh_{65}Si_8B_{27}$ at about 525 C. $Rh_{70}Si_8B_{22}$ is seen to have a slightly lower crystallisation temperature and appears to exhibit two distinct

---

[a] As figure 4.15 shows, the distance from the origin over which any order exists decreases as the boron concentration is increased. This is an indication of decreasing short range order.

Table 4.4

The measured physical properties for the glasses in the Rh-Si-B series.

Alloy	ρ(g cm^{-3}) $\pm$ 0.05	V_H(k$_g$ mm^{-2}) $\pm$ 100	ρ_{RT}($\mu\Omega$-cm) $\pm$ 5	α($10^{-5}K^{-1}$) $\pm$ 3%
$Rh_{70}Si_8B_{22}$	10.391	465	152.1	11.6
$Rh_{65}Si_8B_{27}$	10.136	660	185.2	3.98
$Rh_{60}Si_8B_{32}$	9.715	1097	217.6	1.51

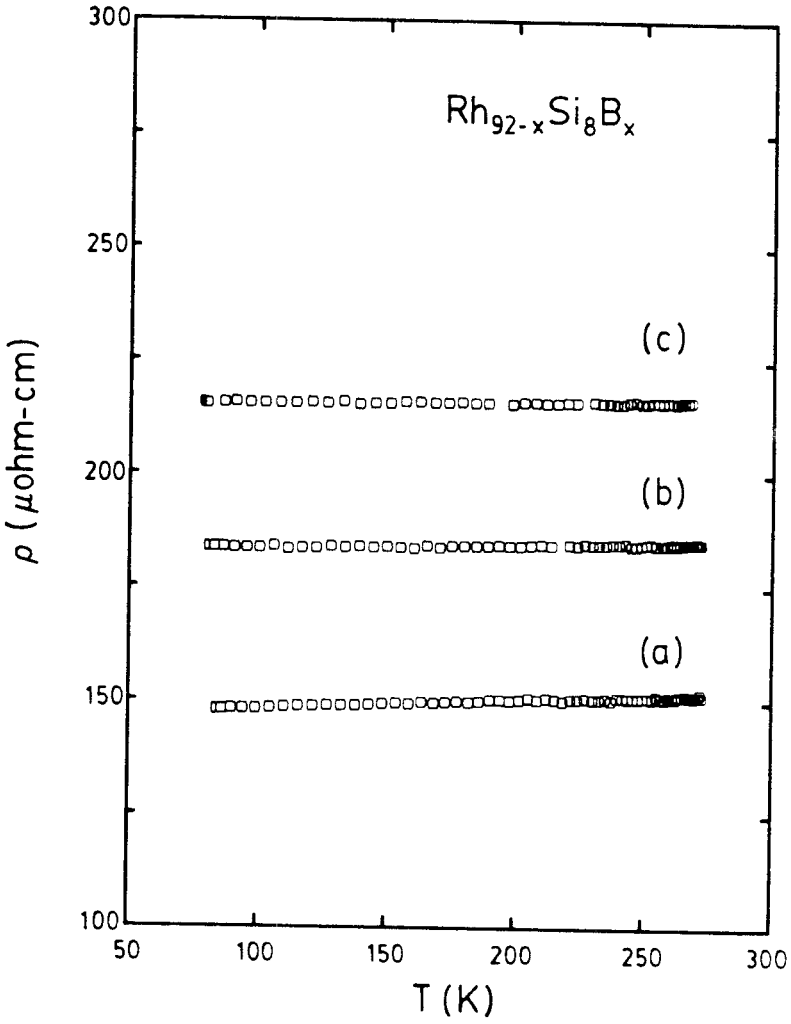

Figure 4.16 The low temperature resistivity, ρ , as a function of the temperature, T, for the rhodium based glasses. (a) $Rh_{70}Si_8B_{22}$, (b) $Rh_{65}Si_8B_{27}$ and (c) $Rh_{60}Si_8B_{32}$.

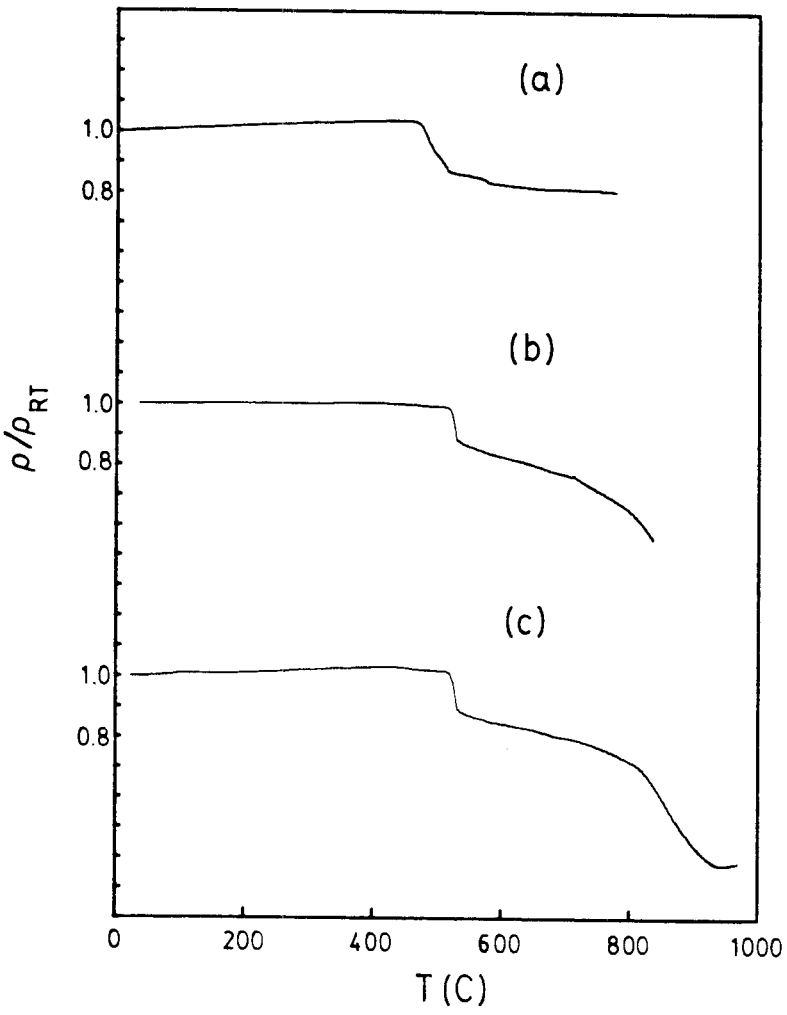

Figure 4.17 The high temperature resistivity, normalised to its room temperature value, for the three rhodium based glasses. A heating rate of about 12 C/min was used. (a) $Rh_{70}Si_8B_{22}$, (b) $Rh_{65}Si_8B_{27}$ and (c) $Rh_{60}Si_8B_{32}$.

crystallisation events. The continued negative slope of the ρ versus T curve after crystallisation indicates that grain growth and segregation continued to temperatures above 950 C for the two alloys with x = 27 and 32. This suggests that diffusion processes and crystallisation kinetics in these alloys are quite slow - a favourable condition for glass formation.

The DTA studies for $Rh_{70}Si_8B_{22}$ and $Rh_{60}Si_8B_{32}$ are shown in figure 4.18. Both alloys exhibit two crystallisation events, though the high temperature event is by far the more significant heat generating reaction in both glasses. For $Rh_{60}Si_8B_{32}$ the DTA experiments were carried out at two heating rates. At 10 C/min, the peak T_{x2} occurs at 815 K while at 50 C/min it occurs at 841 K. From this, an activation energy for the crystallisation, ΔE, can be calculated using the relation[86]

$$\Delta E = k_B \ln \left[\frac{\alpha_1 T_2^2}{\alpha_2 T_1^2} \right] \frac{T_1 T_2}{T_1 - T_2}$$

where T_1 and T_2 are the peak temperatures corresponding to the heating rates α_1 and α_2, respectively and k_B is Boltzmann's constant. For $Rh_{60}Si_8B_{32}$, the activation energy, $\Delta E \simeq 80.4$ Kcal/mol (or 3.48 eV per particle) and is within the range reported for metallic glasses (60 to 150 Kcal/mol).

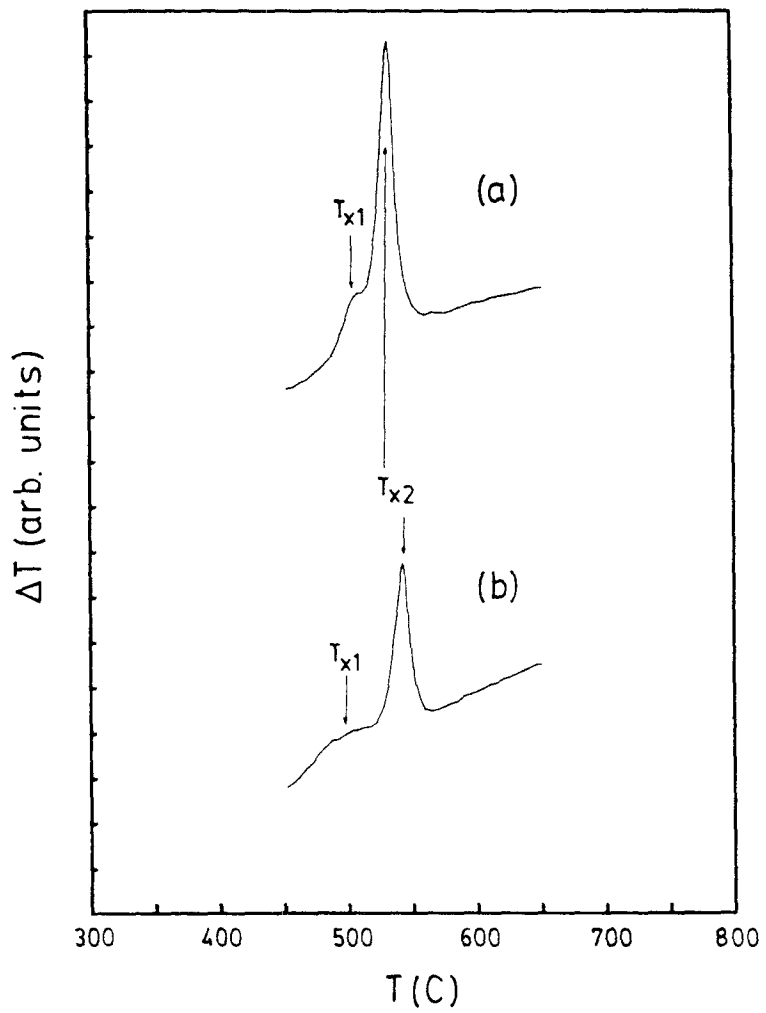

Figure 4.18 Differential thermal analysis data for two rhodium based metallic glasses, obtained by using a heating rate of 10 C/min. (a) $Rh_{70}Si_8B_{22}$, (b) $Rh_{60}Si_8B_{32}$.

§ 4.2.3 Conclusions

From the results of the diffraction experiments on the $(Ru_{0.14}Zr_{0.16})_{100-x}B_x$ and the $Rh_{92-x}Si_8B_x$ alloy series, it is apparent that these alloys exhibit rather unusual short range order (SRO). Indications are that a packing of trigonal prisms can be envisaged to explain the observed atomic distribution functions.

Studies on other high metalloid glasses have also been carried out by Cowlam and co-workers[31,67] and by Inoue et al.[68]. The former performed detailed neutron diffraction studies[31] on the alloy $Ni_{64}B_{36}$. They too observed the "unusual" second peak splitting. By using isotopic substitution techniques they were able to resolve the pair correlation functions, and found the existence of a peak at 1.7 to 1.8 Å in the B-B correlation function. The area under this peak gave a coordination number of 1.1. Based on the distance at which this peak occurs (very close to the Goldschmidt diameter for boron), and on the low coordination number, Cowlam et al. interpreted it as a result of B-B nearest neighbours. This is the first positive evidence for the occurrence of metalloid-metalloid nearest neighbours in a TM-M glass. They, however, believe that the boron atoms, rather than occupying interstitial sites, actually substitute nickel atoms. With this interpretation, though, one would expect a much higher B-B coordination as is found in substitutional ETM-LTM glasses.

In view of this, it appears that the proposal of a TP packing to explain the structures of Rh-Si-B and Ru-Zr-B glasses is a reasonable one. The prediction that such a packing would mean a certain amount of B-B nearest neighbours is not entirely unrealistic, especially since this has been observed in other glasses.

The gradual occurrence of the structural transition in Rh-Si-B glasses from a DRP type glass to something different is remarkable. Not an abrupt transition, but rather an increasing preponderance of trigonal prisms is probably responsible for this change. With increasing TP packing, the features of a DRP structure are replaced by the signature of the prismatic coordination.

Another point worthy of mention is the success of trigonal prismatic models for TM-M glasses with low metalloid content. Both Gaskell's simulation of $Pd_{80}Si_{20}$ glasses using the Fe_3C edge sharing scheme (figure 4.5), and the simulation of Fe-B glasses by Kobayashi et al.[74] using the randomly arranged trigonal prisms were very successful. This indicates a certain versatility about such a coordination, a feature that is absent to an extent in the DRP models.

§ 4.3 THE COMPARATIVE STUDY

The relationship between amorphous structures produced by rapidly quenching the melt and those produced by the condensation of the vapour phase have been a subject of considerable interest but little study[87-90]. The relationship between the liquid phase and the glass is direct. To some extent the short range order of the liquid is preserved in the glass, possibly to a larger extent at eutectic compositions[11]. Vapour deposition, on the other hand, allows for atomic arrangements that are not related to the liquid structure. The motion of an atom on the surface of the film depends on Q_d[eV], the activation energy for surface diffusion, T[K], the temperature of the substrate, a[Å] the atomic jump distance and R[Å/sec] the deposition

rate. The distance of travel, d[Å], in a given time, t[sec], may be expressed as

$$d(t) = (2tD_s)^{1/2} \quad ,$$

with (4.11)

$$D_s = a^2 \nu \exp[-Q_d/k_B T] \quad .$$

ν is of the order of the Debye frequency and k_B is Boltzmann's constant. Depending on the value of Q_d, for a deposition at a given temperature, it is possible to produce amorphous structures which have larger trapped free volume and greater inhomogeneity and density fluctuations than the corresponding liquid quenched structures. It is also possible, for a suitable value of Q_d, to obtain amorphous structures that are more relaxed and have a lower free energy than their liquid quenched counterparts. In either case, the two structures are expected to be different, and it is possible that this difference would also affect any physical properties of interest. Under certain vapour deposition conditions it is also possible to retain some entrapped gaseous impurities in the films. This could also lead to further differences in the two amorphous structures.

A more fundamental question regarding the structure of amorphous materials arises out of this discussion, namely, what is the structure of an "ideal" glass ? This "ideal" state could then be considered as a reference state, much in the same way a perfect crystal is a reference state for crystalline materials. It would also permit a quantitative comparison between different glasses in terms of a parameter (or set of parameters) that would have a known value for the "ideal" state.

The entropy difference, ΔS_{con}, between the liquid and equilibrium crystalline phases decreases with decreasing temperature. That is to say, the liquid becomes increasingly configurationally ordered. At T_g, the glass transition temperature, this configuration is frozen, and the equilibrium state is no longer experimentally accessible (at least on a practical time scale). Information about the equilibrium structure in this temperature regime must be obtained by extrapolation. Kauzmann[91] pointed out that ΔS_{con} seemed to vanish at some finite temperature T_o. In any case, the configurational energy of the equilibrium amorphous phase must vanish at 0 K due to thermodynamic considerations.

What, then, is the "ideal" (that is, fully ordered - no configurational entropy) amorphous state ? Based on microcrystalline models for the liquid state, that have since been disproven, Kauzmann[91] postulated that at T_o the system must undergo "spinodal decomposition," the implication being that full configurational order could be obtained only through translational symmetry. Based on our present knowledge of the well-defined short range order (SRO) in the amorphous state, we must rephrase the question regarding the change around T_o in a different, more plausible way : "Is it possible to construct a fully ordered ($\Delta S_{con}=0$), infinite, amorphous (no translational symmetry) structure ?"

If ΔS_{con} is to be the parameter that characterises the amorphous state, then models must be built to conceptually approach a structure with $\Delta S_{con} = 0$, and such models must contain the basic topological and chemical SRO known to exist in amorphous materials. For example, the random packing in pure amorphous metals[39], or the tetrahedral

coordination in amorphous silicon or germanium[42], or the absence of metalloid-metalloid nearest-neighbours in archetypal TM-M glasses[45] should be incorporated.

There has been some success along these lines. The entropy of fusion of a metallic system is typically on the order of k_B per atom, most of which is the configurational entropy. Spaepen[92] has shown that in tetrahedrally coordinated full-scale random networks, ΔS_{con} is much lower, on the order of 0.2 k_B. In the case of amorphous hard sphere packings, large fully ordered clusters have been generated by Hoare et al.[93,94] and shown to have configurational entropies, ΔS_{con} on the order of $10^{-2} k_B$.

As already mentioned, this "ideal" state cannot be realised experimentally. However, it appears that upon comparing the nature of the amorphous phases produced in the same material, it is possible to learn something about the nature of the amorphous state. One route, which is often taken, is to compare the as-quenched and relaxed states of a glass[95]. This relaxation is achieved by low temperature anneals that permit atomic rearrangement without destroying the amorphous structure. The other possible route is to compare the amorphous structures formed by the same alloy using different preparation techniques. In conjunction with annealing studies, it is expected that such a study would be very valuable.

As such, a comparison of liquid quenched and sputtered materials was undertaken. Also studied were the effects of changing the sputtering condition. For instance, films sputtered under 5 μm argon pressure were found to be quite different from films sputtered under 50 to 75 μm argon pressure. While it was not possible to study all the

properties of the films deposited under high pressure due to their extreme brittleness, their superconducting properties were studied, and are discussed in § 4.3.3.

§ 4.3.1 Macroscopic Properties

The alloy chosen for this comparison was $(Mo_{0.6}Ru_{0.4})_{82}B_{18}$. The motivation for this choice was the extensive work already done on metallic glasses of this composition[15] and the interesting physical properties that this alloy was known to exhibit[a]. $(Mo_{0.6}Ru_{0.4})_{82}B_{18}$ has a crystallisation temperature close to 800 C and this alone made it an interesting candidate.

X-ray diffraction showed these films to be amorphous, exhibiting the expected broad maxima typical of amorphous materials. The detailed diffraction study is reported in § 4.3.2.

The macroscopic properties of the sputtered $(Mo_{0.6}Ru_{0.4})_{82}B_{18}$ films were quite similar to those of the splat quenched foils. (Hereafter, "films" refers to the sputtered material, while "foils" refers to the liquid-quenched alloys.) These were the crystallisation temperature, T_x, and the room temperature resistivity, ρ_{RT}. Table 4.5 lists these values for the two morphologies.

This agreement was encouraging and suggested that the amorphous structure in the two morphologies might be very similar.

---

[a] This work was done in collaboration with the Thin-Films Lab. at JPL. Their main interest was to study an amorphous alloy that could be used as a protective coating in abrasive and corrosive environments.

Table 4.5

A comparison of the macroscopic properties of the two morphologies.

MORPHOLOGY	T (C) ± 1 %	(ohm-cm) ± 5 %
FILMS	800	155
FOILS	785	150

§ 4.3.2 Atomic Structure

Detailed X-ray diffraction studies of the films sputtered under low argon pressures (5 μm) were carried out as described in § 3.3 and the data were analysed as explained in § 4.1.

Figure 4.19 shows the reduced interference functions, I(K), for both the films and the foils of $(Mo_{0.6}Ru_{0.4})_{82}B_{18}$. These patterns are representative of archetypal TM-M glasses, in that the second peak is much less intense than the first and has a high angle shoulder. In fact, Williams et al.[96] have shown that the structure of the similar $(W_{0.5}Ru_{0.5})_{80}B_{20}$ glasses fits the Bernal-Finney DRP model[41] particularly well.

Figure 4.20 shows the reduced radial distribution functions for the two morphologies. Again, these exhibit all the features expected in a TM-M metallic glass.

Table 4.6 lists the interesting parameters obtained from figures 4.19 and 4.20.

The first peak position in I(K) for the films is found to be at a considerably lower value of K than the corresponding peak position for

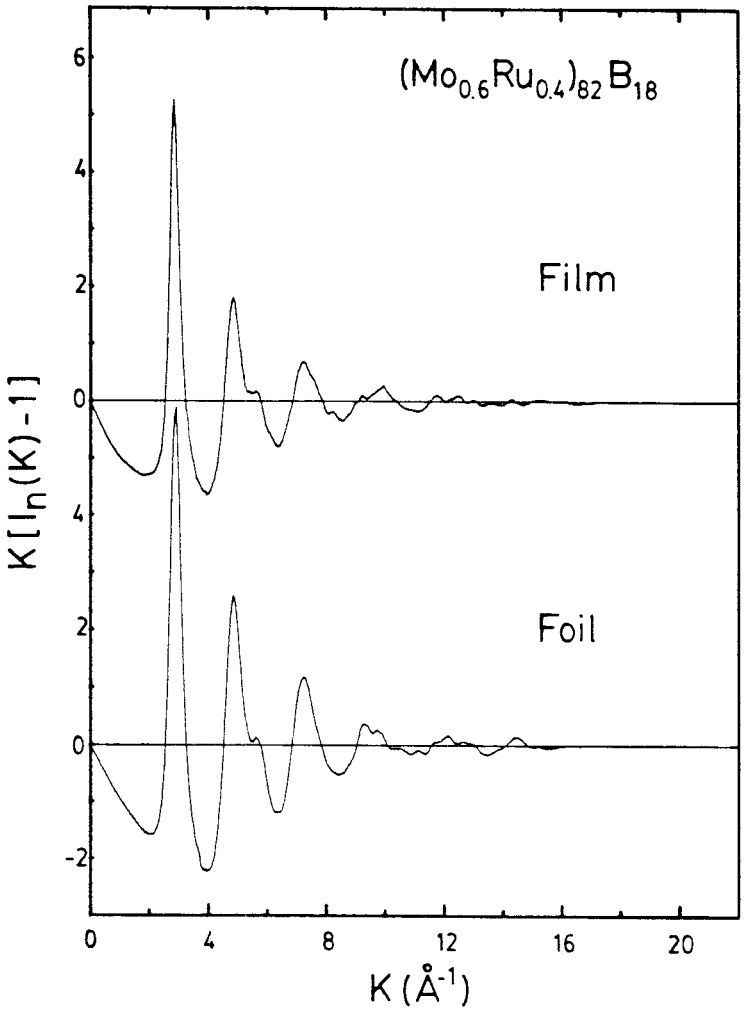

Figure 4.19 Reduced interference functions, I(K) = K[I(K)-1], for the sputtered films and liquid quenched foils of $(Mo_{0.6}Ru_{0.4})_{82}B_{18}$.

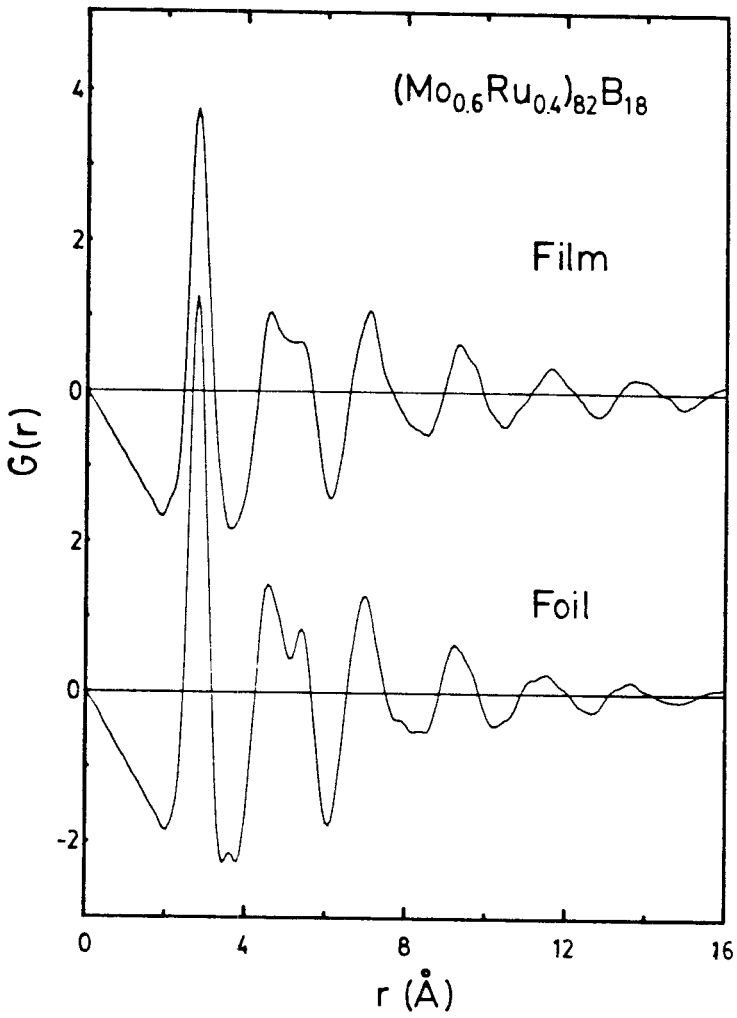

Figure 4.20 Reduced radial distribution functions, G(r), for the sputtered films and liquid quenched foils of $(Mo_{0.6}Ru_{0.4})_{82}B_{18}$.

Table 4.6

Parameters of interest for the films sputtered under 5 μm of argon and the rapidly quenched foils as obtained from the diffraction studies. K_i are the peak positions in the reduced interference functions, I(K), R_i are the peak positions in the G(r), CN is the total coordination number obtained and ρ is the measured atomic density.

SAMPLE	K_1 (Å^{-1}) ± 0.01	K_2 (Å^{-1}) ± 0.01
FILMS	2.89	4.86
FOILS	2.84	4.85

SAMPLE	R_1 (Å) ± 0.01	R_2/R_1	R_2^{sh}/R_1	R_3/R_1	CN ± 0.5	ρ (atoms/Å^3) ± 0.1 %
FILMS	2.77	1.65	1.92	2.51	13.22	0.0745
FOILS	2.77	1.66	1.93	2.54	13.30	0.0716

the foils ($\Delta K = 0.05$ $\mathring{A}^{-1}$). A simplistic interpretation according to the formula[97]

$$R_1 = \frac{1.23\ (2\pi)}{K_1} \tag{4.12}$$

would suggest that the first nearest-neighbour distance in the films is ~ 0.05 $\mathring{A}$ larger than in the foils. However, on examining the G(r) shown in figure 4.20, we note that R_1 is the same in both the films and the foils. This is because when carrying out the Fourier transform there are contributions to the position and shape of the first peak from all values of the scattering vector. This information is discarded by the expression in equation (4.12). Nonetheless, the differences in K_1 indicate that there are some differences in the two structures.

We also note that the shoulder in the second peak is considerably better defined in the case of the foils. This is an indication of a better defined SRO in the foils than in the films. Further, while the positions of the first peaks (R_1) for both the morphologies coincide, the positions of the second and third peaks are at higher values in the films. This would indicate that there is some excess strain in the film that leads to noticeable separation for the second and third nearest-neighbours.

A vapour deposition process such as sputtering is a high energy process achieving much higher effective "quench rates" (§1.2.1) as compared to those attained upon quenching a melt. It is expected, therefore, that the sputter deposited films would have a much higher density of frozen-in stresses and strains, and a significantly reduced SRO than the foils. In the words of § 4.3, the configurational

entropy, ΔS_{con}, would be much higher in the amorphous films. Also, any argon that might be incorporated into the films during the deposition would cause an increase in the excess free volume and local strains. This would further result in the increase in the average distance between metal atoms. This entrapped argon is likely to desorb during post-deposition annealing, resulting in stress release and atomic rearrangements.

The density measurements also suggest the presence of excess free volume in the films as compared to the foils. While the as-sputtered films had an atomic density that is $\sim$4 % less than that of the foils (table 4.6), annealing the films at 450 C for 2 hr increased their density to 0.0732 atoms/$\mathring{A}^3$. This is still $\sim$1.7 % less than the density of the foils, but the fact that annealing results in a densification of the films indicates that there are microvoids that partly disappear by reaching the film surface and perhaps partly agglomerate into large voids and cracks.

The annealing left the films too brittle to permit a detailed diffraction study.

§ 4.3.3 Superconducting Studies

Superconducting properties of materials are known to reflect their structure[98-100]. This is true for amorphous alloys as well. Clemens[100] has shown that the flux pinning profiles in amorphous materials can be a very sensitive probe to the inhomogeneities present. In an attempt to supplement the results from the diffraction studies on the sputtered films, the measurement of key superconducting properties was undertaken. The properties measured included T_c, the transition

temperature, H_{c2}, the upper critical field and dH_{c2}/dT, the critical field gradient. These properties were studied for the as prepared materials and for selected anneals. There was also an attempt to study them as a function of the sputtering pressure.

Table 4.7 summarises the results obtained for T_c and H_{c2}. The films sputtered under 5 μm argon pressure had a T_c of 6.19 K which was higher than the T_c of 6.05 K reported for the foils[15]. After annealing at 500 C for 20 hr the T_c of the films lowered to 6.3 K, closer to that of the liquid quenched materials. The films sputtered under 75 μm argon were intended to emphasise the effects of any adsorbed argon. It was found that these films have an as-deposited T_c of 3.18 K. This value was considerably lower than that for the films. Upon annealing, however, the T_c was seen to increase to 5.12 K.

A decrease in T_c of about 6 % has been reported for the liquid quenched foils for similar anneals (500 C, 20 hr), and it has been attributed to the annealing out of defects, strains and excess free volume[101]. It is conceivable that a similar mechanism is in effect for the films sputtered under 5 μm argon. The larger percentage drop ($\sim$ 10%), however, would imply that the sputtered materials have a greater amount of such defects than the foils. This is consistent with the results of the diffraction studies.

Figure 4.21 shows the critical field curves for the sample deposited under low argon pressures. Upon annealing, the H_{c2} versus T curve shows an upward kink. This may be interpreted as evidence for a two-phase material, one having a lower T_c and a higher critical field gradient than the other. The behaviour reported for the foils did not permit this interpretation as conclusively[100]. While there was a

Table 4.7

A list of the superconducting parameters, T_c, H_{c2} and ΔH_{c2} for the two kinds of films, as-deposited and after the strongest anneal. Also shown for comparison are the values for the as-quenched foil.

MATERIAL AND TREATMENT	T_c (K)	H_{c2} (kG/K)	ΔH_{c2} (kG)
Film sputtered under 5 μm argon. As deposited.	6.91	24.7	6.5
Film sputtered under 5 μm argon. Annealed at 500 C for 20 hr.	6.3	25.8	7.4
Film sputtered under 75 μm argon. As deposited.	3.85	44.4	14.
Film sputtered under 75 μm argon. Annealed at 500 C for 20 hr.	5.12	70.3	46.
Foil. As-quenched.	6.05	24.5	5.2

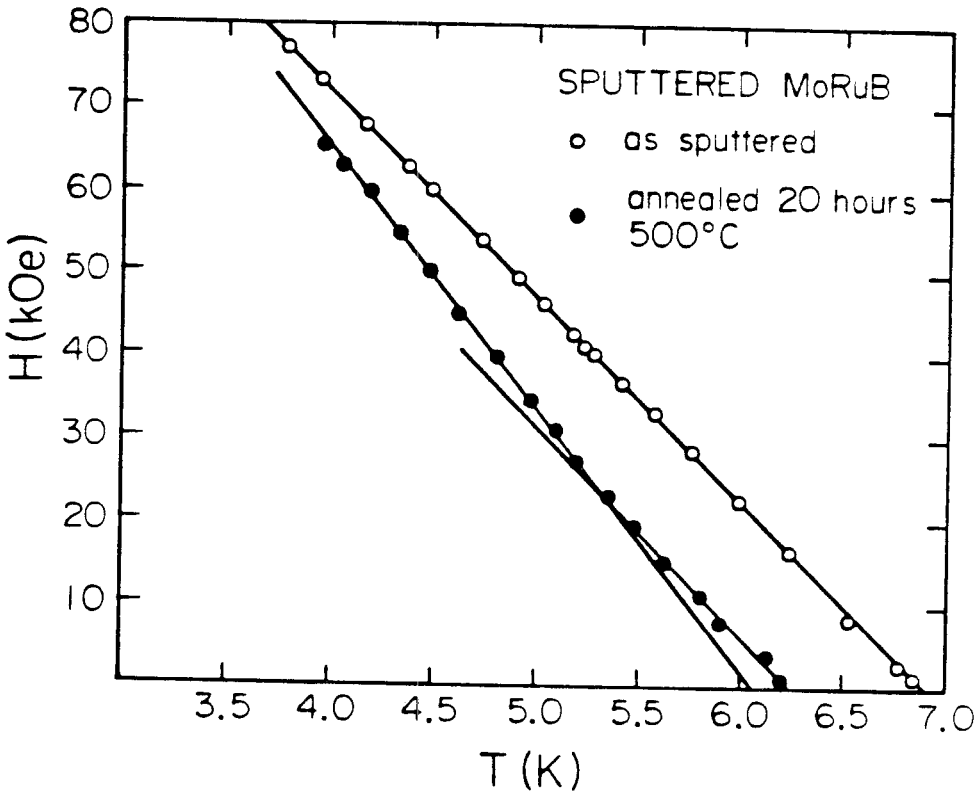

Figure 4.21 The critical field curves for the $(Mo_{0.6}Ru_{0.4})_{82}B_{18}$ films sputtered 5 μm argon pressure.

shift of the entire curve to lower temperatures, and while it did appear to deviate from linearity at lower values of H_{c2} than the as-quenched material, it was not possible to demarcate the two regions clearly.

So while the dH_{c2}/dT for the two as-prepared morphologies (the comparison, unless explicitly stated, is always intended between the foils and the low pressure "clean" films) was almost the same, the annealing behaviour was significantly different. The width of the transition, which is also indicative of the homogeneity of the material, was larger for the films. Further, it was seen to increase upon annealing. This is different from the results of other workers[102] where, upon annealing, the width was seen to decrease. Such a decrease was attributed to structural relaxation. Evidently, the introduction of the inhomogeneities, as indicated by the kink in the H_{c2} curves for the films, is reflected as this increase in the width of the transition.

The pinning profiles for these films were studied in collaboration with Clemens[103]. The films sputtered under low pressures exhibited very different profiles from films sputtered under high pressures.

Figure 4.22 shows the results for the "clean" films. The ordinate represents the normalised pinning force, F_p/H_{c2p}^2. H_{c2p} is the value of the critical field obtained by extrapolating the F_p versus H curve to zero. This value of the critical field is representative of the bulk of the sample, where the resistive measurement of H_{c2} only determines the field at which a supercurrent can no longer percolate through the medium. Since only 15 percent of a sample need be superconducting to permit percolation[104], H_{c2} is greater than H_{c2p} by an amount that

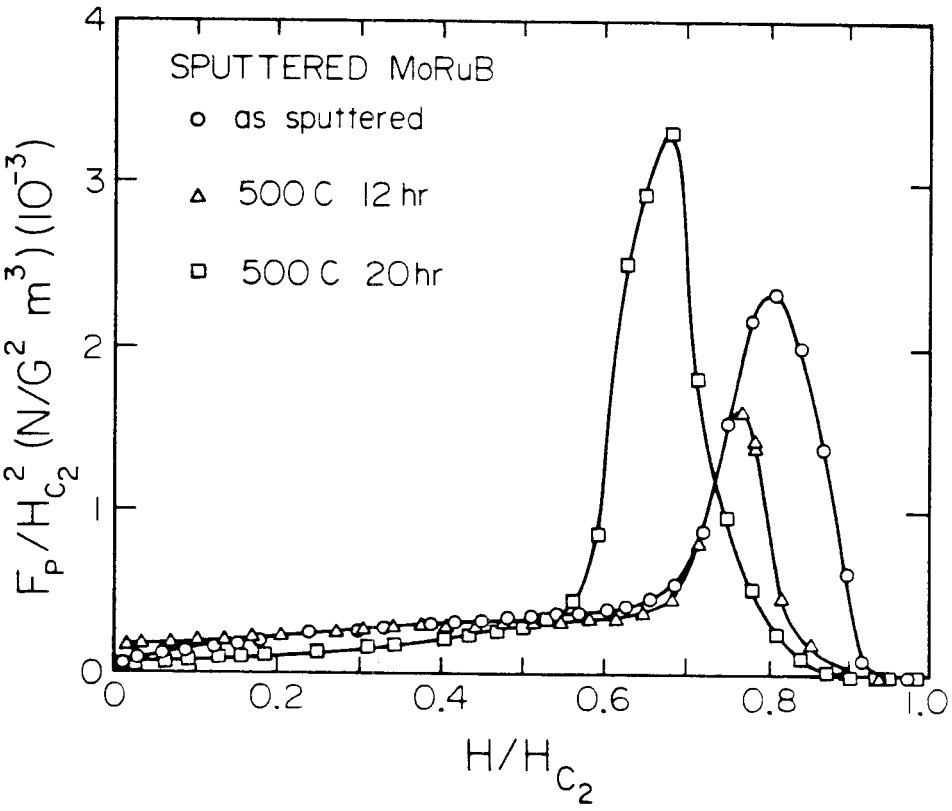

Figure 4.22 The normalised pinning force profiles for the film deposited under low argon pressure for three annealing conditions.

reflects the width of the distribution. Normalising the pinning force in this manner not only permits comparison between samples measured at different temperatures, but also eliminates the effects due to any changes in H_{c2} upon annealing. The abscissa in figure 4.22 is the reduced field, H/H_{c2}.

It is clear from figure 4.22 that, upon annealing, the flux pinning in the sample moves to lower reduced fields. This extrapolates to a low H_{c2p}, and the larger difference between H_{c2} and H_{c2p} implies larger inhomogeneity. Also, we note that the magnitude of the pinning force first decreases and then increases with annealing time. This is similar to the results on the foils[100], except that the pinning in the films is about fifteen times larger than that in the foils. These results again indicate the greater inhomogeneity in the films as compared to the foils. The annealing dependence of the magnitude of the pinning force indicates that there is an initial decrease followed by an increase in the inhomogeneity of these materials. The first stage may be akin to the annealing out of defects and strains as reported in the foils[101], while the second stage may mean phase separation within the amorphous phase. No growth of microcrystallites was observed by X-ray diffraction or TEM. It is quite interesting to note that Koch et al.[101] report the growth of inhomogeneities in $(Mo_{0.6}Ru_{0.4})_{82}B_{18}$ foils, as evidenced by small angle X-ray scattering at exactly these annealing conditions.

The T_c and H_{c2} values reported in table 4.7 for the films sputtered under high pressures of argon indicate unusually high critical field gradients. For the as-deposited film, these gradients extrapolate to an $H_{c2}(0)$ value of 171 kG. This extrapolation is just

linear, without the prefactor predicted by the Maki theory[105]. The empirical observation is that the Maki theory is not obeyed by amorphous materials[106]. Upon annealing the entire H_{c2} curve shifted to higher temperatures. No kink was observed in the curve even though the transitions were extremely broad. The gradient, however, was found to increase even further. If the annealed films persist in disobeying the "dirty" limit predictions for low reduced temperatures (T/T_c) and high reduced fields (H/H_{c2}), then the extrapolated fields $H_{c2}(0)$ would be around 360 kG. These fields are in the same region as predicted for materials like Nb_3Al and Nb_3Ge[107]. At the same time it is interesting to note the Nb_3Al and Nb_3Ge have considerably higher T_c than these films.

While it may be possible that these high critical fields are a result of the inhomogeneity, it is certain that this inhomogeneity is not crystalline. That extreme inhomogeneity exists is certain from the very broad transitions observed. If the material did contain microcrystallites of a phase with an intrinsically higher T_c and H_{c2} than the host amorphous phase, then for them to affect the properties of the matrix they would have to be greater than ξ_d, the coherence length in the material. Typically, ξ_d in amorphous materials is about 50 Å. If any significant fraction of microcrystalline inclusions of size greater than 50 Å existed in the films, they would have been detected by both X-ray diffraction and TEM. The films were found to be convincingly amorphous, both before and after the annealing.

Table 4.8 lists the coefficient of the electronic specific heat, γ[erg/cm^3-K^2], for the three morphologies, as obtained from[108]

$$\left(\frac{dH_{c2}}{dT}\right)_{T=T_c} = -4.48(10^4)\ \rho\gamma\ , \qquad (4.13)$$

where ρ[ohm-cm] is the normal state resistivity and $(dH_{c2}/dT)_{T = T_c}$ [G/K] is the critical field gradient at T_c. The bottom row in table 4.8 has been obtained by normalising out the effects of the density. Since the density of the films sputtered under 75 μm argon pressure was not available, the last column is left empty. The value for the foils reported by Hopkins et al.[109] was obtained from specific heat measurements. We note that γ for the films is less than that for the foils. For the "clean" films, after removing the effects of the lower density, the value obtained for γ is within 10 percent of that of the foil. This is about the extent of agreement that is expected between values calculated from equation (4.13) and those

Table 4.8

A list of the electrical resistivity and the coefficient of the electronic specific heat for the three morphologies.

	FOILS	FILMS (5 μm)	FILMS (75 μm)
ρ[ohm-cm]	$1.50(10^{-4})$	$1.55(10^{-4})$	$1.89(10^{-3})$
γ[mJ/cm^3-K^2]	$4.09(10^{-1})$	$3.55(10^{-1})$	$5.24(10^{-2})$
γ[mJ/mol-K^2]	2.98	3.3	-

obtained from specific heat measurements. The γ for the films prepared under 75 μm are much lower, and are probably the result of the high resistivity of the material. The reason for this unexpectedly high resistivity could be the presence of microcracks and voids in the films.

Hopkins et al.[109] have noted that in the $(Mo_{0.6}Ru_{0.4})_{1-x}B_x$ series γ appears to be constant at $\sim$4 mJ/mol-K^2 for $x < 0.16$ and falls to $\sim$2 mJ/mol-K^2 for $x > 0.20$. They interpret this as a reflection of two different short range orders (SRO), one on either side of $x = 0.18$. They, however, refrain from suggesting the exact nature of this short range order, or its variation. If the lower value for γ in the films is significant, it would mean that the alloys with $x > 0.20$ have an SRO similar to the films, that is a less dense structure, with a larger nearest-neighbour distance.

§ 4.3.4 Conclusions

The results from both the diffraction studies and the superconductivity work show conclusively that the films prepared by sputtering, even under nominally clean conditions contain a denser distribution of quenched-in strains and defects. This is not unexpected in view of the atomistic nature of the preparation technique.

It appears that these defects can be easily annealed out, even to the extent of a densification of the matrix.

While these microvoids do not play a determinant role in the "clean" films where the macroscopic properties such as the crystallisation temperature and the room temperature resistivity are concerned, microscopic properties such as the superconducting

transition temperatures and the critical field gradients are significantly altered.

In the extreme case where there is surely some incorporation of argon into the films, the superconducting properties behave quite dramatically. The extremely high critical field gradients and broad transitions indicate a considerable amount of inhomogeneity in these films.

Figure 4.23 shows the cross sections of a film deposited under 5 μm argon and one under 75 μm argon. Even in the as-deposited state there is a clear difference. Under high deposition pressures the film tends to grow in a columnar fashion, and it is this growth pattern itself that may be responsible for the unusual low temperature properties.

The films thus appear to be metastable structures that tend to relax towards the liquid quenched material for short duration anneals, but probably due to their less dense structure tend to separate easily into two different amorphous phases, for longer anneals.

Admittedly, this single study does not permit a universal conclusion regarding the effects of the preparation technique on the amorphous state of all materials. It does, however, imply that, before the properties of metallic glasses may be attributed to amorphous sputtered films of the same composition, there is need for independent confirmation. The sputtered films are likely to be materials with greater disorder and inhomogeneity than the liquid quenched materials.

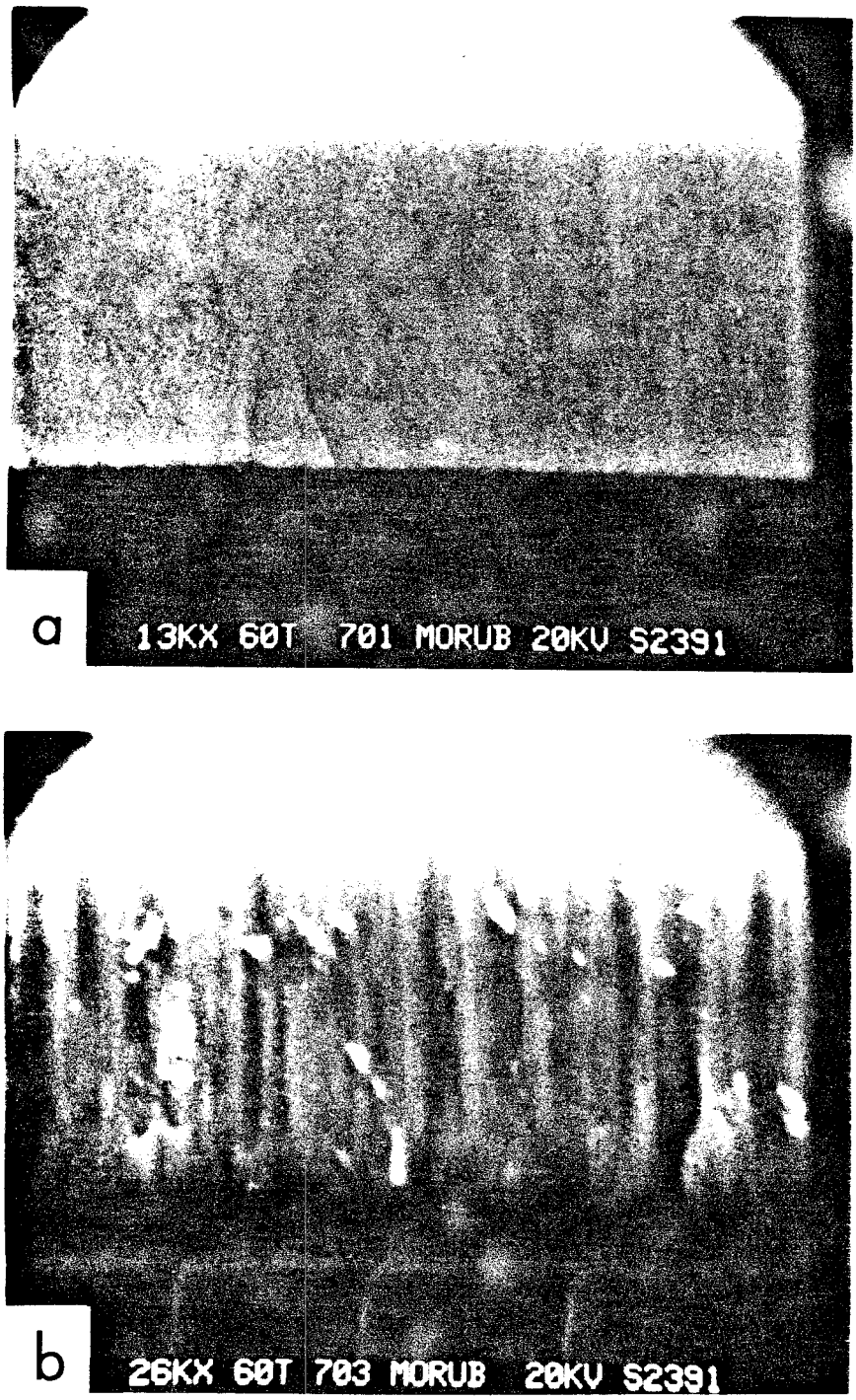

Figure 4.23 The cross section, as observed under the scanning electron microscope of (a) the film deposited under 5 μm argon and (b) that deposited under 75 μm argon.

§ 4.4 PROPOSED EXPERIMENTS

In the opinion of the author, the study of the structure of amorphous materials is at a crossroad. While it is possible to fine tune models for specific alloy systems, and propose new models that would replace existing ones, some new experiments are necessary to help elucidate the state of affairs.

One such experiment is an isotope substitution experiment using neutron scattering. Some isotopes, such as Ni^{62} and Dy have negative scattering lengths, b. It is therefore possible to make an alloy in which the average scattering length for one of the elements is zero. For instance, a Ni-B alloy, with $< b >$ for nickel tuned to zero, would show only the B-B correlatioms. When using other techniques, such as isomorphous substitution, it is this B-B correlation that is the hardest to obtain. The reason for this is the small percentage fraction that this correlation contributes to the total distribution function. As a result, even the best experimental data are not good enough to provide defininitive results[53]. For a Ni-B alloy in which $< b >_{Ni}$ is zero, only the experimental statistics would restrict the accuracy in the B-B correlation obtained. This result could then be used to solve for the other correlations by carrying out an identical experiment on an alloy of the same composition made using natural nickel. It would therefore be interesting to study alloys of Ni-B at low boron concentrations, where they represent archetypal TM-M glasses and at high boron concentrations where the deviations from DRP models are pronounced. The coordination numbers obtained would help determine whether the boron sites are interstitial or substitutional in the high metalloid regimes. Attempts have been made at such studies on low

concentration Ni-B alloys by Lamparter et al.[110] but they were not able to produce alloys with $< b >_{Ni} = 0$. Also interesting would be to study the corresponding liquid alloys. At high boron concentrations there may be a preferred SRO in the liquid.

The second experiment that can be of considerable interest is to study the dynamical structure factor $S(q,\omega)$ for these alloys using inelastic neutron scattering. $S(q,\omega)$ would reflect not only the momentum transfer information but also the energy transfer associated with interatomic motions. In a TM-M glass, for instance, the motions of the lighter metalloid atom would contribute to the total vibration spectra of the glass. If the metalloid site differs substantially in two different glasses, then $S(q,\omega)$ should be able to distinguish between the two glasses and provide information about the local coordination around the metalloid atom. Such information is usually averaged out in radial distribution functions. While quite a few calculations have been made for simple metal metallic glasses such as Mg-Zn[111], not much work has been done on TM-M glasses. Some preliminary results[112] from calculations on high metalloid glasses have shown that there should be a significant contribution to the vibrational density of states associated with the boron atoms in the centre of the trigonal prisms. Due to the large mass ratios typical in TM-M glasses one or more of these modes appear to be localised at the high energy regions of the spectrum and should be observable experimentally.

CHAPTER 5

APPLICATIONS

§ 5.1 WEAR STUDY

As was mentioned in a footnote in § 4.3.1, some of the emphasis of the study on thin films was application-oriented. Could the advantages of sputtering be combined with the exciting physical properties of amorphous alloys ? In order to answer this question, an investigation of the corrosion and wear resistance of amorphous films coated on various steel substrates was undertaken. In this chapter the results of the wear studies are reported.

The alloy selected for this study was $(W_{0.6}Re_{0.4})_{76}B_{24}$. The considerations that went into this choice were as follows. Since local temperatures in wear processes are likely to be very high, the material selected should have a very high crystallisation temperature.

Johnson et al.[15] have noted that the solid solubility of metalloids in refractory metal sigma phases are very low, leading to good glass forming abilities. The metalloid content that result in best glass formation ranges between 14 and 28 atomic percent depending on the particular alloy system. The W-Re system is known to form a sigma phase that is stable up to $\sim$2800 C. Further, tungsten-based alloys are known to be hard. This is an important consideration since wear in most materials is known to scale with hardness. The alloy $(W_{0.6}Re_{0.4})_{76}B_{24}$ satisfied all these criteria and was therefore selected for study as a wear coating.

§ 5.1.1 Sample Preparation

Films of amorphous metallic $(W_{0.6}Re_{0.4})_{76}B_{24}$, typically 3 to 5 μm thick, were deposited on glass, quartz and 52100 steel substrates using d.c. S-gun magnetron sputtering. The target of $(W_{0.6}Re_{0.4})_{76}B_{24}$ used in sputtering was prepared as discussed in § 3.1. Substrates were mounted about 8 cm away from the target. Argon was used as the carrier gas for sputtering. The typical rate of deposition was 300 Å/min. Compositional uniformity over the surface and along the thickness of the films was studied using secondary ion mass spectrometry (SIMS). Film thickness as well as depth of the craters created during the SIMS studies were measured for calibration purposes using a surface profilometer. The films deposited on glass and quartz substrates were utilized for structural characterisation by X-ray diffraction and the determination of the crystallization temperature (T_x). X-ray diffraction studies were performed on a Norelco "Theta - two theta" diffractometer using CuKα radiation. Electrical resistivity as a function of temperature was measured to obtain T_x. This was done using a four-point probe with the sample enclosed in a temperature controlled argon atmosphere.

The substrates used for the wear test were heat-treated 52100 bearing steel discs and pins. Both, the disc (2.5" in diameter, 0.25" thick) and the pin (0.75" in diameter and spherical tip) were annealed at 750 C for one hour and then quenched in water. They were then tempered at 300 C for forty minutes resulting in a hardness of 55 ± 3 R_C (Rockwell hardness on C scale). These heat-treated pins and discs were then polished to better than a root mean square roughness of 1000 Å and used as substrates.

§ 5.1.2 The Experiment

To optimize the wear characteristics of the coated surfaces with respect to those of the uncoated pin and disc, effects of the following sputtering parameters on the wear behaviour were systematically studied : argon pressure, substrate temperature, substrate bias during sputtering, sputter cleaning/etching prior to the actual deposition, and the rate of deposition.

Wear measurements were carried out at room temperature, under atmospheric conditions, using the pin-on-disc method shown in figure 5.1. The pin-on-disc technique was selected for two reasons; it is sensitive under low load (<1 kg) conditions, and the volume loss from the pin, a direct measure of the wear, can be conveniently obtained from the diameter of the wear pattern. The sliding speed of the pin on disc was maintained constant ($\sim$1 ft/sec) by adjusting the disc rpm, and the wear pattern as well as the volume loss of material from the pin was studied as a function of the load. A maximum load of 1 kg was used. The volume removed was calculated by measuring the mean diameter of the wear spot on the spherical surface of the pin and using the relation

$$V = R^3 \left[(2/3) - \cos\phi + (1/3) \cos^3\phi \right],$$

where R is the radius of the pin and ϕ is the half-angle subtended by the wear pattern at the centre of the pin.

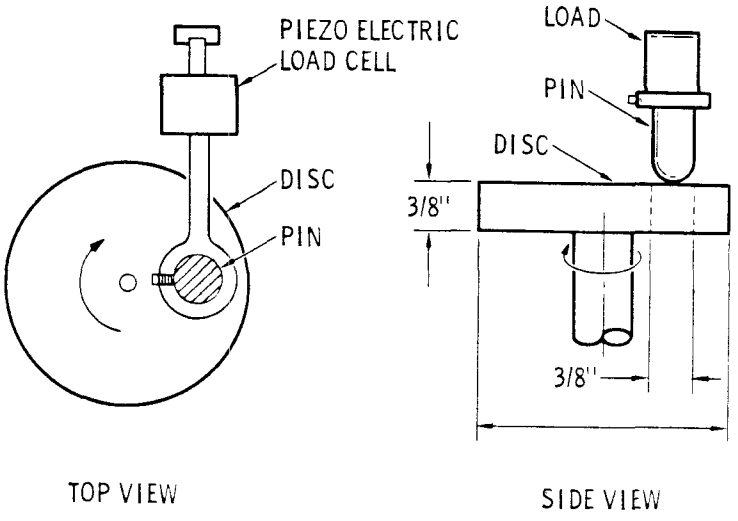

Figure 5.1 Schematic diagram of the experimental setup for the "pin and disc" method of wear rate measurement.

§ 5.1.3 Results and Discussion

Figure 5.2 shows an X-ray diffraction pattern from an as-deposited 5.2 μm thick $(W_{0.6}Re_{0.4})_{76}B_{24}$ film on glass using CuKα radiation. The broad diffraction band and absence of any sharp lines in the pattern indicate an amorphous material. A typical composition depth profile by SIMS of an as-deposited $(W_{0.6}Re_{0.4})_{76}B_{24}$ film is shown in figure 5.3. Uniformity of the composition throughout the film thickness (∿0.8 μm) is remarkable. The drop in the profiles at 0.8 μm is due to the film-substrate interface. It must be mentioned, however, that several initial deposition runs from the new target showed significant composition variations along the film thickness presumably due to the differences in sputtering yields of the constituents. Only after long conditioning of the target (corresponding to almost 1 mm erosion of the target surface), did the film composition stabilise and show reproducibility from run to run. In every run, however, the target was routinely pre-sputtered onto a mechanical shutter for several minutes before exposing the substrates to the vapour flux. Also, the amorphous nature and composition uniformity of the films were closely monitored during the entire course of work, especially whenever sputtering conditions were changed. No significant changes in these characteristics were observed.

The temperature dependence of the normalized electrical resistance of a film deposited on a quartz substrate is shown in figure 5.4. The large sudden and irreversible change in the film resistance at about 1275 K corresponds to the crystallisation of the film.

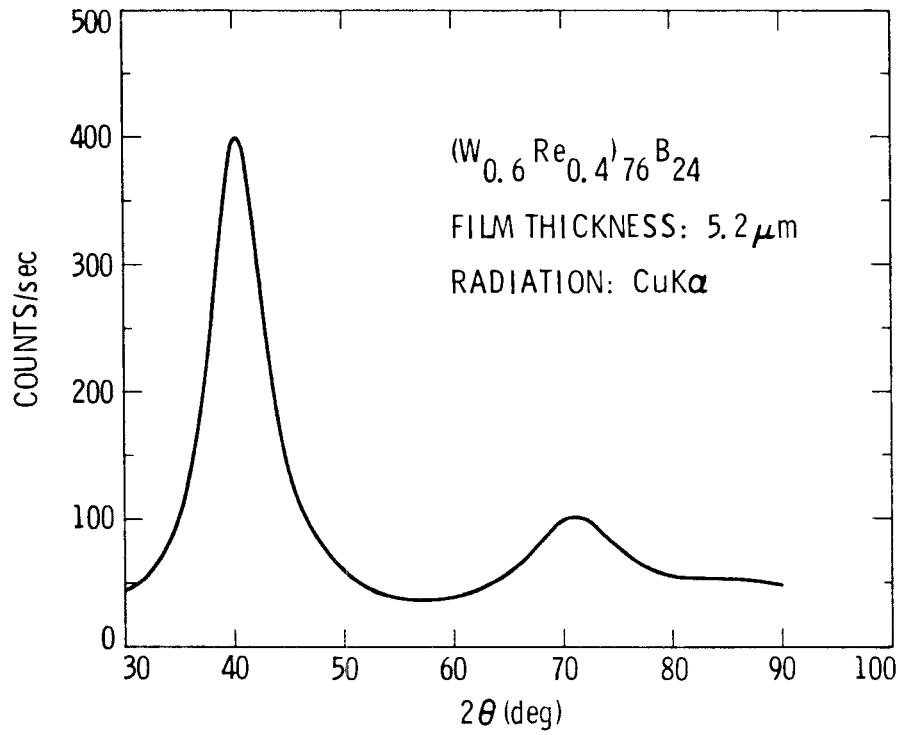

Figure 5.2 An X-ray diffraction pattern of a 5.2 μm thick film of $(W_{0.6}Re_{0.4})_{76}B_{24}$ obtained using CuKα radiation.

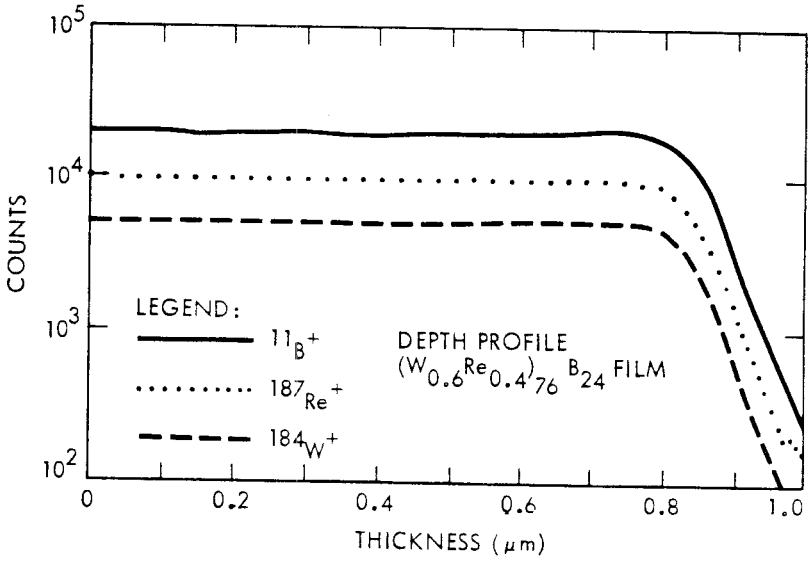

Figure 5.3 A chemical composition-depth profile of a $(W_{0.6}Re_{0.4})_{76}B_{24}$ film on a glass substrate, obtained using SIMS.

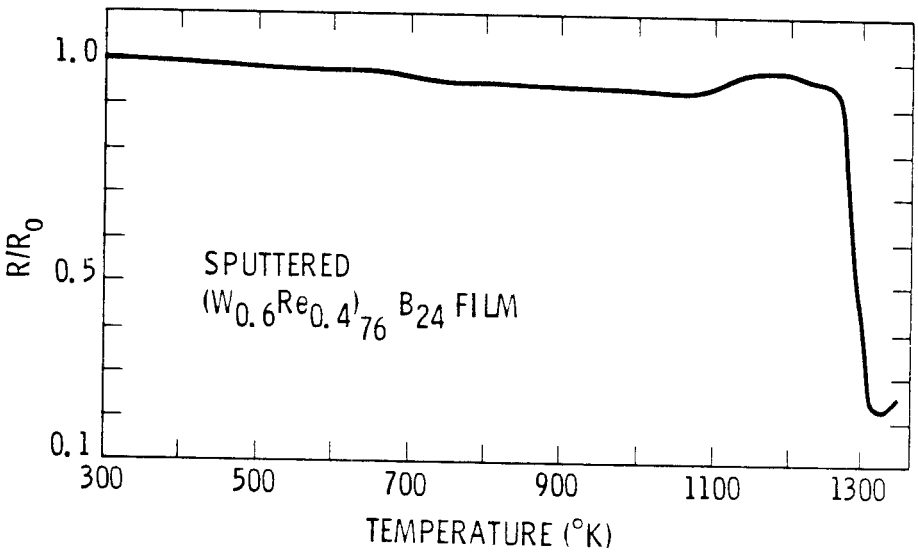

Figure 5.4 The temperature dependence of the normalised resistivity of a $(W_{0.6}Re_{0.4})_{76}B_{24}$ film. The sharp drop in the resistivity at 1275 K corresponds to the crystallisation of the film.

Figure 5.5 shows the load dependence of microhardness of an as-deposited, 5.2 μm thick $(W_{0.6}Re_{0.4})_{76}B_{24}$ film on 52100 steel substrate. Only under low load conditions (below ∿100 ponds) were the indentations on the sample less than 25 % of the film-thickness. The hardness of the films was therefore 2400 Kg/mm^2. The observed hardness of the film-substrate composite at higher load values drops significantly (due to lower hardness of the steel substrate) as shown in the figure.

A sequence of depositions on 52100 steel disc and pin surfaces and measurements of their wear characteristics was carried out under various sputtering conditions. The changes in the deposition parameters were dictated by their influences on apparent film adhesion, hardness and wear behaviour.

The resulting set of optimum deposition conditions is presented in table 5.1. A brief discussion of the influence of some of the more determinant conditions is presented below.

The carrier gas pressure was varied to optimize between the formation of a weak structure with vertical columns, as a result of the use of high sputtering pressure, and excessive compressive stresses in the film, resulting from too low a pressure[113]. Films deposited under pressures of less than 8 μm of argon exhibited blistering when exposed to the atmosphere, indicating a large density of frozen-in compressive stresses. On the other hand, at pressures of 15 μm or above, stresses appeared to be tensile in nature, causing adhesion failure through development of numerous microcracks in the films. The most stable and adherent film on steel was obtained at 10 μm pressure of argon.

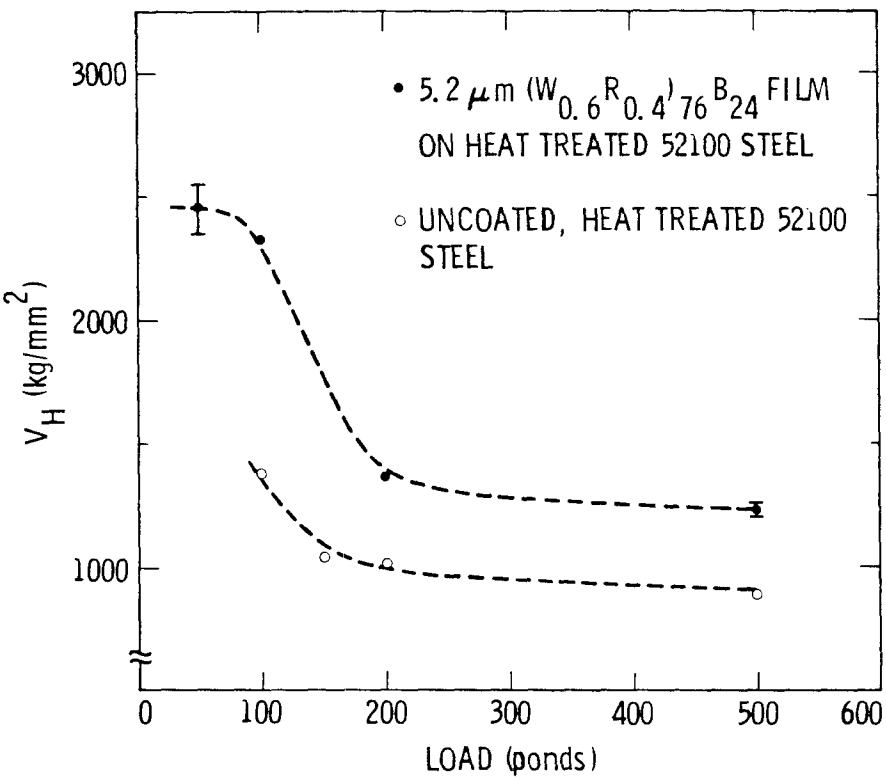

Figure 5.5 The load dependence of the Vicker's hardness of a 5.2 μm thick coating of $(W_{0.6}Re_{0.4})_{76}B_{24}$ on heat treated 52100 steel. The hardness of the uncoated surface is shown for comparison.

Table 5.1

The optimum conditions for the sputter-deposition of wear resistant $(W_{0.6}Re_{0.4})_{76}B_{24}$ coatings on 52100 bearing steel.

A. <u>Sputter-etching prior to the deposition</u>:	
Substrate bias	-500 V d.c.
Current density	20 mA/cm^2
Argon Pressure	50 μm
Time	15 min
B. <u>Deposition</u>:	
Substrate temperature	350 C
Argon pressure	10 μm
Target to substrate distance	8 cm
Deposition rate	300 Å/min

Although the film adhesion on the steel surface was not independently evaluated, occasional flaking or peeling of the films during the measurement of wear clearly distinguished the sputtering conditions which resulted in better adhesion. Significant improvement in adhesion was observed when the steel surface was subjected to a light sputter-etch just prior to the deposition. This was accomplished by maintaining the substrates at a -500 V d.c. bias with respect to the chamber under a 50 μm pressure of argon for 15 min. The slight surface roughness thus created is believed to be effective in strengthening the interface. The substrate bias was maintained during the initial few minutes of the actual film deposition. The intent was to use the Ar^+ ion bombardment of the substrates and the resulting partial sputter etching during the film growth to help relax the first few monolayers deposited. This was expected to reduce the stresses caused due to the incoherent nature of the interface.

To study the effects of a simultaneous application of negative bias and heat to the substrates during film growth, wear characteristics were monitored as a function of deposition temperature which was varied from 25 C to 450 C. This was achieved by controlling the power fed into a quartz halogen-radiation heater in the sputtering chamber facing the substrates. Wear resistance improved gradually with temperature; however, the effective deposition rate dropped significantly above 400 C, indicating a drastic reduction in the sticking coefficients at high temperature. Best results were obtained at 350 C as listed in table 5.1. This temperature is considerably less than that used in alternate techniques. For instance, the formation of TiN coatings by multi-arc deposition raises the

temperatures of the substrates to as much as 800 C.

Figure 5.6 summarises the wear results. Wear rate versus load is plotted for the coated and uncoated steels. It is clear from the figure that coating the 52100 bearing steel with a film of $(W_{0.6}Re_{0.4})_{76}B_{24}$ reduces the wear rate by 2.5 to 3 orders of magnitude. For the ranges of loads used, there is, as expected[114], a trend of increasing wear rate with increasing load. A plot of the wear rate vs load on a log-log plot (figure 5.7), shows the slope to be $\sim$1.4. While the data are not good enough to permit a one-to-one correspondence with any particular model, it does seem that the plastic deformation lump removal model[114] which predicts $W \propto P$ is most applicable. All other models give a power law of the type $W \propto P^n$ where $n < 0.8$[114]. The absolute wear rate for both the 52100 steel and the coated steel is not entirely unexpected. Archard[114] reports a wear rate for stellite of 7×10^{-8} mm^3/mm for a 1 kg load. Assuming that the mechanism of wear is the same and since the hardness of the steel as compared to that of stellite ($\sim$1000 kg/mm^2) is higher by a factor of two, the wear rate for steel at the same load would be half that for stellite. The experimental result we obtain is of the expected magnitude.

Archard[114] and others[115] have derived an expression for a probability factor, K_{pin}, which indicates the degree to which the transfer of wear is reduced below the maximum expected value. This factor arises because not every contact results in a wear particle; and

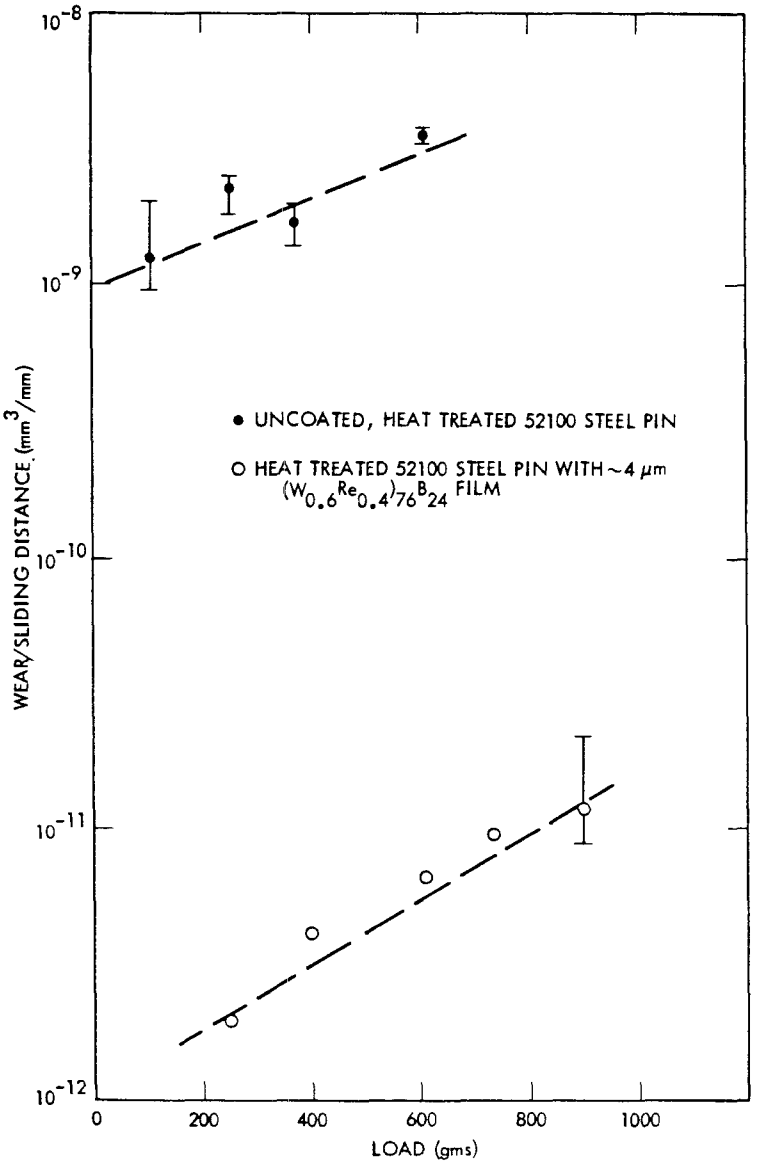

Figure 5.6 Wear rate as a function of load for the $(W_{0.6}Re_{0.4})_{76}B_{24}$ coated and uncoated steels.

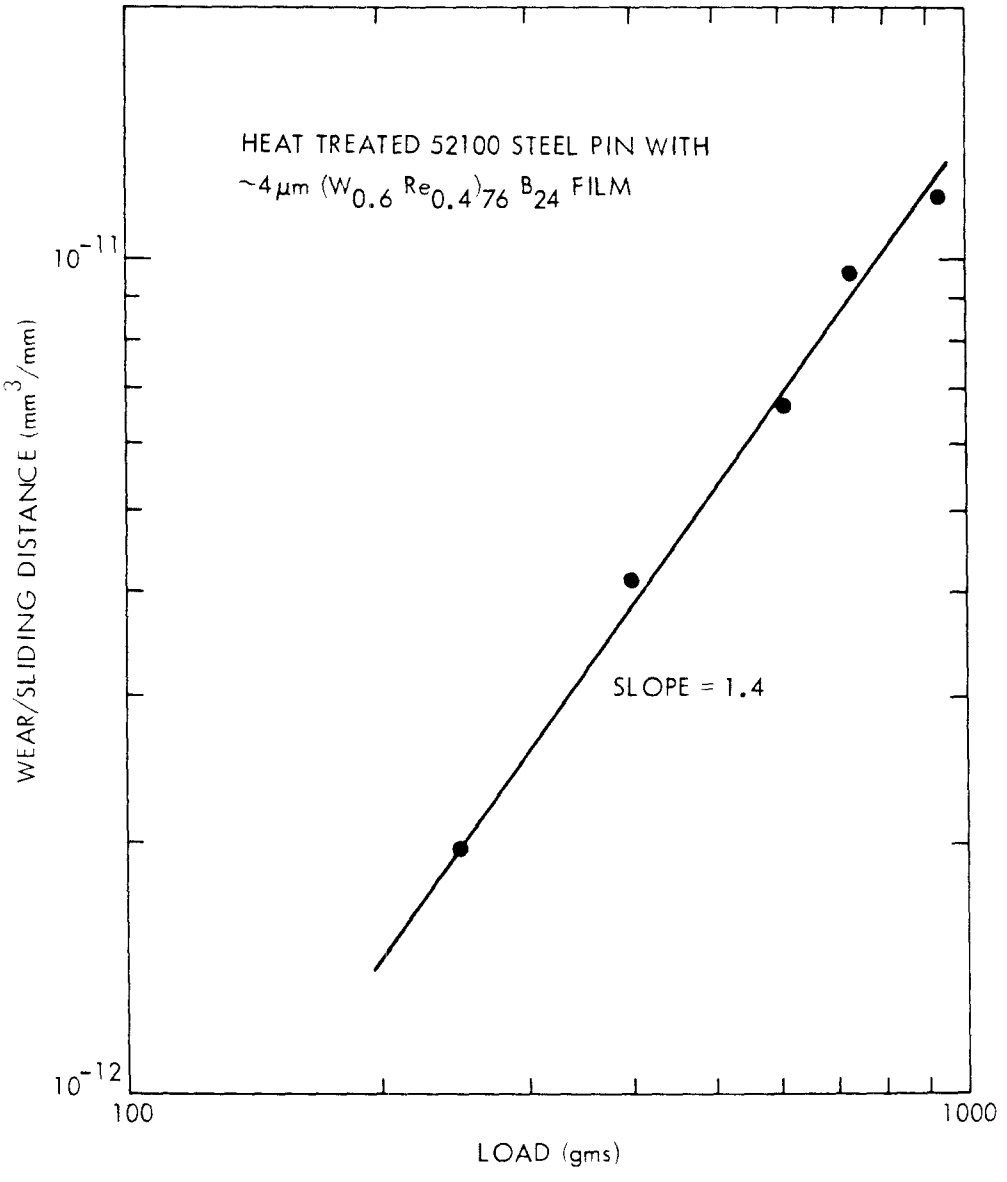

Figure 5.7 A log-log plot of the wear rate versus load for the $(W_{0.6}Re_{0.4})_{76}B_{24}$ coated steel, plotted to obtain the exponent of the power law.

the expression for K_{pin} is

$$K_{pin} = \frac{3\ H\ W}{P}$$

where $H[kg/mm^2]$ is the hardness of the pin , $W[mm^3/mm]$ is the wear rate and P[kg] is the load.

For a plastic wear process, acting through lump removal, the theory predicts that $W \propto P$. This would mean that K_{pin} is independent of load. Figure 5.8 shows the plots of K_{pin} versus load for the uncoated and coated pins. For the coated pin we do find that the dependence of K_{pin} on load diminishes at high loads. For the uncoated steel K_{pin} decreases with load. This is consistent with the suggestion that wear in the steel is restricted, not by plastic flow but by elastic lump removal. The other possibility, namely, layer removal, is unlikely in 52100 bearing steel. In figure 5.8 also plotted for purposes of comparison are the K_{pin} for WC on WC and ferrite steel on tool-hardened steel[116].

We must now focus our attention on the extremely low wear resistance of the coated steel pins. The higher hardness of the film (a factor of 2 over the uncoated pin) cannot alone explain the difference. There must be a significant difference in the wear mechanism itself. It is understood that in crystalline materials the wear debris is formed by preferential crack propogation along slip planes, stacking faults and dislocation pile ups[117]. The presence of such defects and anisotropy in the material leads to surface areas and regions with lower free energy where it is possible to fracture the material. On the other hand, absence of such "preferential sites" for

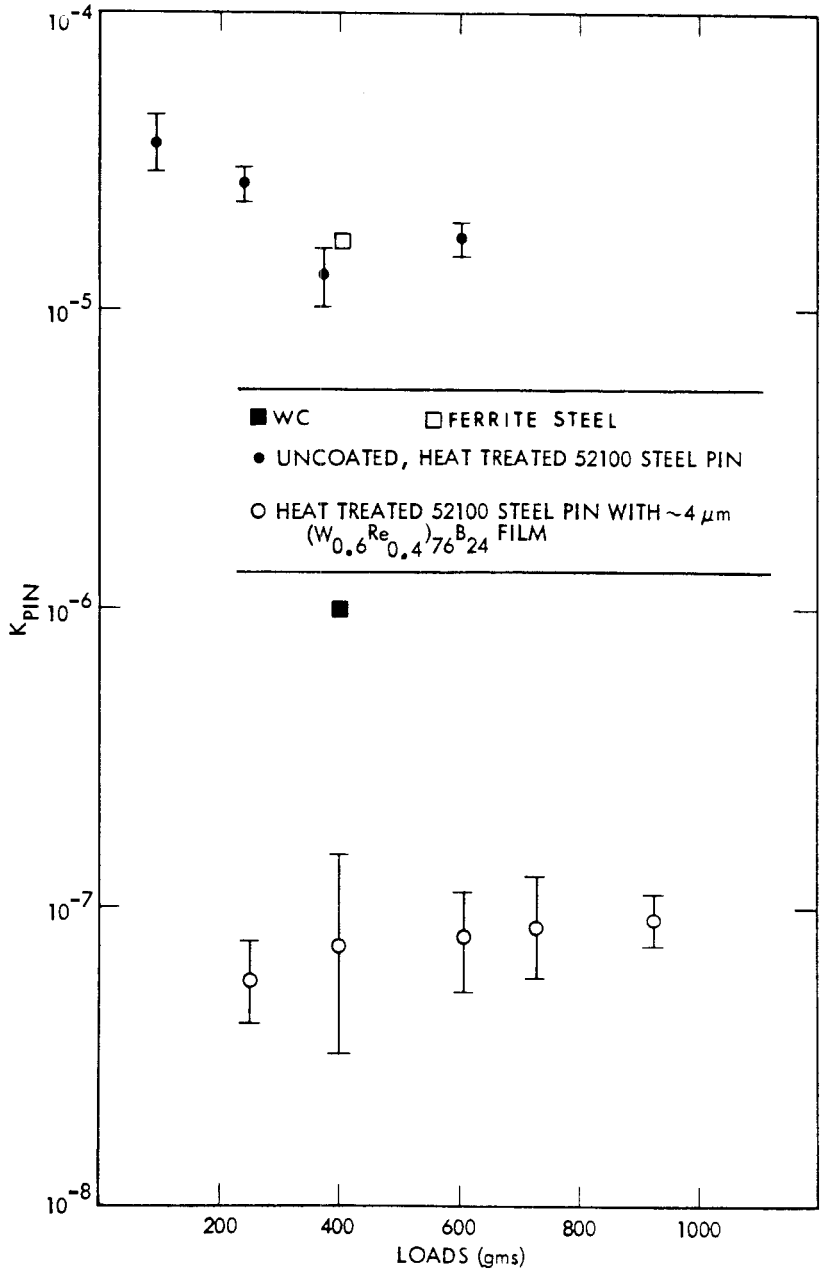

Figure 5.8 The wear parameter, K_{pin}, as a function of load for the $(W_{0.6}Re_{0.4})_{76}B_{24}$ coated and uncoated steels surfaces. Also shown are the results for WC on WC and ferrite steel on tool-hardened steel[116].

crack propogation in amorphous coatings contributes significantly to their high wear resistance. Also, the enhanced smoothness of the surface further reduces the probability that a given contact would result in the formation of a wear particle.

§ 5.1.4 Conclusions

The study indicates that the uses envisaged for amorphous material coatings are indeed realistic. A dramatic improvement of the wear resistance of 52100 steel was obtained upon coating the surface by a thin layer of amorphous $(W_{0.6}Re_{0.4})_{76}B_{24}$. However, it was found that the conditions for film deposition had to be carefully controlled in order to produce well-adherent films.

REFERENCES

1). J. Kramer, Ann. Phys., 19, 37(1934).

2). J. Kramer, Z. Phys., 106, 675(1937).

3). A. Brenner, D.E. Couch and E.K. Williams, J. Res. Natl. Bur. Stand., 44, 1109(1950).

4). W. Buckel and R. Hilch, Z. Phys., 132, 420(1952).

5). W. Buckel and R. Hilch, Z. Phys., 138, 109(1954).

6). W. Klement Jr., R.H. Willens and P. Duwez, Nature, 187, 869(1960).

7). M.H. Cohen and D. Turnbull, Nature, 189, 131(1961).

8). P. Duwez, R.H. Willens and R.C. Crewdson, J. Appl. Phys., 36, 2267(1965).

9). H.S. Chen and D. Turnbull, J. Chem. Phys., 48, 2560(1968).

10). H.S. Chen and D. Turnbull, Acta Metall., 17, 1021(1969).

11). J.J. Gilman, Phil. Mag. B, 37, 577(1978).

12). D. Turnbull, Contemp. Phys., 10, 473(1969).

13). R. Hasegawa, Glassy Metals: Magnetic, Chemical and Structural Properties, ed. R. Hasegawa, Ch.5, CRC Press, Boca Raton, 1983.

14). M. Mehra, A.P. Thakoor, S.K. Khanna and W.L. Johnson, to be published.

15). W.L. Johnson and A.R. Williams, Phys. Rev. B, 20, 1640(1979).

16). The development follows that of D.S. Boudreaux, in Glassy Metals: Magnetic, Chemical and Structural Properties, ed. R. Hasegawa, Ch.1, CRC Press, Boca Raton, 1983.

17). P. Duwez and R.H. Willens, TMS-AIME, 227, 362(1963).

18). P. Pietrokowsky, Rev. Sci. Instrum., 34, 445(1963).

19). R. Pond Jr. and R. Maddin, TMS-AIME, 245, 2475(1969).

20). P.K. Leung and J.G. Wright, Phil. Mag., 30, 995(1974).

21). C.-J. Lin, F. Spaepen and D. Turnbull, J. Non-Cryst. Sol., 61-62, 767(1984).

22). B.-X. Liu, W.L. Johnson, M.-A. Nicolet and S.S. Lau, Appl. Phys. Lett., 42, 45(1983).

23). R.B. Schwarz and W.L. Johnson, Phys. Rev. Lett., 51, 415(1983).

24). B.E. Warren, X-Ray Diffraction, Addison-Wesley, Reading, 1969.

25). G.S. Cargill III, Sol. Stat. Phys., 30, 227(1975).

26). B.E. Warren, H. Krutter and O. Morningstar, J. Amer. Ceram. Soc., 19, 202(1936).

27). Y. Waseda, H. Okazaki and T. Masumoto, Proc. Int. Conf. Non Crys. Sol., p 202, Taylor and Francis, London, 1977.

28). J.F. Sadoc and J. Bletry, Mater. Sci. Engg., 23, 187(1976).

29). A. Lee, G. Etherington and C.N.J. Wagner, J. Non-Cryst. Sol., 61-62, 349(1984).

30). H.-U. Krebs, Ph.D. Thesis, Univ. of Goettingen, 1984.

31). N. Cowlam, Wu. Guoan, P.P Gardner and H.A. Davies, J. Non-Cryst. Sol., 61-62, 337(1984).

32). B.E. Warren, Prog. Metal Phys., 8, 147(1959).

33). J. Dixmier, K. Doi and A. Guinier, Physics of Non Crystalline Solids, ed. J.A. Prins, p 67, North Holland, Amsterdam, 1965.

34). B.E. Warren, J. Appl. Phys., 12, 375(1941).

35). G.S. Cargill III, J. Appl. Phys., 41, 12(1970).

36). K. Suzuki, K. Fukunaga and T. Masumoto, Sci. Rep. Res. Inst. Tohuku Univ., A26, 1(1976).

37). D. Turnbull and D. Cohen, J. Chem. Phys., 52, 3038(1970).

38). J.D. Bernal, Nature, 185, 68(1960).

39). J.D. Bernal, Proc. R. Soc., A280, 299(1964).

40). J.D. Bernal, I.A. Cherry, J.L. Finney and K.R. Knight, J. Phys. E, 3, 338(1970).

41). J.L. Finney, Proc. R. Soc., A319, 479(1970).

42). D.E. Polk, Acta Metall. 20, 485(1972).

43). C.H. Bennet, J. Appl. Phys., 43, 2727(1972).

44). L. von-Heimendahl, J. Phys. F, 5, L141(1975).

45). J.F. Sadoc, J. Dixmier and A. Guinier, J. Non-Cryst. Sol., 12, 46(1973).

46). J. Dixmier and P. Duwez, J. Appl. Phys., 44, 1189(1973).

47). L.J. Lewis and R. Harris, J. Non-Cryst. Sol., 61-62, 547(1983).

48). D.S. Boudreaux and J.M. Gregor, J. Appl. Phys., 48, 5057(1977).

49). H.S. Chen and Y. Waseda, Phys. Stat. Sol., 51, 593(1979).

50). R. Harris and L.J. Lewis, Phys. Rev. B, 25, 4997(1982).

51). A.R. Miedema, R. Boom and F.R. DeBoer, J. Less Com. Met., 41, 283(1975).

52). B.E. Warren, B.L. Averbach and B.W. Roberts, J. Appl. Phys., 22, 1493(1951).

53). J.F. Sadoc and C.N.J. Wagner, Glassy Metals II, ed. H. Beck and H.-J. Guntherodt, Ch.3, Springer Verlag, New York, 1983.

54). A.B. Bhatia and D.E. Thornton, Phys. Rev. B, 2, 3004(1970).

55). H. Berman, Am. Minerologist, 24, 434(1939).

56). D.T. Cromer and J.B. Mann, J. Chem. Phys., 47, 1892(1967).

57). D.T. Cromer, J. Chem. Phys., 50, 4857(1969).

58). G. Breit, Phys. Rev., 27, 362(1926).

59). H.P. Klug and L.E. Alexander, X-Ray Diffraction Procedures, Wiley Interscience, New York, 1974.

60). International Tables for X-Ray Crystallography, Vol. III, ed. N.F.M. Henry and K. Lonsdale, Kynoch Press, Birmingham, 1952.

61). N.S Gingrich, Rev. Mod. Phys., 15, 90(1943).

62). P.H. Gaskell, Glassy Metals II, ed. H. Beck and H.-J. Guntherodt, Ch.2, Springer Verlag, New York, 1984.

63). E. Lorch, J. Phys. C, 2, 229(1969).

64). D.T. Cromer and J.T. Waber, Acta Cryst., 18, 104(1965).

65). D.T. Cromer, Acta Cryst., 18, 17(1965).

66). J.H. Konnert and J. Karle, Acta Cryst. A, 29, 702(1973).

67). G.S. Chadha, N. Cowlam, H.A. Davies and I.W. Donald, J. Non-Cryst. Sol., 44, 265(1981).

68). A. Inoue, A. Kitamura amd T. Masumoto, Trans. Jpn. Inst. Met., 20, 404(1979).

69). A. Williams, M. Mehra and W.L. Johnson, J. Phys. F, 12, 1861(1982).

70). M. Mehra, A. Williams and W.L. Johnson, Phys. Rev. B, 28, 624(1983).

71). P.H. Gaskell, J. Non-Cryst. Sol., 32, 207(1979).

72). S. Rundqvist, Ark. Kemi, 20, 67(1963).

73). Y. Andersson, V. Kaewchausilp, M. Soto and S. Rundqvist, Acta Chem. Scand., 28, 297(1974).

74). S. Kobayashi, K. Maeda and S. Takeuchi, Jpn. J. Appl. Phys., 19, 1033(1980).

75). P.J. Cote and L.V. Meisel, Glassy Metals I, ed. H.-J. Guntherodt and H. Beck, Ch.7, Springer Verlag, New York, 1981.

76). See, e.g., A.K. Sinha and P. Duwez, J. Phys. Chem. Solids, 32, 267(1971).

77). C.J. Kempter and R.J. Fries, J. Chem. Phys., 34, 1994(1961).

78). F.S. Galasso, Structure and Properties of Inorganic Solids, Ch.6, Pergamon Press, Oxford, 1970.

79). J.W. Edington, Practical Electron Microscopy in Materials Science, Appendix 4, van Nostrand Reinhold, New York, 1976.

80). B. Post and F.W. Glaser, Trans AIME 194, 631(1952).

81). D.S. Boudreaux and H.J Frost, Phys. Rev. B, 23, 1506(1981).

82). P.H. Gaskell, Acta Metall., 29, 1203(1981).

83). Sargent-Welch Tables, Cat. No. S-18806, Sargent Welch Scientific Co.

84). R. Ray, R. Hasegawa, C.-P. Chow and L.A. Davis, Scr. Metall., 11, 973(1977).

85). J.H Mooij, Phys. Stat. Sol. a, 17, 521(1973).

86). H.O.K. Kirchner, Mater. Sci. Eng., 23, 95(1976).

87). M.G. Scott and R. Maddin, Proc. 2nd Int. Conf. RQM, ed N.J. Grant and B. Geissen, p 249, Section I, MIT Press, Cambridge, 1976.

88). A.M. Flank, M. Harmelin, M. Jaulin and A. Noudon, Rev Phys. Appl., 15, 1427(1980).

89). S.K. Khanna, A.P. Thakoor, R.F. Landel, M. Mehra and W.L. Johnson, Appl. Phys. Comm., 1, 135(1981-82).

90). M. Mehra, W.L. Johnson, A.P. Thakoor and S.K. Khanna, Sol. Stat. Comm., 47, 859(1983).

91). W. Kauzmann, Chem. Revs., 42, 219(1948).

92). F. Spaepen, Phil.Mag., 30, 417(1974).

93). M.R. Hoare and P.Pal, Adv. Phys., 20, 161(1971).

94). M.R. Hoare, J. Non-Cryst. Sol., 31, 157(1978).

95). R. Schulz, Ph.D Thesis, Caltech, Pasadena, 1984.

96). A.R. Williams and W.L. Johnson, J. Non-Cryst. Sol., 34, 121(1979).

97). A. Guinier, X-Ray Diffraction, Ch.3, Freeman, San Fransisco, 1963.

98). W.L. Johnson, Physical Metallurgy, ed. R.W. Cahn and P. Haasen, Ch.27, North-Holland, Amsterdam, 1984.

99). W.L. Johnson, Glassy Metals I, ed. H.-J. Guntherodt and H. Beck, Ch.9, Springer Verlag, New York, 1981.

100). B.M. Clemens, Ph.D. Thesis, Caltech, Pasadena, 1982.

101). C.C. Koch, D.M. Kroeger, J.S. Lin, J.O. Scarborough, W.L. Johnson and A.C. Anderson, Phys. Rev. B, 27, 1586(1983).

102). A.L. Drehman and W.L. Johnson, Phys. Stat. Sol. a, 52, 499(1979).

103). B.M. Clemens, M. Mehra and W.L. Johnson, to be published.

104). A. Davidson and M. Tinkham, Phys. Rev. B, 13, 3261(1976).

105). K. Maki, Physics, 1, 127(1964).

106). M. Tenhover, W.L. Johnson and C.C. Tsuei, Sol. Stat. Comm., 38, 53(1981).

107). S. Foner, Superconductivity in d- and f-Band Metals, ed. D.H. Douglass, p 161, Plenum Press, New York, 1976.

108). T.P. Orlando, E.J. McNiff Jr., S. Foner and M.R.. Beasley, Phys. Rev. B, 19, 4545(1979).

109). S.T. Hopkins and W.L. Johnson, Sol. Stat. Comm., 43, 537(1982).

110). P. Lamparter, W. Sperl, S. Steeb and J. Blétry, Z. Naturforsch., 37a, 1223(1982).

111). J.-B. Suck and H. Rudin, Glassy Metals II, ed. H. Beck and H.-J. Guntherodt, Ch.7, Springer Verlag, New York, 1983.

112). S. Analage, Caltech, Pasadena. Private Communication.

113). J.A. Thornton, Deposition Technologies for Films and Coatings, ed. R.F. Bunshah, p222, Noyes, Parkridge, 1982.

114). J.F. Archard, J. Appl. Phys., 24, 981(1953).

115). F.P. Bowden and D. Tabor, The Friction and Lubrication of Solids, Oxford Univ. Press, Oxford, Part I : 1950, Part II : 1964.

116). J.F. Archard, J. Appl. Phys., 32, 1420(1961).

117). A.D. Sarkar, Wear of Metals, p 93, Pergamon Press, Oxford, 1976.